Energy, Material, and Telecommunication center

ENGINEERING HEAVY-METAL-FREE TERNARY COLLOIDAL QUANTUM DOTS FOR SECURITY AND ENERGY APPLICATIONS

By

Kokilavani Shanmugasundaram

Thesis presented for obtaining the degree of

Master of Science (M.Sc.)

Master in Energy and Material Sciences

Jury members

President of the jury and Internal Examiner	Prof. Kulbir Kaur Ghuman INRS-EMT
External Examiner	Prof. Rafik Naccache Concordia University
Research Director	Prof. Fiorenzo Vetrone INRS-EMT
Research Co-directors	Prof. Federico Rosei INRS-EMT
	Prof. Gurpreet S. Selopal Dalhousie University

ACKNOWLEDGEMENTS

First and foremost, I would like to sincerely express my heartfelt gratitude to God for his blessings throughout my Master's journey. I am profoundly thankful to my supervisor, Prof. Fiorenzo Vetrone, for his invaluable guidance, patience, and support. My sincere thanks to my co-supervisor, Prof. Federico Rosei, for providing me with the best research environment and resources and offering me a lifetime opportunity to grow as a young researcher and work in such a dynamic group.

I sincerely thank my co-supervisor, Prof. Gurpreet Singh Selopal, for his unwavering guidance and support. His constructive feedback and stimulating discussions to improve the quality of my research, along with his encouragement and motivation, have inspired my Master's work.

I am grateful to Dr. Lei Jin for mentoring skills, enthusiasm, and insightful advice for my thesis work. I would like to extend my appreciation to my team members from the Nano-Femto Group and all collaborators for their support to finish my master research work. Special thanks to Christophe Chabiner and Dr. Catalin Harnagea for their assistance with SEM and XRD analysis, Chamoulaud Gwénaël for help with the UV-Vis absorption spectrophotometer and fluorometer, and Daniel Chartrand for his guidance in performing PL lifetime measurements.

I am deeply appreciative to my colleagues at INRS-EMT who encouraged and helped me during challenging times. I thank my family for their constant support, love, and belief in me which have been my strength to finish my Master work.

Finally, I would like to acknowledge the MITACS and CREATE-SEED (Collaborative Research and Training Experience in Sustainable Electronics and Eco-Design) program for the financial support.

ABSTRACT

Colloidal Quantum dots (QDs) are semiconductor nanocrystal whose size-/shape-/composition-dependant optoelectronic properties make it a promising candidate for security and energy conversion applications. Nevertheless, most high-performing QDs contain heavy metals (Pb, Cd) that raise toxicity concerns and hamper their commercial-scale application. In this context, Cu-based ternary QDs have been recognised as potential alternative due to its low-toxicity, wide-spectral tunability, and broad absorption and emission characteristics. On the other hand, their complex stoichiometry induces high density of surface traps/defects, resulting in limited long-term operation stability and poor performance during device operation. This thesis work focuses on the optimization of the heavy-metal-free ternary QDs as discussed below.

First, a colloidal ternary heavy-metal-free ZnSeS shell engineered Cu:$ZnInSe_2$ ($CZISe_2$/ZSeS) QDs was developed as light harvesters for photoelectrochemical (PEC) hydrogen (H_2) production. To attain uniform shell growth, in-situ growth passivation approach was employed via one-pot hot-injection method. The interface defects between core/shell and charge carrier dynamics were regulated by modulating Se:S ratio to obtain an alloyed ZnSeS shell. Resulting $CZISe_2$/ZSeS QDs offer a higher PL lifetime (154 ns) and better charge transfer rate than $CZISe_2$ QDs, indicating the alloyed shell favours the charge separation/transfer process. The employed $CZISe_2$/ZSeS QDs exhibit a saturated photocurrent density of 11.80 mA/cm^2, which is ≈7.8% much higher than $CZISe_2$ QDs under 1 sun illumination (AM 1.5G, 100 mW/cm^2), respectively. The operational stability and PEC performance was further improved through integration of MWCNTs. The T:M-$CZISe_2$/ZSeS QDs-based PEC device delivers a record of high photocurrent density (13.15 mA/cm^2) and excellent operational stability (~80% for 3600s). This work highlights the crucial role of optimizing the core/shell QDs with appropriate shell material to advance the use of heavy-metal free QDs for PEC-H_2 production and other solar energy conversion technologies (i.e., solar cells)

Second, a synergistic approach was employed to modulate the optical characteristics of heavy-metal-free $ZnInSe_2$/ZnSe core/shell QDs by incorporating Cu-doping and Mn-alloying into their core and shell to investigate their use in anti-counterfeiting and information encryption. The engineered “Cu:$ZnInSe_2$/Mn:ZnSe” core/shell QDs exhibit an intense bright orange photoluminescence (PL) emission centered at 606 nm, with better color purity than the undoped and individually doped core/shell QDs. The average PL lifetime is significantly prolonged to 201 ns, making it relevant for complex encryption and anti-counterfeiting. PL studies reveal that in

Cu:$ZnInSe_2$/Mn:ZnSe, the photophysical emission arises from the Cu state via radiative transition from the Mn $^4T_1$ state. Integration of Cu:$ZnInSe_2$/Mn:ZnSe core/shell QDs into poly(methyl methacrylate) (PMMA) serve as a versatile smart concealed luminescent inks for both writing and printing patterns. The features of these printed patterns using Cu:$ZnInSe_2$/Mn:ZnSe core/shell QDs persisted after 10 weeks of water-soaking, and retained 70% of their PL emission intensity at 170 °C, demonstrating excellent thermal stability.

In summary, this thesis work provides different strategy to engineer the heavy-metal-free ternary QDs for improved performance of PEC device and optical anti-counterfeiting device. The choice of shell material significantly influences the performance and stability of these QDs, making it a key factor in optimizing solar energy harvesting and conversion efficiency. Furthermore, it provides an efficient approach to enhance both the emission and stability of heavy-metal-free QDs via dopant engineering for fluorescence anti-counterfeiting application.

Keywords: Quantum dots; Core/shell; Heavy-metal-free; Transition metal dopants; Photoluminscence; Carrier dynamics; Stability; Photoelectrochemical cells; Water splitting; Anti-counterfeiting.

RÉSUMÉ

Les points quantiques colloïdaux (QDs) sont des nanocristaux semi-conducteurs dont les propriétés optoélectroniques dépendent de la taille, de la forme et de la composition, ce qui en fait des candidats prometteurs pour des applications de sécurité et de conversion énergétique. Néanmoins, la plupart des QDs à haute performance contiennent des métaux lourds (Pb, Cd), soulevant des préoccupations de toxicité et freinant leur adoption à l'échelle commerciale. Dans ce contexte, les QDs ternaires à base de Cu ont été reconnus comme une alternative potentielle en raison de leur faible toxicité, de leur large accordabilité spectrale et de leurs caractéristiques d'absorption et d'émission étendues. Cependant, leur stœchiométrie complexe induit une forte densité d'états de défaut de surface, entraînant une stabilité de fonctionnement limitée à long terme et des performances médiocres pendant les périodes d'utilisation des dispositifs. Cette thèse se concentre sur l'optimisation des QDs ternaires exempts de métaux lourds, décrits ci-dessous.

Tout d'abord, une coquille ternaire colloïdale sans métaux lourds de ZnSeS a été développée pour des QDs Cu:$ZnInSe_2$ ($CZISe_2$/ZSeS), destinés à la photoélectrochimie. Pour obtenir une croissance uniforme de la coquille, une approche de passivation in situ a été employée via une méthode d'injection à chaud en une seule fois. Les défauts d'interface entre le noyau et la coquille ainsi que la dynamique des porteurs de charge ont été régulés en modulant le rapport Se:S afin d'obtenir une coquille alliée de ZnSeS. Les $CZISe_2$/ZSeS QDs obtenus présentent une durée de vie de photoluminescence (PL) prolongée (154 ns) et un meilleur taux de transfert de charge que les QDs $CZISe_2$, ce qui indique que la coquille alliée favorise le processus de séparation/transfert de charge. Les QDs $CZISe_2$/ZSeS présentent une densité de photocourant saturé de 11,80 mA/cm² sous une illumination solaire (AM 1,5G, 100 mW/cm²), soit 7,8 % de plus que les $CZISe_2$ QDs. La stabilité opérationnelle et les performances en photoélectrochimie (PEC) ont été encore améliorées par l'intégration de MWCNT. Le dispositif PEC à base de T:M-$CZISe_2$/ZSeS QDs a permis d'atteindre un nouveau record de densité de photocourant élevé (13,15 mA/cm²) et une excellente stabilité opérationnelle (~80 % pendant 3600 s). Ce travail met en évidence l'importance cruciale de l'optimisation des QDs cœur/coquille avec un matériau de coquille approprié pour faire progresser l'utilisation de QDs sans métaux lourds pour la production de H_2 en PEC et d'autres technologies de conversion d'énergie solaire, telles que les cellules solaires.

Deuxièmement, une approche synergique a été employée pour moduler les caractéristiques optiques des $ZnInSe_2$/ZnSe QDs sans métaux lourds, en incorporant un dopage au Cu et un alliage au Mn dans leur noyau et leur coquille afin d'étudier leur utilisation dans la lutte contre la contrefaçon et le cryptage de l'information. L'ingénierie des QDs cœur/coquille Cu:$ZnInSe_2$/Mn:ZnSe a produit une photoluminescence (PL) orange vif intense centrée à 606 nm, avec une meilleure pureté de couleur que les QDs non dopés ou dopés individuellement. La durée de vie moyenne de la PL a été considérablement prolongée à 201 ns, ce qui les rend pertinents pour des applications complexes de cryptage et de lutte contre la contrefaçon. Les études de PL révèlent que dans les Cu:$ZnInSe_2$/Mn:ZnSe QDs, l'émission photophysique provient de l'état Cu via une transition radiative à partir de l'état Mn $^4T_1$. L'intégration de QDs Cu:$ZnInSe_2$/Mn:ZnSe dans le poly(méthacrylate de méthyle) (PMMA) sert d'encres luminescentes polyvalentes et intelligentes pour l'écriture et l'impression de motifs. Les caractéristiques de ces motifs imprimés avec des Cu:$ZnInSe_2$/Mn:ZnSe cœur/coquille QDs ont persisté après 10 semaines d'immersion dans l'eau et ont conservé 70% de leur intensité d'émission PL à 170 °C, démontrant une excellente stabilité thermique.

En résumé, cette thèse propose une stratégie innovante pour la conception de QDs ternaires exempts de métaux lourds, afin d'améliorer les performances des dispositifs PEC et des dispositifs optiques anti-contrefaçon. Le choix du matériau de coquille joue un rôle clé dans l'optimisation des performances et de la stabilité de ces QDs, en faisant un facteur essentiel pour l'efficacité de la collecte d'énergie solaire et de la conversion. De plus, elle fournit une approche efficace pour améliorer à la fois l'émission et la stabilité des QDs sans métaux lourds via l'ingénierie des dopants pour une application anti-contrefaçon par fluorescence.

Mots-clés : Points quantiques; cœur/coquille; respectueux de l'environnement; dopants de métaux de transition; photoluminescence; dynamique des porteurs de charge, stabilité; cellules photoélectrochimiques; séparation de l'eau; lutte contre la contrefaçon.

TABLE OF CONTENTS

LIST OF FIGURES

LIST OF TABLES

LIST OF EQUATIONS

LIST OF ABBREVIATIONS

CQDs	Colloidal Quantum dots
VB	Valence Band
CB	Conduction Band
DOS	Density of States
$E^{1/2}$	Energy of states
OLA	Oleylamine
TOPO	Trioctylphosphine oxide
HAD	Hexadecylamine
PLQY	Photoluminscence Quantum Yield
$TMGe_3As$	Tris(trimethylgermyl)arsine
DAP	Donor-Acceptor Pair
NCs	Nanocrystals
MEG	Multiple-Exciton Generation
LARP	Ligand Assisted Reprecipitation
Zb	Zinc blende
Wz	Wurzite
Cu	Copper
Mn	Manganese
In	Indium
AC	Alternating Current
PEC	Photoelectrochemical
Eg	Band Gap
STH	Solar-to-hydrogen
MWCNTs	Multi-walled Carbon Nanotubes
MOF	Metal-Organic Framework
GBC	Global Brand Counterfeiting
ACF	Anti-counterfeiting
UC	Up conversion
Dc	Down conversion
RGB	Red-Green-Blue
PMMA	Poly(methyl methacrylate)
$Zn(OAc)_2$	Zinc acetate
$In(OAc)_3$	Indium (III) acetate
Se	Selenium powder
S	Sulfur
$Cu(OAc)_2{\cdot}H_2O$	Copper (II) acetate monohydrate
$Mn(OAc)_2$	Manganese acetate
$Zn(OAc)_2.2H_2O$	Zinc acetate dehydrate
ODE	1-octadecene
DDT	1-dodecanethiol
DCM	Dichloromethane
TEOS	Tetraethyl orthosilicate
$Na_2S.9H_2O$	Sodium sulfide nonahydrate
Na_2SO_3	Sodium sulfite
FTO	Fluorine doped tin oxide
EPD	Electrophoretic deposition
Pt	Platinum
LSV	Linear Sweep Voltammetry
OCP	Open Circuit Voltage
EIS	Electrochemical Impedance Spectroscopy
RHE	Reversible Hydrogen Electrode
XRD	X-ray diffraction
TEM	Transmission Electron Microscopy
SEM	Scanning Electron Microscopy
SE	Secondary electrons
BSE	Backscattered electrons
TRPL	Time-resolved PL spectroscopy
TCPSC	Time-correlated single-photon counting
XPS	X-ray Photoelectron Spectroscopy
B.E	Binding Energy
Q	Charge
J	Photocurrent density
V	Voltage
T	Temperature
K_B	Boltzman constant
R_{ct}	Charge transfer resistance
PL	Photoluminescence
CIE	Commission Internationale de l'Eclairage
R	Radius
ε_0	Permittivity in free space
ε_r	Relative permittivity
m_e*	Effective mass of excited electron
m_h*	Effective mass of hole
QY	Quantum Yield
UPS	Ultra-violet Photoelectron Spectroscopy
PCE	Photoconversion Efficiency
eV	Electron Volts
mL	Milli Liters

KHz	KiloHertz
mHz	MegaHertz
θ	Incident Angle
λ	Wavelength
Wt%	Weight Percentage
T	Average Lifetime
TAS	Transient Absorption spectroscopy

INTRODUCTION

1.1 Background

Semiconductor nanocrystals so-called colloidal quantum dots (CQDs) are nanoscale tiny sized particles (typically in size range from ~2-20 nm) which are analogous to bulk semiconductors and differ based on quantum confinement effect (Figure 1.1a-b) [1]. CQDs tightly confine their charge carrier like a three-dimensional (3D) particle in a box model. CQDs exhibit size/shape/composition tunable absorption and emission features that are related with the transitions between the discrete quantum mechanically allowed energy levels as like atoms or molecules [2]. These features make it referred to as artificial atoms [3].

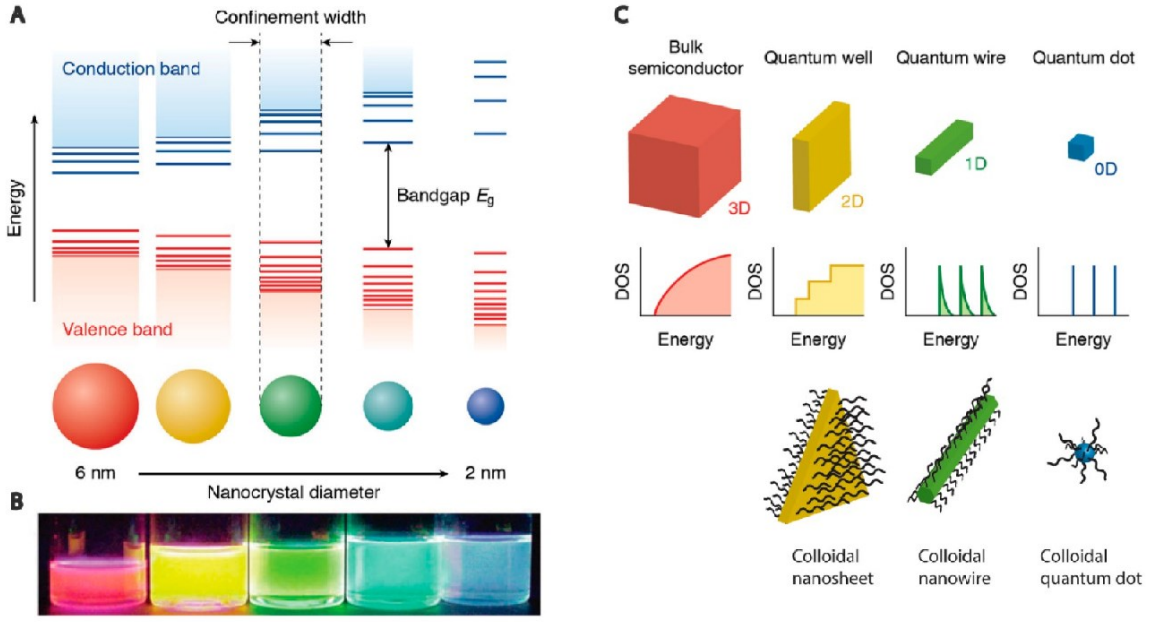

Figure 1.1 (a) Quantum confinement effects in QDs. (b) CdSe CQDs of different sizes under UV light irradiation. (c) Schematic representation of the semiconductor in different dimension and their corresponding density of states. Organic ligands capped different colloidal NCs from 2D to 0D (bottom panel) [4].

According to quantum mechanical calculations, these discrete energy levels are not observed in bulk materials. Generally, the valence band (VB) and conduction band (CB) of a material is described through “density of states” (DOS). DOS represents the number of allowed modes or states per unit energy. As depicted in Figure 1.1c, the change in the dimensions have significant impact on the DOS. In a bulk 3D semiconductor, the DOS is dependent on the square root of

energy ($E^{1/2}$) whereas in case of 2D the DOS increases in quantified steps (~E^0). For 1D nanotubes or nanowires, the excitons travel along the wire/tube, resulting in a DOS with inverse square root energy dependence (~$E^{-1/2}$). QDs with 0D exhibit DOS with discrete allowed energy states. Thus, the band gaps present in QDs (known as Bohr radius) can be varied by changing the size, shape, and charge potential [4]. The light emission from the recombination of electron and hole is dependent on the particle size. Larger size QDs emit longer wavelengths, whereas small size QDs emit short wavelengths. Based on the 3D particle in a box model, the band gap of a QDs is determined according to the Brus equation given below (Equation 1):

Equation 1 Brus equation based on 3D particle in a box model

$$\Delta E = E_g\,(bulk) + \frac{h^2}{8R^2}\left(\frac{1}{m_e^*} + \frac{1}{m_h^*}\right) - \frac{1.786e^2}{4\pi\varepsilon_0\varepsilon_R R^2} \quad (1)$$

Where ΔE refers to band gap of QDs; E_g is band gap of bulk semiconductor; R is the radius; ε_0 is the permittivity in free space; ε_r is the relative permittivity; m_e* is the effective mass of excited electron and m_h* is the effective mass of hole [5]. The equation explains that the size of QDs is inversely proportional to band gap. Thus, the emission wavelength changes with QDs size that is responsible for multi-color nature of QDs. The tunable energy band gaps based on size, shape and composition make them a potential candidate for various optoelectronic applications, including LEDs, Lasers, single-electron transistors, solar cells, quantum computing, cell biology research, microscopy, and second-harmonic generation (Figure 1.2) [6].

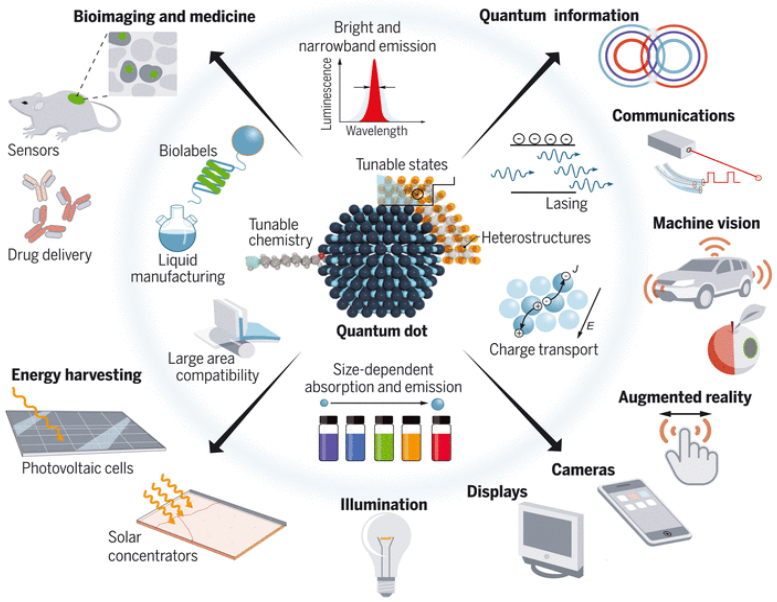

Figure 1.2 CQDs have unique features for different applications, from quantum information to bioimaging and medicine [6].

During 1987, the efforts on the controlled synthesis of CQDs using II-VI semiconductors had often resulted in polydispersity in size and shape, poor crystallinity, and surface electronic defects, which explained the need to study an appropriate high-quality model system with distinguishing properties relative to nanometer-sized regions [7, 8]. Murray, Norris and Bawendi present a simple route to synthesize high-quality monodispersed CdE (E=Se, S and Te) [9]. Different sizes from 1.2 to 11.5 nm (diameter by its major axis) were produced with consistent crystallinity, a high degree of monodispersity and surface derivatization in a single reaction. The 2023 Nobel Prize in Chemistry was awarded for the “Discovery and synthesis of colloidally stable Quantum dots” as a ground-breaking invention in the field of nanotechnology [10]. To understand how these high-quality nanocrystals are obtained, we will look at some of the works inspired by Murray and co-workers. At the beginning of 1857, the studies and investigation on monodisperse lyophobic colloids (ex. Au sols) revealed that the formation happens through temporally discrete nucleation events followed by controlled growth [11, 12]. Inspired by this, Murray et al. [9] have attained the nucleation through the injection of reagents at high temperatures. The nucleation process is controlled by several factors, including temperature, interfacial tension, and degree of supersaturation [13]. This nucleation step is terminated through the rapid drop in temperature via fast injection into the hot coordinating solvent that induces the nanocrystal growth [14]. The growth of nanocrystals is a competing reaction between the two effects: (i) diffusion-controlled growth (focusing effect) and (ii) reaction-controlled growth (defocusing effect) [15]. In diffusion-controlled growth, the smaller particles

grow faster (growth rate proportional to radius) than larger particles to obtain a narrow size distribution only if the secondary nucleation process is avoided [16]. In contrast, the reaction-controlled growth is based on the dissolution and chemical potential of particles. Smaller particles dissolve faster due to higher surface energy and move towards sites on large particles, which is popularly known as Ostwald ripening [17].

Both reaction-controlled and diffusion-controlled growth are governed by a critical radius to form a stable particle highly dependent on the supersaturation limit [16]. For instance, in a typical synthesis, a near-symmetrical distribution (focusing effect) with a constant number of particles is first observed. When the defocusing effects prevail, the particle size exceeds the critical radius, producing a broader-size particle with an asymmetrical distribution (Figure 1.3).

CQDs have a high surface area-to-volume ratio, which is compensated using surfactants or ligands during the synthesis. Most of the synthetic routes to prepare CQDs employ surfactant molecules (polar head and long hydrocarbon tail) such as oleic acid, dodecane-thiol, oleyl amine, trioctyl phosphine or trioctyl phosphine oxide [18]. These surfactants tune the reactivity of precursors that influence the nucleation rate and growth process. The choice of surfactants is determined based on the coordination chemistry with the surface atoms of CQDs. The interaction between the organic molecules and inorganic nanocrystals allows the manipulation independently to tailor the properties as desired, and this can give rise to novel properties.

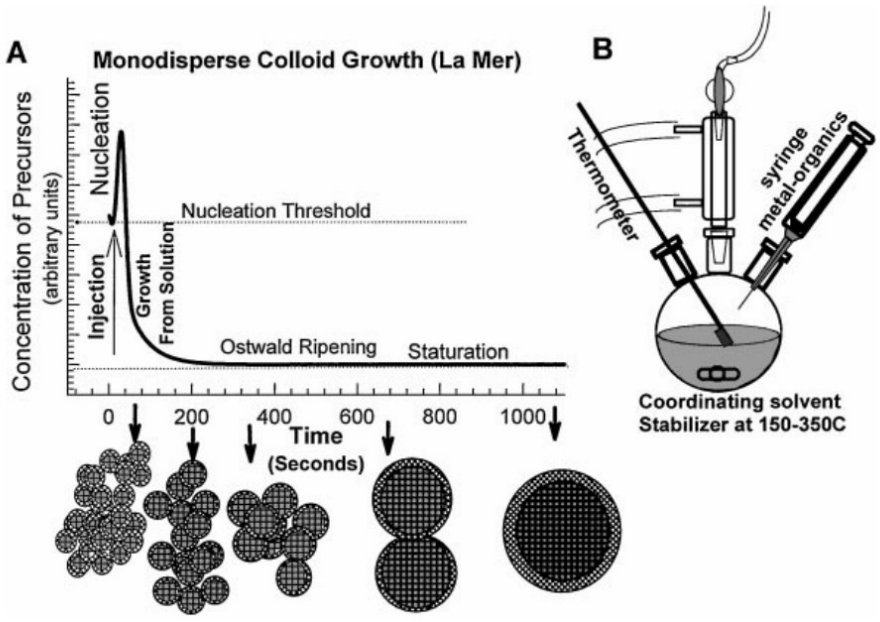

Figure 1.3 (a) Pictorial representation of various stages involved in the synthesis of NCs according to La Mer model. During the NC growth phase, aliquots were removed in regular interval of time to isolate the NC based on size. (b) Diagram to illustrate the synthesis vessel used for synthesizing NCs [19].

1.2 Synthetic methods

During the last three decades, a size-and-shape-controlled synthesis of CQDs has been achieved through hot injection or heat-up methods. These methods produce high-quality nanocrystals and are cost-effective and scalable. The hot-injection methods involve the rapid injection of precursors into hot-coordinating solvents. The injection temperature is critical as it varies based on the decomposition of precursors. After supersaturation, the growth begins with the termination of nucleation. On a large scale, hot-injection synthesis poses significant challenges, such as controlling reaction temperature during precursor injection and low reproducibility because of batch-to-batch synthesis. By comparison, in the heat-up method, the nucleation and growth steps are achieved through steady heating of a precursor and ligand mixtures [20].

Continuous flow synthesis presents numerous advantages over batch methods, including simplicity, scalability, effective mixing of reagents/solvents, reaction parameter controls, and sequential analysis. In addition, it allows full automatic control over the synthesis [21]. Recently, the dual temperature stage flow reactor had a significant impact on separating the nucleation and growth process that resulted in improved control over obtaining a narrow size distribution of CQDs. A high-quality CdS nanocrystals were produced by thermodynamic and kinetic control of the nucleation and growth process. Cao et al. [22] produced high-quality CdS nanocrystals by automatic separation of nucleation and growth process through control of thermodynamics and kinetics of nanocrystals in the nucleation stage. Successive ionic layer adsorption and reaction (SILAR) have been examined for the in-situ CQDs synthesis methods [23]. A good control over size and stoichiometry with improved coverage of surface ligands was obtained using SILAR synthesis [24]. However, SILAR-based CQDs suffer from severe corrosion compared to ex-situ synthesized CQD devices [25].

In CQDs synthesis, the interplay between the organic surfactant molecules and the organic-inorganic interface is crucial during the synthesis, which is the driving force for the control of different sizes, shapes, and architectures achieved in recent years [26, 27]. The typical process to synthesize CQDs via hot-injection technique as follows: The mixture containing organometallic precursor and molecular surfactants in a solvent is heated to a temperature (T_1) in the range from 100 - 320 °C under an inert gas flow (N_2 or Ar) [28]. The inert gas flow prevents the oxidation of precursors [21]. The non-metallic precursors (T_2, room temperature) are rapidly injected into the hot mixture that quickly reduces the temperature, and slow growth begins to produce the CQDs [29]. Different parameters such as precursor concentration, type of surfactants and precursors, reaction temperature, molar ratios of precursors, reaction time, etc.,

can be varied to control the size, shape, and structure of CQDs. As an example, to synthesize PbS QDs, $PbCl_2$ (0.56 g) is mixed with oleyl amine (OLA; 10 mL) and heated to 75 - 150 °C (based on desired particle size). After 30 min, 3 mL from sulphur stock solution (0.16 g, 15 mL) is mixed with OLA (3 mL) and quickly injected into the reaction mixture and growth time is maintained for 20 min to produce PbS QDs. The size of PbS QDs was tuned in the range of 3 - 9 nm by changing the reaction temperature [30]. The synthesis approach can be applied to different kinds of QDs that emit light in the range from UV to Visible and NIR (400 - 2000 nm) [28]. The TEM images of a few CQDs are depicted in Figure 1.4a. The size dependant change in emission of CdSe/ZnSe core/shell CQDs shows the variation in emission color based on size (emit blue color ~1.7 nm and red color ~5 nm) (Figure 1.4b). The shape of nanocrystals can also be tailored through selective adhesion of surfactant molecules to form CQDs from nearly spherical to highly anisotropic. The strong binding nature of capping molecules inhibits the growth of selective facets that lead to the production of a variety of shapes. Different shapes of NCs, including rod-, rise-, tear-, drop-, arrow-, and tetra pods, can be obtained by changing the concentration of alkyl phosphonic acid, heating regime and length of the alkyl chain (Figure 1.4c).

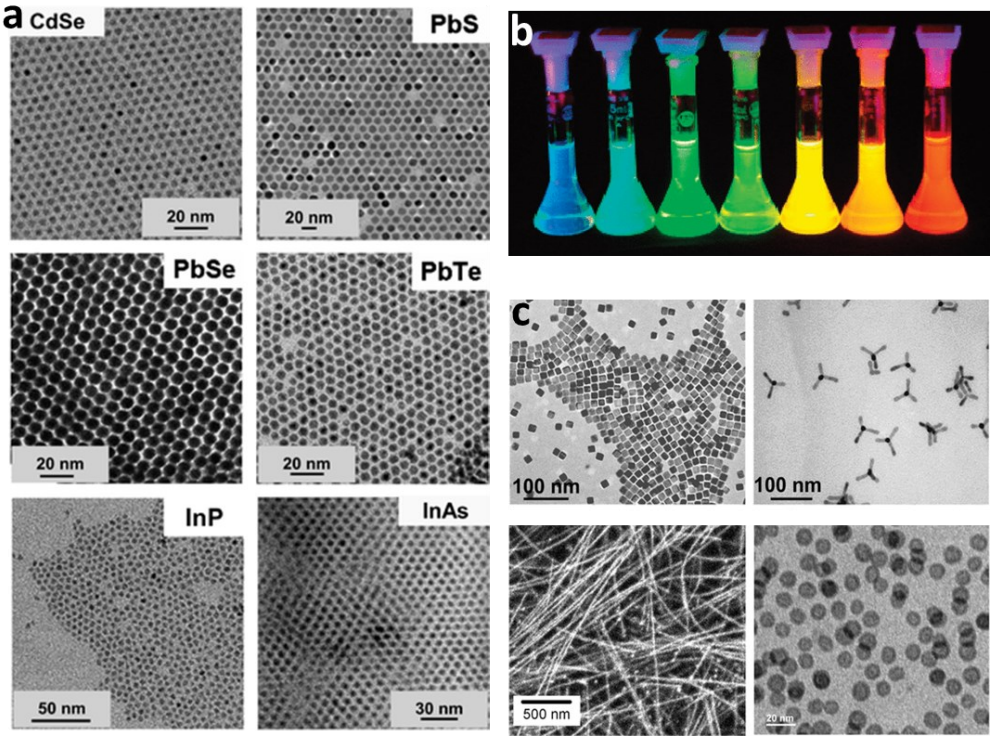

Figure 1.4 (a) TEM image of different colloidal nanocrystals, (b) Color emission from Colloidal solutions of CdSe/ZnSe core/shell NCs [31], and (c) PbSe cubes [32], CdTe tetrapods [33], PbSe nanowires [32], and hollow iron oxide NPs.

CQDs are engineered to have intriguing optical and electrical properties by tuning composition, structural modification, and impurity doping strategy. Recent progress in research and development of CQDs has led to a diverse array of structures and unique functionalities for specific applications, ranging from biological imaging to optoelectronic applications.

1.3 Composition-engineered QDs

1.3.1 II-VI semiconductors

The II-VI QDs are composed of elements from groups II and VI from the periodic table, such as the CdS, CdSe, PbS, PbTe, ZnS, ZnSe, CdTe and so on. Earlier, high-quality Cd-based QDs were fabricated using an expensive $Cd(CH_3)_2$ with Trioctylphosphine oxide (TOPO) as a surface capping agent [34]. Studies then explored different low-cost Cd precursors (CdO, $Cd(AC)_2$ and $Cd(CO_3)_2$) precursors to prepare high-quality CdSe QDs as an alternative to $Cd(CH_3)_2$ [35, 36]. Meanwhile, Hexadecylamine (HDA) has been used as a single monomer surfactant to regulate the shape of CdS nanocrystals into monorod, bipod, tripod, and tetrapod and pencil-type rod by simple variation in growth temperature or precursor concentration [37]. The zinc blende (Zb) CdSe crystal structure shows high photoluminescence quantum yield (PLQY) (37%) than Wurtzite (Wz) CdSe QDs due to the Cd^{2+} rich surface that prevents the excess surface traps/defects by forming a CdO layer [38]. In line with this, studies were focused on controlling stoichiometry to achieve highly monodispersed QDs. For instance, the control of the stoichiometric ratio of precursor in PbS (Pb/S – 24:1) has proven to delay the Ostwald ripening that making possible to produce a monodisperse PbS QDs with a narrow absorption peak (20 meV), high PLQY (60%) and exceptional air-stability [39].

The size of Pb-based QDs is tuned from less than 2 nm to 17 nm by adjusting the reaction temperature between RT and 250 °C, enabling emission across the NIR to mid-NIR range as shown in Figure 1.5a [40]. For commercial applications, it is crucial to produce extremely stable QDs because Pb-based QDs are sensitive to changes in the external environment and rapidly undergo oxidation, leading to surface traps/defects and a photo-charging process. An effective strategy like inorganic shell passivation [41], ligand passivation, surface treatment with molecular chlorine [42], and in-situ halide passivation [43] are widely used to enhance the stability of PbS-based QDs. The strong coordination of phosphine ligand (i.e. TOP) to PbS QDs

enhanced the PLQY to 80% and also achieved a better air stability [44]. The ligand passivation has reduced the surface oxidation on exposure to air by preventing contact with oxygen.

1.3.2 III-V semiconductors

From the mid-1990s to date, the synthesis of III-V QDs have been long known to be extremely challenging compared to other types of semiconductors [45]. Generally, the III-V QDs exhibit an amorphous or partially crystalline nature and their oxidation effects; crystallization is improved at high temperatures however it causes irreversible aggregation and precipitation of particles [46]. Researchers have investigated III-V groups QDs, including GaP, InP, InAs, and InSb, which are of particular interest for applications that require Cd/Pb-free QDs. According to a study by Walker and colleagues, the growth mechanism of InP QDs is fundamentally different from that of CdSe and PbSe QDs [47]. In CdSe or PbSe QDs, the growth is limited by the low conversion rate of selenium precursor, while the phosphorus precursor conversion rate precedes the growth of InP, which leads to the broadening of particle size distribution. A highly reactive precursors are used to obtain monodispersed III-V QDs including the tris(trimethylsilyl)phosphine or tris(trimethylsilyl) arsine and is still the most widely used precursor for the synthesis. The drawback of limited selection of precursors and faster consumption of monomers leads to inhomogeneous size distribution. In contrast, Daniel et al. [48] employed less reactive precursors that do not contain Si-P or Si-As bond (tris(trimethylgermyl)arsine ($TMGe_3As$), to improve the size distribution of QDs. Although the particle growth rate is still faster, the less reactivity of $TMGe_3As$ (30x slower) than $TMSi_3As$ has led to a more uniform size distribution. Figure 1.5b shows the absorption spectra of InAs QDs synthesized via the continuous precursor injection method to produce a high mono-dispersion that is comparable to PbS CQDs [49]. More recently, the monomer flux control has gained significant interest for the synthesis of InAs CQDs. In 2021, the synthesis of InAs CQDs by suppression of monomer flux controlled the growth to produce a good size distribution (12.2%) with the first excitonic peak appearing at 1600 nm [50]. Due to the sparse choice of precursors and limited synthetic approaches, group III-V QDs have not yet reached the expected levels in terms of spectral tunability. Systematic studies on the effects of surface chemistry of various organic ligands coordinating III-V semiconductors are still lacking, and developing theoretical models could broaden our understanding of the behaviour of group III-V CQDs.

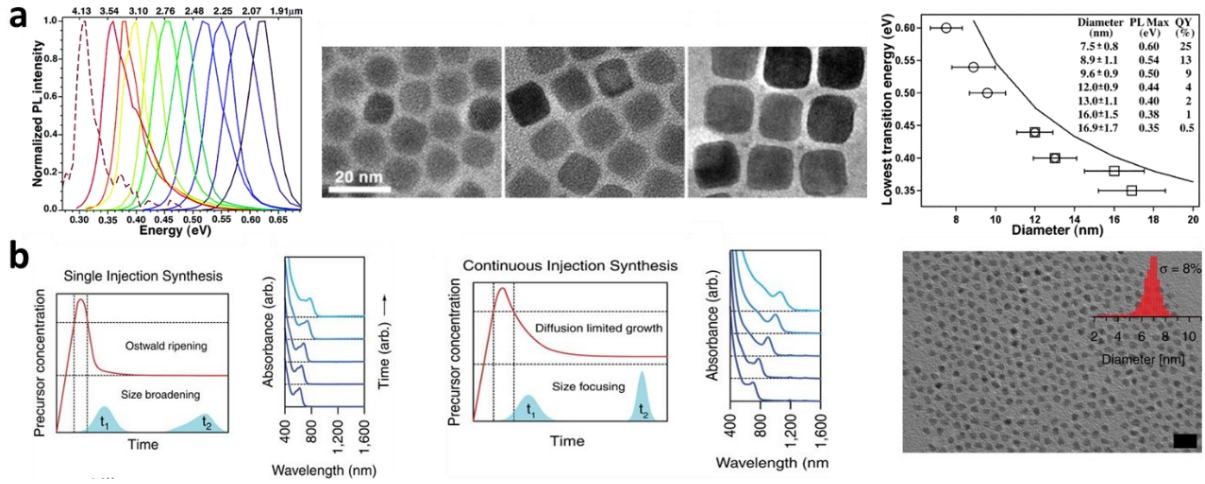

Figure 1.5 (a) PL spectra and TEM images, and Correlation of lowest transition energy with increased PbSe QDs [40]. (b) Temporal evolution of precursor concentration for synthesis of InAs by hot and continuous injection methods and their corresponding Absorption spectra, TEM image of InAs/CdSe/CdS CSS QDs [49].

1.3.3 I-III-VI_2 semiconductors

Over the last decades, InP and other Cd-free QDs are widely studied; however, the complex synthesis route, and narrow emission spectrum restricts their broader application in optoelectronic devices [51, 52]. As an alternative, Ternary I-III-VI_2 QDs (where I = Cu, Ag, Au; III = Al, Ga, In and X = S, Se, Te) are promising due to their outstanding features, including the wide-bandgap tunability [53], long emission time [54], and ease of processability, which makes it attractive for optoelectronic [55] and light-harvesting applications [56]. For I-III-VI_2 QDs, the charge recombination process (Donor-Acceptor pair) is mediated through interstitial point defects that determine the optical properties [57]. Typically, group-I cations have high mobility to form vacancies, accounting for most of the defects [58]. Defect states are domiciles within the band gap that are responsible for charge recombination through the DAP process. In $AgInS_2$, the Indium antisite (V_{Ag}^{-}) and silver vacancy (In_{Ag}^{2+}) in $AgInS_2$ act as the major DAP centers [57]. In photovoltaics, the existence of sub-bandgap states has shown detrimental effects in reducing the power conversion efficiency and open-circuit voltage [59]. Currently, doping Zn into I-III-VI_2 QDs improved the PLQY, contributing to the development of defect-free I-III-VI_2 semiconductors [56]. Indeed, Cu-In-Se QDs synthesized from the commercially available reagents shows deviation from the stoichiometric $CuInSe_2$, i.e. $CuIn_{1.5}Se_3$, $CuIn_5Se_8$ and $CuIn_{2.4}Se_4$ (Figure 1.6a) [60]. Azad et al. [61] produced a high-quality stoichiometric $CuInSe_2$ with near-monodispersion (ca. 4 nm) using TOP as coordinating ligands, CuCl and $InCl_3$. Although the defects related to

non-stoichiometry are eliminated, the complex chemistry of ternary QDs is still under debate, resulting in poor performance of solar energy conversion devices.

1.3.4 Perovskites QDs

Over the past few years, perovskite QDs (PQDs) have been studied intensely because of their interesting properties, such as near-unity PLQY [62], tunable PL maxima (400-800 mm)[63], narrow emission widths [64] and multiple-exciton generation (MEG) [65]. The wide variety of applications of perovskite QDs are solar energy harvesting [66], next-generation lighting [67] and display, and medical imaging [68]. Particularly, a remarkable solar cell efficiency from single digits to 22.1% has been achieved in recent years [69]. The typical PQDs have an ABX_3 crystal structure (A = Cs^+, $CH_3NH_2^+$ (MA^+) or $CH(NH_2)^{2+}$ (FA); B = Pb^{2+}; X = Cl^-, Br^-, I^-) contains a A-site cations inside the cuboctahedral cages of corner-sharing $[BX_6]^{4-}$ octahedron. Substituting the A site cation is possible with other monovalent cations (Na+, K+, Rb+), however it induces structure distortion and reduces the Goldsmicht tolerance factor (>1 or 0.8>), potentially compromising the structural stability [70]. Their cubic or orthorhombic crystal structure are only considered as appealing because of the electronic delocalisation within the crystal structure. The synthesis of PQDs can be performed even at room temperature as it exhibits ionic bonding character. Various approaches have been explored to prepare PQDs in different sizes, shapes and compositions, of which cubes are observed most commonly with edge lengths of 4-15 nm [71, 72]. Emission color of PQDs can be tuned to cover the whole visible spectral range (400-800 nm). The emission peak is tunable by changing size of PQDs under different temperatures, and the obtained PL line widths are narrow with FWHM in the range of 12-42 nm [73] . In addition, PQDs exhibit 90% PLQY even without any surface passivation due to the high-defect tolerance ability of the electronic structure. The two most employed synthetic methods are the RT Ligand-assisted reprecipitation (LARP) method [74] and the conventional HI method [75]. LARP is considered as attractive option due to the mild reaction conditions and easy manipulation compared to HI, which is not suitable for low-cost large-scale production. Louwen et al. [76] synthesized a stable pure-iodine all-inorganic tin-lead (Sn-Pb) alloyed ($CsSn_xPb_{1-x}I_3$) perovskite colloidal QDs using a RT method at open air through spontaneous crystallization strategy (Figure 1.6b). Perovskite QDs are also coupled with metal complexes for photocatalytic systems. Chen et al. [77] synthesized $CsPbBr_3$-Ni(tpy) catalytic system and achieved a high yield in photocatalytic reduction of CO_2 to CO/CH_4. The promising physical and chemical properties of perovskite QDs, combined with continuous design improvements, will lead to the achievement of highly efficient optoelectronic devices in the near future.

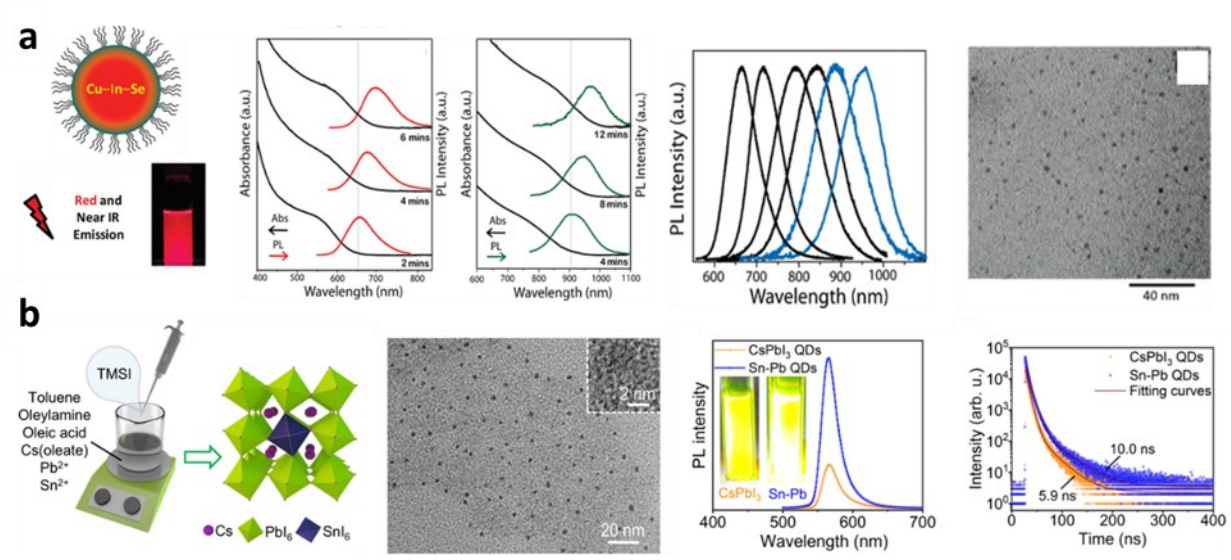

Figure 1.6 (a) Absorption and PL spectra of $CuIn_5Se_8$ and $CuIn_{2.3}Se_4$ QDs with reaction time, PL from red to NIR from $CuIn_5Se_8$, and TEM of $CuIn_{2.3}Se_4$ QDs [60]. (b) Pictorial representation of synthesis of inorganic Sn-Pb alloyed perovskite QDs, TEM image of $CsSn_{0.09}Pb_{0.91}I_3$, PL spectra and PL decay of $CsPbI_3$ and Sn-Pb QDs [76].

1.4 Structure-engineered QDs

The structural engineering of QDs enhances the chemical, thermal and photochemical stability of QDs by removing surface traps/defect states and preserving them from oxidation. This section describes the different core/shell architecture, including the core/shell QDs, core/alloyed shell QDs, and core/multi-shell QDs.

1.4.1 Core/shell QDs

The core/shell QDs exhibit novel optical and electronic properties compared to core-only QDs. Typically, in core/shell QDs, the shell acts as a protective layer and impacts the charge dynamics. Based on the relative band alignment between the CB and VB of core and shell materials, the core/shell structures are categorized into four main types: (i) Type-I, (ii) Reverse Type-I, (iii) Type-II, and Quasi-Type-II that enables a different charge dynamics and stability (Figure 1.7a-d).

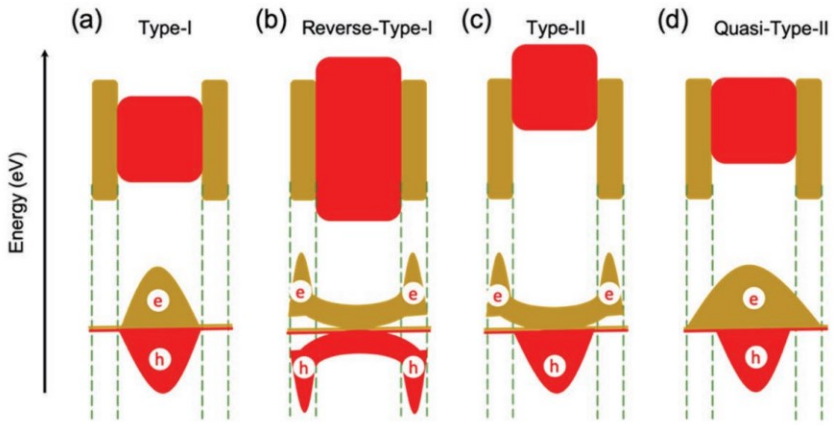

Figure 1.7 Classifiation of core/shell QDs based on relative band alignment of CB andVB edges of core and shell semiconductors (a) Type-I, (b) Reverse Type-I, (c) Type-II, and (d) Quasi-Type-II [20].

In Type I, the CB and VB edge of the core is located inside the shell, such as CdSe/ZnS [78]. The excitons are confined inside the core and the passivation with a larger band gap protects the core from surroundings.

Lian and co-workers [79] demonstrated that the increase in shell thickness for Type-I CdSe/ZnS core/shell QDs decreases the charge separation and recombination rate (Figure 1.8a). Although the shell layer provides stability, it increases the energy barrier for electron tunneling, which does not facilitate the charge transfer. To overcome this, a possible strategy is to increase the band gap of the core via alloying that creates a smaller band offset to facilitate the delocalization of electrons and reduces the overlap of electron/hole wavefunction.

On the other hand, in reverse type-I QDs, the CB and VB band edges of the shell are present within the band gap of the core such as CdS/CdSe [80] and ZnSe/CdSe have (Figure 1.8b). So far, CdSe/CdS QDs are one of the best-developed and most widely studied core/shell QDs systems [81, 82]. Reverse Type-I band alignment leads to partial or complete delocalization of electrons and holes into the shell region [83], which improves the charge extraction and injection rate. Narrowing the band gap of shell material broadens the absorption edge towards a longer wavelength [81].

In type-II QDs, either CB or VB of the shell semiconductor is in staggered configuration with respect to the core. One charge carrier is confined inside the core, while the other is in only in shell region. Particularly, the band energy offset depends on the effective band gap of QDs, which is controlled by changing the size of core and thickness of shell material. In quasi-type-II, either hole or electron is confined in the core, whereas the other is present on the entire core/shell structure, eg. CdTe/CdSe QDs [84] (Figure 1.8c). Zhu et al. [85] show multiple

electron generation (19 e-) from single Quasi Type II CdSe/CdS QD by transient absorption spectroscopy (TAS) under the excitation of 400 nm laser. Such quasi-type-II QDs can be employed to potentially harvest light and charge separation components in artificial photosynthetic systems.

Two different methods were adopted for the synthesis of core/shell QDs: (i) Epitaxial growth approach and (ii) Cation-exchange methods. In the first method, the epitaxial growth of an inorganic shell onto a pre-synthesized core QDs increases the overall diameter of the CQDs while maintaining the inner core diameter [86-88]. In the second method, the exchange of cations from outermost to inner CQDs layers retains the overall core/shell QDs size, the same as the core QDs size [89, 90]. Various geometrical structures can be achieved via cation exchange, which has received much attention in recent years. Type-I systems can be tailored to Type-II by varying the shell thickness and core diameter of semiconductors such as CdSe-ZnSe, ZnTe-CdSe, and CdTe-CdSe. For instance, a thin ZnSe shell over CdSe core yields Type-I while thick ZnSe shell yields Type-II [91]. Conversely, a thick CdSe shell can produce a reverse Type-I band alignment while a thin CdSe shell on a ZnSe core results in Type-I band alignment [83].

For most core/shell QDs, the shell material do not emit light due to the band alignment between core and shell, charge relaxation process, and also the ultrafast non-radiative auger recombination. Haiguang et al. [92] synthesized NIR-active PbS/CdS Zb/CdS Wz QDs, producing independent and simultaneous radiative exciton recombination in both core and shell, respectively. Double colour emitting QDs have been found to be compatible with visible/NIR transparency windows of biosystems and are widely used in chemical and biological sensing applications.

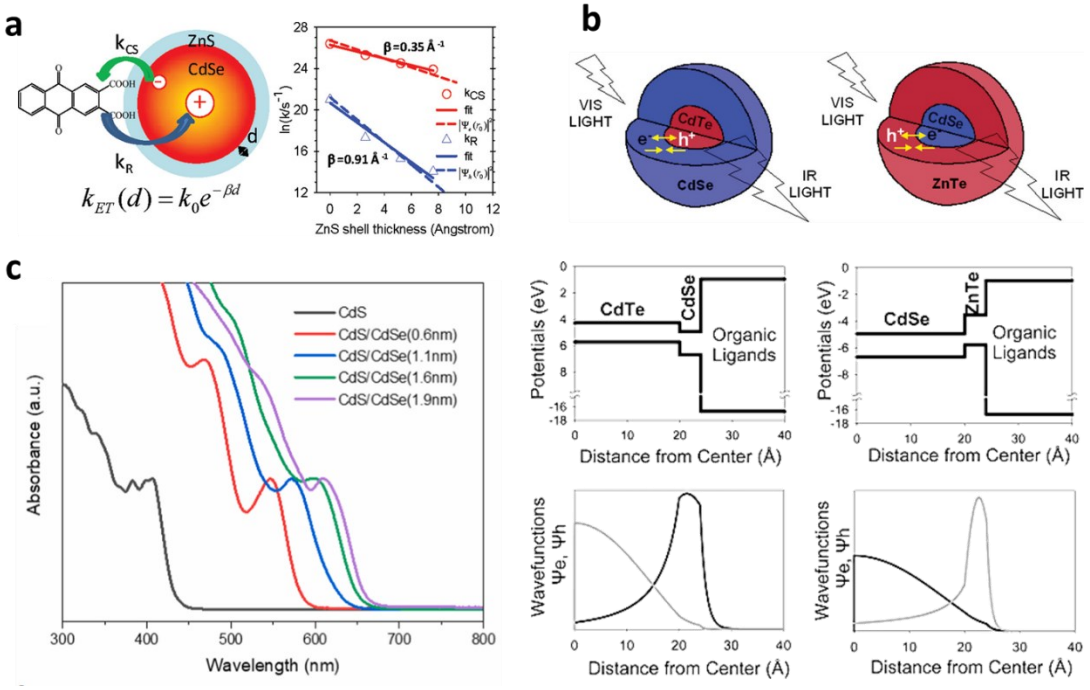

Figure 1.8 (a) The photoinduced charge carrier separation/recombination in CdSe/ZnSe core/shell QDs and their logarithmic plot on changing the ZnS shell thickness [79]. (b) Type-II engineered CdTe/CdSe and CdSe/ZnSe core/shell heterostructures and their corresponding electron and hole radial wavefunctions [84]. and (c) Absorption spectra as a function of shell thickness [80].

1.4.2 Alloyed core/shell QDs

In core/shell QDs, the sharp boundary induces interfacial strains [93]. Typically, the crystallographic mismatch between the constituents results in strain at the interfaces, and therefore, fine-tuning the band-edge energy value and its alignment with neighboring components is often necessary [90]. This can be obtained by constructing a core/shell with a soft boundary via alloyed composition engineering at the core or shell. A composition-dependent band gap energy offers additional tuneability. A $Pb_ySe_{1-y}/PbSe_xS_{1-x}$ CQDs are synthesized in a single-step reaction by utilizing the difference in reactivity between TOPSe and TOPS [94]. This strategy offers control over composition and shell thickness by changing the reaction conditions such as tuning Se/S molar ratio, temperature, and reaction time. Bae et al. [95] show the interfacial CdSeS alloyed layer on CdSe/CdS QDs significantly enhanced the exciton lifetime and suppressed the auger recombination (Figure 1.9a). These advantages highlight the precise tuning of shell composition to form the alloyed shell layer for optoelectronic applications.

1.4.3 Core/multi-shell QDs

The synthesis of QDs with multiple shells was from the challenge to simultaneously satisfy the structural and electronic properties in binary core/shell systems [21, 81]. Particularly, the lattice mismatch between core and shell materials severely restricts the ability to grow a thick shell without compromising the PL properties. To address this, a strain-reducing intermediate shell approach was initially introduced in the CdSe/ZnSe/ZnS core/shell/shell (CSS) system. The ZnSe intermediate layer acts as a lattice adaptor, effectively reducing the interfacial strains between CdSe and ZnS. Talapin and co-workers [96] revealed the high PLQY and higher stability against photooxidation for CdSe/CdS/ZnS CSS QDs compared to CdSe/ZnS QDs (Figure 1.9b). TEM images show uniform shell growth of graded shells and are crucial to reach QYs close to unity [97]. Similarly, a CdS/$Zn_{0.5}Cd_{0.5}S$/ZnS prepared via SILAR technique showed high PLQY of 80% and improved stability compared to binary core/shell QDs [98]. In a different approach, CdSe/ZnSe double shell overcoated InAs QDs exhibit high QYs (70%) over the IR region (800-1600 nm) [99].

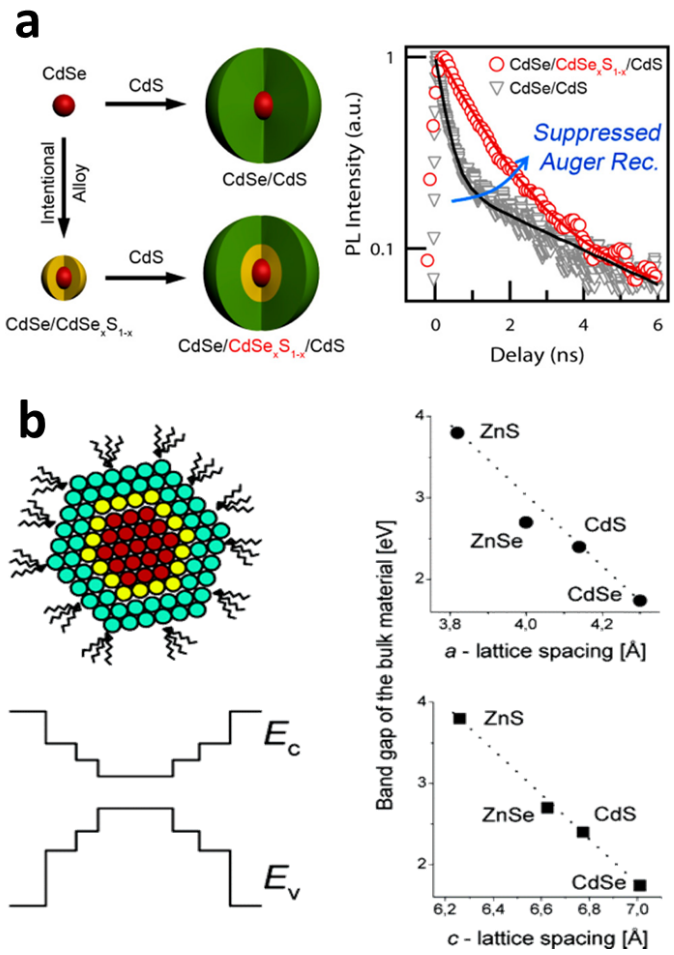

Figure 1.9 (a) Schematic representation of CdSe/CdSe$_x$S$_{1-x}$/CdS core/alloyed shell QDs and the PL decay curve [95]. (b) core/multi-shell QDs and comparison of their band gaps in bulk and QDs [96].

1.5 Dopant-engineered QDs

Doping QDs with transition metal ions possess distinct optical, electronic and photophysical properties that are advantageous over undoped QDs, including the large Stokes shifts to prevent re-absorption losses, greater thermal and chemical stability, broader spectral window, and longer excited-state lifetimes, [100]. Dopants introduces new electronic states between the band edge of the QD's which alters the charge separation and recombination dynamics [100]. In addition, the optical and electronic properties of QDs can be tuned through controlling the type and concentration of dopants [101]. So far, the transition-metal ions such as Mn, Cu, or Ag have mainly been introduced as dopants in II–VI type QDs (ZnSe, ZnS, CdS, and CdSe) or ternary QDs (ZnCdS, CuInS, ZnInS, and AgInS) [102, 103]. Tradition synthetic methods to prepare doped CQDs involve the reaction system with both competitive host ions and dopant ions, which

is challenging to control and optimize. It produces large portion of undoped QDs, as revealed from their emission spectra. In this context, Naryan et al. [104] adopted a new strategy of decoupling the doping process from nucleation and/ or growth via nucleation-doping and growth-doping. In principle, this allows to control the radial position of dopant ions in host nanocrystals. Nucleation-doping would place the dopants away from the potential surface trap states to improve the optical properties. In Mn:ZnSe QDs, the excess Se (Mn:Se – 1:25) aids in the formation of smaller stable MnSe nanoclusters, while a low precursor ratio produces large-sized MnSe nanocrystals due to continuous growth. The following section will provide an understanding of different doping strategies and their effect on the optical and electronic properties of the QDs.

1.5.1 Mn doping

Doping of Mn^{2+} in wide band gap semiconductor is known widely for its unique yellow-orange emission centred within 580-600 nm [105]. The distinct feature of this emission is the longer excited-state decay lifetime that identifies the origin from Mn^{2+} [106]. Over last 30 years, the Mn doped QDs are studied widely and achieved significant milestones from doping it in chalcogenide and extending to emerging perovskite nanocrystals [107-109]. Bhargava and co-workers first reported research on Mn doping in ZnS and presents the intense Mn d-d transition [106]. Later, the work of the high-temperature organometallic synthesis route reported by Bawendi and coworkers [6] directed the successful doping in ZnSe and included a discussion on the position of the Mn^{2+} ion inside host material [110]. Then, many fields emerged, and intense research was conducted to understand the physical insights of doping, doping concepts, optical characteristics of doped QDs, diffusion doping and phase-selective doping [100, 111]. Although ZnS was first used as host [106], doping Mn was extended to different binary, ternary, alloyed and even other complex nanostructures. The important findings such as size dependant evolution based on Mn d-d emission in CdSe [112], temperature-dependent emission [100], doping in multinary $AgInS_2$–ZnS and $CuInS_2$–ZnS systems [113], efficient doping in alloy nanocrystals, and thermal stability in doped ZnSe etc. Also, the synthetic parameters can be tuned by employing different spectroscopical methods, have led to extensive study to understand the origin of exciton dopant energy transfer responsible for the spin inverted d-emission. Based on theory, the Mn emission is non-tunable but it can be possible by altering the ligand field energy that offers the emission tunability (>50 nm spectral window). These Mn doped QDs are explored in various fields such as bioimaging [114], photovoltaics [115],

fluorescence resonance energy transfer [116], solar concentrators [117], and solar water splitting [118].

1.5.2 Cu doping

Copper (Cu) doping in CQDs has gained much interest in recent years. Unlike Mn-doped QDs, where the emission wavelength range of the dopant is restricted to the yellow-orange region due to the intrinsic transition between the $^4T_1$ and $^6A_1$ d-states, Cu dopants can exhibit a wide spectral range depending on nature, size, and host composition. For instance, Cu:ZnS exhibit blue-green emission [103], Cu:ZnSe show green to yellow emission [101], Cu:CdS in orange to red [119], and Cu:InP in near-infrared [120]. Most of the reported research suggests that Cu enters the lattice in +1 oxidation state and replace the atoms in the lattice. Few other works suggested the existence of Cu in +2 oxidation state, thereby creating a hole affecting the PL properties of host nanocrystals. The doping of Cu into bulk semiconductors where the acceptors and donor levels are identified in the band gap of semiconductors is different from the QD systems. For Cu:CdSe QDs, the UPS measurements showed the observations of Cu d levels near the VB edge. It exists as Cu^+ oxidation state substituting the cationic Cd sites according to X-ray absorption near-edge spectroscopy (XANES) [121]. A Cd-free Cu doped ternary Zn-In-S QDs were prepared using a one-pot non-injection synthetic approach. Such composition tunable Cu:Zn-In-S allows tunable PL emission from visible to NIR (450-810 nm) with high PLQY (85%) [122]. Jun et al. [56] synthesized high-quality oleyl amine capped Zn-Cu-In-Se alloyed QDs with broad absorption onset extending to ~1000 nm, and the resulting QD sensitized solar cells show PCE of 11.91% under 1 sun illumination. An efficient Cu doped InP QDs synthesized by epitaxial growth of ZnSe as a dopant diffusion barrier, wherein the emission range covers from 630 nm to 1100 nm with high PLQY (35-40%) [120]. Xia et al. [123] demonstrated the simultaneous incorporation of Cu into the AgInSe core and ZnSe shell, and the fabricated QDs-based PEC device exhibited a high photocurrent density of 9.1 mA/cm^2. Therefore, Cu-doping are of great potential in advancing the properties of QDs for optoelectronic applications.

1.5.3 Lanthanide ion doping

In past decades, the investigations on lanthanide-doped QDs are growing because energy transfer property present in Lanthanide ions (Ce^{3+}, Er^{3+}, Tb^{3+}, Nd^{3+}) show significant impact on luminescence efficiency. Most representative host material used for La doping are CdS, ZnS and ZnO. Generally, lanthanide doping is more challenging than with transition metal ions (such

as Cu and Mn) because of the significant differences in ionic radii and charge between lanthanide ions and the host cations in QDs. The mechanism behind the incorporation of lanthanide ions into the host lattice (such as ZnS or CdS) remains a subject of ongoing debate. The PL emission characteristics depend on the location of Lanthanide dopants in the host lattice. For instance, in Eu doped ZnS QDs, Eu^{3+} ions are adsorbed on the surface rather than into the bulk ZnS nanocrystals, as indicated by the absence of ZnS host absorption at 340 nm in the excitation spectrum of Eu^{3+} emission. Nevertheless, on exciting with 929 nm laser, a strong up conversion luminescence from Eu^{3+} in Eu-doped ZnS QDs shows efficient energy transfer from the host to the dopant [124]. Depending on the synthesis conditions, Lanthanide ion-doped QDs exhibit PL lifetime in micro/milli second scale [125]. The longer excited state lifetime of lanthanide-doped QDs is beneficial for time-resolved applications in bio-related fields.

1.6 CQDs as tunable light absorbers and emitters

1.6.1 CQDs as light absorbers for photoelectrochemical (PEC) devices

1.6.1.1 Working principles

In a typical PEC device, one of the photoelectrodes serves as the working electrode to capture light energy from solar radiation. This can occur either through a photoanode, where electrons act as the mobile charge carriers, or through a photocathode, where holes function as the mobile charge carriers (Figure 1.10a) [126]. The counter electrode is where the other half-reaction takes place. A tandem photoanode-photocathode pair is a more complicated configuration in PEC cells, involving both oxidation and reduction reactions. These electrodes are dipped into an electrolyte and linked to an external electrical contact. At the electrolyte/electrode junction, the chemical potential difference leads to the charge transfer process, creating a flow of electric current until an equilibrium is established [127]. The fermi level of the semiconductor electrode and the electrolyte are aligned, causing band bending in the semiconductor [128]. Upon light illumination, several crucial steps occur in PEC systems which are as follows (photoanode as an example) : (I) Generation of electron-hole pairs after photons absorption with energy larger than band gap (E_g) of semiconductor, (II) Charge carrier separation (electron-hole pairs) based on built-in electric field, (III) Electrons are directed towards the outer circuit to counter electrode and the holes under the oxidation reaction, (IV) Charge carrier recombination [129], and (V) Redox reaction (Figure 1.10b) [128]. To realize an

efficient PEC H_2 production, the photoelectrode, which is the heart of the PEC cell should satisfy the following requirements:

a) band gap of the semiconductor should be appropriate for broader absorption of light with maximum overlap with solar spectrum.

b) The separation of electron-hole pairs generated should be effective.

c) The charge transfer process should be faster than charge recombination.

d) PEC water splitting requires high energy input (uphill reaction) $(H_2O\ (l) \rightarrow H_2(g)\ + \frac{1}{2}\ \ O_2)$. The CB potential of the semiconductor should be more negative than 0.0 V vs NHE (H^+/H_2), and the VB should be more positive than 1.23 V vs NHE (O_2/H_2O). On considering the energy losses, the semiconductor's band gap should be larger (1.7 eV at room temperature) [130].

e) The photoelectrodes should be chemically stable and resistant to corrosions at dark and light conditions in aqueous solutions.

f) Semiconductor materials should be low-cost and easy to prepare.

Since the breakthrough discovery of PEC water splitting by Fujishima and Honda in 1972 [131], a significant effort have been made to realize high-performance photoelectrodes that exhibit high solar-to-hydrogen (STH) efficiency, and operational stability [132]. However, until now, no single semiconductor photoelectrodes is found that can fulfill all the requirements simultaneously. Various investigations have focused on heterojunctions with a light-absorbing material (organic dyes [133], metal complexes[134]) and bulk semiconductors (TiO_2, C_3N_4) [135]. Last few decades, QDs-based PEC devices have made considerable progress while the overall STH efficiency is still below the commercial level expectations (STH >10% with long-term stability >1000 h) [136], due to the inability of semiconductor to generate sufficient charge carriers, non-radiative charge recombination channels, and slower rate of charge injection from QDs to charge acceptors [137]. To tackle these problems, it is crucial to focus on the design and synthesis of QDs with proper band structure and light absorption range, improving the loading of QDs on photoelectrodes, and surface engineering the photo electrodes to improve charge transport and establish long-term stability.

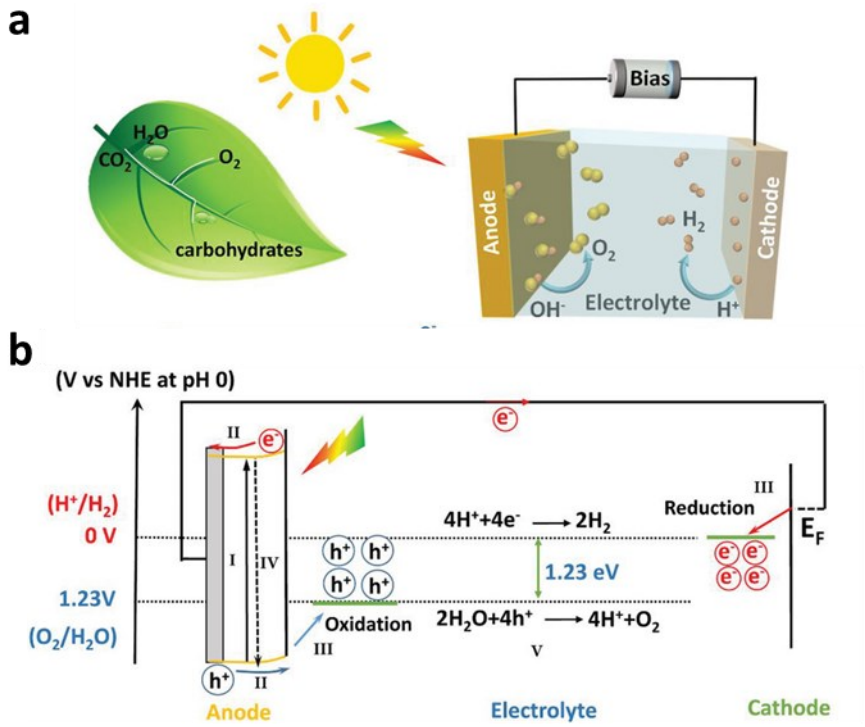

Figure 1.10 Schematic illustration of (a) Typical PEC water splitting system. (b) Charge carrier dynamic in photoanode based PEC system [138].

1.6.1.2 Challenges

(i) Light absorption efficiency

The charge carrier generation is the first key step in the PEC reaction, where extending the light absorption edge is crucial to harvesting maximum photons for enhancing the STH efficiency [139]. In this context, visible light-active chalcogenide-based QDs are considered as promising candidates because of their simple synthesis procedure and favourable band structures [140]. In terms of solar light energy distribution on earth's surface, the visible and NIR light range accounts for 50% whereas UV light is only about <5% of the entire solar spectrum [141]. Therefore, narrow band gap QDs can be suitable for utilizing the optimal range of solar spectrum, including the Pb chalcogenide-based QDs with band gaps (1.1-1.8 eV)[142]. For instance, PbS QDs (active in UV, visible and NIR) deposited TiO_2 yields an 1.15% STH efficiency with sacrificial agents [143]. Nevertheless, the light absorption range was compensated with the reduction in driving force to inject the electron due to the smaller band offsets between TiO_2 and PbS QDs. To elevate the high charge injection rate, co-sensitizing strategy was adopted to improve photon collection. A sequential deposition of CdSe QDs on CdS QDs-ZnO nanowires increases the photocurrent density, which is attributed to the step-

wise band alignment (CdSe/CdS/ZnO) and greater light absorption [144]. The competitive intake by each-co-sensitizer was still an issue to be resolved by enhancing the design of QDs. The strategy to overcoat a shell on QDs has improved the light-harvesting ability. Jin et al. [145] developed SILAR-based PbS/CdS core/shell QDs, which show broad NIR absorption (400-1030 nm) and greater light absorption, resulting in improved photocurrent density to 11.2 mA/cm^2. Although the shell improved performance, the drawbacks of the SILAR-based method, such as high time consumption and poor QDs coverage, intensified the progress of developing colloidal thick-shell QDs. In colloidal core/thick-shell QDs, the absorption range of QDs is governed by the shell type and thickness. For example, replacing the ZnS shell with CdS shell extended the absorption from 400 nm to 600 nm [146]. However, due to the wide band gap of the shell (CdS - 2.42 eV and ZnSe 3.25 eV), most thick shells have limited light absorption, typically below 600 nm. Generally, alloying the QDs can increase the absorption. Few examples of alloyed QDs includes the TiO_2/CdS_xSe_{1-x} [147], $ZnO/Zn_xCd_{1-x}Se$ [18], and $ZnO/Zn_xCd_{1-x}Te$ [148]. Zhao et al. [149] synthesized $CdSe/CdSe_{1-x}S_x/CdSe$ core/alloyed shell QDs show improved absorption up to 650 nm. These observations indicates that alloying core or shell could offer new opportunities in extending the light harvesting abilities to utilize broader absorption range from the solar spectrum.

(ii) Charge transport efficiency

Charge separation and transport are crucial aspects apart from light absorption efficiency in PEC systems. Metal oxides with larger band gaps have been widely studied as electron transporting materials and host material for PEC systems due to their low-cost, environmentally friendly property functional electrochemical stability, high electron transfer ability, and suitable band edge potential for water splitting [150]. The host materials such as mesoporous films suffers from severe charge recombination issue due to its wide band gap nature [151]. To alleviate this issue, supporting the host semiconductor with high conductive materials are considered as an effective strategy that can provide a direct pathway for faster electron transfer between the solid/liquid interface to produce high photocurrent density. Examples include the TiO_2 combined to 1D graphene nanoribbons [152], multi-walled carbon nanotubes (MWCNTs) [153], Au-MWCNTs [154], and metal-organic frameworks (MOF) [155]. In addition, tuning the morphology (nanotubes, nanorods, and nanowires [156]) have also facilitated the charge transfer without the grain boundary challenges.

(iii) Material stability and charge dynamics

Colloidal QDs often suffers from surface sensitivity to external environments such as moisture, light, temperature, surface ligands, and oxygen due to high-surface area to volume ratio [28]. It

can induce charge traps/defects, which results in a more undesirable recombination pathways and, consequently, decreased photo/chemical stability as well as greater loss in photocurrent density contributing to the PEC performance. In this regard, developing a suitable inorganic shell for capping the core was devised to mitigate the loss of QDs properties from degradation, and it also tunes the charge dynamics. Kim et al. [102] used SILAR based method to deposit Mn-CdS shell on PbS QDs which improved the light absorption from 400-800 nm. However, their initial high photocurrent (22.1 mA/cm^2) drops rapidly (55% of the initial value) within 5 min of continuous illumination, possibly due to the interfacial surface trap states that occur from SILAR deposition [143]. To address this issue, colloidal core/shell QDs are pre-synthesized, which passivates the uncoordinated bonds present on the QDs' surface, improving the chemical, thermal and photochemical stability. A TiO_2 photoanode using thick-shell CdSe/CdS QDs maintained 57.5% of its photocurrent density after illuminating for 2 h, which is better than the bare CdS QDs (42.1%). Shell thickness influences the charge dynamics in core/shell QDs. For example, the increase in shell thickness for CdSe/CdS QDs reduces the hole transfer rate 4-5 times compared to CdSe QDs. Interfacial gradient alloyed shell layer has proven to exhibit higher electron-hole transfer rate which modifies the confinement potential to achieve a record photocurrent density of 17.5 mA/cm^2 [157]. These efforts open opportunities to achieve both optimal stability and efficient charge transfer simultaneously.

(iv) Developing heavy-metal free QDs based PEC device

Most high-performance QDs contain heavy metals (Cd, Hg and Pb) or employ heavy metals during the process of QDs preparation, which limits the large-scale deployment of QDs-based photoelectrodes. Apart from focusing on stability and efficiency, developing heavy-metal free QDs based photoelectrodes also play crucial role for commercial application.

Eco-friendly carbon dots-based photoelectrodes have the potential for a broad light absorption range and other advantages such as earth abundance, chemical stability, cost-effectiveness and broad optical absorbance [158]. While the current density is far low (<4 mA/cm^2) because of relatively severe charge recombination [159]. A NIR-active SnSe QDs-TiO_2 photoanode synthesized by template-assisted cation exchange approach exhibit a photocurrent density of 8.2 mA/cm^2 [160]. However, Sn^{2+} gets easily oxidized to Sn^{4+} state which forms as an impurity during the fabrication process, affecting the H_2 production. In addition, the synthesis of Sn-based QDs involves using Cd. As an alternative, the ternary semiconductors have received recent attention and investigated widely due to their low-toxicity, cost-effective, composition tunable optoelectronic properties, and appropriate band potential for water reduction. Nevertheless, the defects induced charge traps in I-III-VI_2 QDs that affects the PEC

performance is one of major challenge to tackle. Non-colloidal NIR QDs produced via molecular beam epitaxy demonstrated high current densities (18 mA/cm^2), but this method involves complex and costly deposition techniques [161]. Tong et al. [162] synthesized colloidal $CuInS_2$/ZnS core/thin shell QDs, resulting QDs-PEC device show high photocurrent density (5.3 mA/cm^2). A thick shell has proven effective in suppressing the charge recombination for improved PLQY and the exciton lifetime of ternary I-III-VI_2 QDs. Li et al. [163] synthesized $CuInSe_xS_{1-x}$ alloyed graded interfacial layer into $CuInSe_2$/$CuInS_2$ QDs and achieve 70% improvement in photocurrent density. In future, engineering the heavy-metal free QDs should concentrate at engineering the surface and interface of I-III-VI_2 QDs.

1.6.2 CQDs as light emitters for optical anti-counterfeiting devices

The advancing modern science and technology have made everyday life convenient for people but also brings counterfeiting as an effortless job for fraudsters [164]. Counterfeit goods with widespread prevalence disrupt normal economic growth, cause huge economic losses and have adverse effects on human life. The global brand counterfeiting (GBC) reports a worldwide economic loss of 3 trillion USD caused by counterfeiting in 2022 and an exponential rise is expected [165]. Therefore, the design and development of high-security anti-counterfeiting (ACF) technology is crucial to improve the document protection, prevent counterfeiting and replication. Although various anti-counterfeiting techniques and materials, including laser holograms, radio-frequency identification, watermark technology, nuclear track technology and so on, have been developed, luminescent printing has been widely used due to its easy operation, designable and high-throughput production. Luminescent anti-counterfeiting materials using semiconductor quantum dots, photonic crystals, and up-conversion nanomaterials attracted much attention among researchers to pave way for more advanced anti-counterfeiting patterns.

1.6.2.1 Working Principles

Luminescence-based anticounterfeiting involves incorporating luminescent materials that emit light when exposed to external stimuli [166]. Luminescent materials are engineered to respond uniquely under various conditions that makes counterfeiters difficult to replicate the authentic items [167]. Semiconductor QDs [168], organic dyes [168], Yb/Er-carbon dots [169], perovskite [170], and Ln^{3+} doped nanoparticles [167] are the excellent luminescent materials which can be excited by external stimuli such as light, heat, mechanical force, and chemical reagents. For

instance, the $CsPbBr_3$ produces green fluorescence under UV light, while the Ln^{3+} doped NPs can be tuned to different color by changing the excitation wavelength [171, 172]. Generally, based on the number of external stimuli, the luminescence anticounterfeiting are classified into three levels: (i) Single level, (ii) double level, and (iii) multilevel anticounterfeiting. Single-level anti-counterfeiting is the simplest luminescence anticounterfeiting mode, which is applied widely to various currencies and certificates. According to various luminescence modes, single level anti-counterfeiting is divided into chemiluminescence PL, up conversion (UC) PL and down conversion (DC) PL anti-counterfeiting [173]. DC PL anticounterfeiting is realized by absorption of high energy photons and releases low-energy photons [174]. Currently, different materials are used in single-level DC PL anti-counterfeiting, including carbon dots, organic luminogens, cellulose nanofibrils/CdTe QDs, Nitrogen doped carbon dots, Tb^{3+}/Eu^{3+} grafted melamine cyanurate, and $SrAl_2O_4:Eu^{2+}$. QDs based composite materials that offers promising features for more precise, complex and high-dimensional anticounterfeiting patterns, which have been of great interest compared to single monochrome low-level anticounterfeiting materials.

1.6.2.2 Challenges

In today's era, the main drawback of luminescent anticounterfeiting materials are their susceptibility to damage when exposed to environmental factors such as pH, humidity, and temperature. The degradation of luminescent materials under varying environmental conditions restricts their practical application across diverse environments. Sensitivity to these factors leads to loss of encrypted sensitive information. Researchers work continuously to overcome these limitations by fabricating stable materials to provide better protection against environmental factors. Xu et al. [170] demonstrated high storage stability (60 days) and thermal stability (150 °C) for Cs_4PbBr_6/SiO_2 protected $CsPbBr_3$ nanocrystal based anti-counterfeiting security labels. Ding et al. [175] designed UC $NaGdF_4$:Yb/Ho/Ce@$NaYF_4$:X (X = Eu, Tb, Sm, Dy) core–shell nanostructures as an efficient and multicolor-tunable dual mode emitters for anti-counterfeiting. Nevertheless, UC materials based on lanthanide elements (Ce, La, Gd, Eu, Tb) are expensive, and their complicated synthesis obstructs its real-time applications. Metal chalcogenide-based QDs exhibit promising emission performance and offer composition/size tunability, which provides a broader emission wavelength to cover the entire visible light region. Chen and their co-workers [176] reported the CdTe/ZnS-2-polyamidoamine hybrid using microfluidic printing methods; the printed pattern response in green and red colors under UV light. Liu et al. [177] developed an II-VI colloidal QDs-based Red-green-blue (RGB) emitting fluorescence security inks. The fabricated security labels are invisible under the naked eye but

can be visualized under UV light, and further, the AI-based authentication strategy makes it very promising for sensitive industries such as the Nuclear one. However, for commercialization, these security labels should not contain toxic elements like Cd and Pb. Consequently, developing alternative, heavy-metal-free QDs for anticounterfeiting applications is important to ensure safety and environmental sustainability.

1.7 Thesis objectives and contribution

Based on my literature review, significant challenges have been identified to design and develop an efficient heavy-metal free colloidal core/shell QDs, including reducing the surface charge recombination, modulating PL emission characteristics, and charge carrier dynamics as desired for the two key applications, i.e. PEC H_2 production and optical anti-counterfeiting devices. Surface engineering the QDs by finding a suitable shell material that ensures to provide both stability and better charge generation/separation is crucial for high-performance QDs-based PEC H_2 production. In optical anti-counterfeiting devices, modulating the PL characteristics by utilizing dual dopants along with shell passivation could enhance the security features and provide ultra-stability against environmental degradation, which are essential for practical application. Therefore, the objectives of my thesis are as follows:

I. Photoelectrochemical H_2 production

The first project is focused on the design and synthesis of heavy-metal-free ZnSeS alloyed shell passivated ternary Cu doped $ZnInSe_2$ QDs for solar-driven PEC H_2 production. The objective is to prevent surface traps/defects and tune the charge carrier dynamics of Cu-$ZISe_2$ core QDs by an in-situ shell passivation approach. This approach can effectively mitigate the undesired charge recombination and provide a suitable band alignment for charge transfer. The as-synthesized Cu-$ZISe_2$/ZSeS QDs photosensitizers on wide band gap mesoporous TiO_2 semiconductor thin films were employed as photoanode for PEC H_2 production. In addition, the MWCNTs are incorporated to improve the charge transport properties for enhanced and stable PEC H_2 production.

II. Optical anti-counterfeiting application

The second project is to synergistically modulate the optical properties of heavy-metal-free $ZnInSe_2$/ZnSe core/shell QDs by incorporating Cu-doping and Mn-alloying into their core and shell to investigate their use in anti-counterfeiting and information encryption. The QDs were introduced on PMMA polymer to form smart concealed inks for both writing and printing patterns. We studied the durability of the printed patterns by exposing them to varying

temperatures and water-soaking tests. A mechanism was proposed to understand how dopant interactions modulate the emission characteristics of anti-counterfeiting security inks.

1.8 Thesis organization

Chapter 1 presents the research background of this thesis and provides an overview of the research problem, motivation, and objectives for each project undertaken.

Chapter 2 describes the materials used, and the characterization techniques employed to study the physiochemical properties of the synthesized QDs in detail.

Chapter 3 discusses the design and fabrication of heavy-metal-free Cu-$ZnInSe_2$/ZnSeS based on a gradient alloyed shell using an in-situ shell passivation approach. The chapter highlights the significant enhancement in PEC performance and stability through improved charge transfer kinetics and reduced charge recombination, supported by experimental and theoretical studies. The influence on PEC performance after incorporating an electron transport layer (MWCNTs) was also examined.

Chapter 4 considers a novel approach on dual dopants (Cu, Mn) engineered heavy-metal-free $ZnInSe_2$/ZnSe core/shell QDs to tune the optoelectronic properties for their use in anti-counterfeiting and information encryption. The durability of the printed patterns was examined by exposing to varying temperatures and water-soaking tests. The invisible anti-counterfeiting security features was identified by printing it on different surfaces. A mechanism was proposed to understand the dopant interactions that modulate the emission characteristics of anti-counterfeiting security inks.

Chapter 5 briefly summarizes the findings of the Master's research work and discusses the future challenges and outlook of this emerging field.

CHAPTER 2. MATERIALS, METHODOLOGY AND CHARACTERIZATION

This chapter introduces the synthesis of colloidal Cu:$ZnInSe_2$ QDs, Cu:$ZnInSe_2$/ZnSeS core/alloyed shell QDs, and Cu:$ZnInSe_2$/Mn:ZnSe core/shell QDs. The fabrication of QDs-based photoanode and QDs-based security inks for PEC H_2 production and anti-counterfeiting applications are then discussed. After that, the chapter covers the different PEC measurements conducted to evaluate the performance of QDs based photoanode for solar-driven H_2 production. For anti-counterfeiting application, the details of the studies performed to determine the stability of labels created using QDs based security inks are presented. Different characterization techniques are used to investigate, study, and validate the observations and experimental results of this thesis work. This section also contains a discussion about the working principle and instrumentation of these characterization techniques.

2.1 Materials

QDs synthesis: Zinc acetate ($Zn(OAc)_2$, 99.99%), Indium (III) acetate ($In(OAc)_3$, 99.99%), Selenium powder (Se, 100 mesh ≥99.5%), Sulfur (S, ≥99.5%), Copper (II) acetate monohydrate ($Cu(OAc)_2 \cdot H_2O$, ≥98%), Manganese acetate ($Mn(OAc)_2$, 98%), Zinc acetate dehydrate ($Zn(OAc)_2.2H_2O$), 1-octadecene (ODE, 90%), 1-dodecanethiol (DDT, ≥98%), Trioctylphosphine (TOP, 97%), Oleyl amine (OLA, 70%), dichloromethane (≥99.8%), Tetraethyl orthosilicate (reagent grade, 98%), hexane (anhydrous, 95%), toluene (anhydrous, 99.8%), methanol (anhydrous, 99.8%), and acetone (99.5%) were obtained from Sigma-Aldrich, USA.

PEC device fabrication: ZrO_2 powder, multi-walled carbon nanotubes (average length/diameter - 10 µm/12 nm) (MWCNTs), alpha-terpineol, sodium sulfide nonahydrate ($Na_2S.9H_2O$, ≥98.0%), sodium sulfite (Na_2SO_3, ≥98%), and Ethyl cellulose were obtained from Sigma-Aldrich, USA. Titania paste containing larger anatase scattering particle (18NR-AO, diameter up to 450 nm), Ti-Nanoxide T/SP, Ti-Nanoxide BL/SC were purchased from Solaronix SA, Switzerland. FTO conductive glass (square resistance: 6Ω, Transmittance: ≥82%) was purchased from South China Xiangcheng Technology Co., Ltd, China.

Anti-counterfeiting device fabrication: Poly(methyl methacrylate) (PMMA, average molecular weight – 996,000 by GPC), and toluene (≥99.5%) was purchased from Sigma-Aldrich, USA.

All the chemicals were used as received without any modification.

2.2 Methodology

2.2.1 Synthesis of QDs for PEC H_2 production

Cu-doped $ZnInSe_2$ core QDs : Cu doped $ZnInSe_2$ ($CZISe_2$ core QDs) was prepared using the procedure described earlier [178]. Hot injection technique was adopted to prepare the colloidal QDs (Figure 2.1). To synthesize $CZISe_2$ core QDs, $Zn(OAc)_2$ (0.16 mM), $Cu(OAc)_2 \cdot H_2O$ (0.04 mM), $In(OAc)_3$ (0.64 mM) were added to the solution of ODE (5.0 mL), OLA (1.0 mL), and DDT (1.0 mL) into a three-neck round bottom flask. The mixed solution was degassed under a N_2 flow and stirred for 5 min. Subsequently, the solution was heated to 130 ℃ to form a clear solution under N_2 flow and kept for 20 min. Then the solution was further degassed for 20 min to remove the organic volatile compounds and water molecules. Meanwhile, the Se stock solution was prepared by mixing Se powder (0.35 mmol, 27.6 mg), OLA (0.5 mL), DDT (0.5 mL), and ODE (6.0 mL) solution by ultra-sonication for 80 min at room temperature. The reaction temperature was elevated to 200 ℃, and the Se stock solution was immediately injected to trigger the formation of $CZISe_2$ core QDs. The reaction growth time was kept for 30 min to obtain $CZISe_2$ core QDs. The obtained product was precipitated by adding excess acetone. Toluene of appropriate volume (1:1, QDs:toluene) was added to redisperse the QDs which is followed by adding acetone for precipitation. This process was repeated 3 times to remove the unreacted compounds and obtain high-quality purified QDs. Finally, the purified QDs was dispersed in toluene for optical and structural characterization. Toluene is used because it provides long-term stability due to its higher dielectric constant.

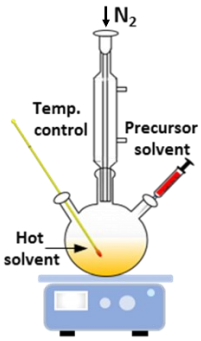

Figure 2.1 Typical scheme of setup hot-injection technique for CQDs synthesis.

Overcoating ZnSeS shell on the $CZISe_2$ QDs: The $CZISe_2$/ZnSeS core/shell QDs was synthesized with slight modifications to the previous literature [179, 180]. First, the $Zn(OAc)_2$ stock solution was prepared by dissolving 73 mg $Zn(OAc)_2$ in 5 mL ODE, 1 mL DDT, and 1 mL OLA. Then, 28 mg Se powder and 28 mg Sulfur powder were dissolved separately in 2 mL TOP by ultra-sonication to form TOP-Se and TOP-S complexes. From the stock solutions, 7 mL $Zn(OAc)_2$, 0.1 mL TOP-Se and 1.9 mL TOP-S were sequentially injected into $CZISe_2$ core-containing solution at 200 °C. After heating to 235 ℃ for 30 min, the $CZISe_2$@ZnSeS core/shell QDs was obtained. To purify the product, the same procedure was followed until the QDs were purified sufficiently for about 4 times.

2.2.2 Synthesis of QDs for optical anti-counterfeiting device

Cu-doped $ZnInSe_2$ core QDs: The Cu:$ZnInSe_2$ QDs was prepared using the same procedure described in section 2.2.1.1. In addition, the undoped $ZnInSe_2$ QDs were synthesized without the addition of Cu precursor**.**

Overcoating ZnSe shell on the Cu:$ZnInSe_2$ QDs: $Zn(OAc)_2$ (73 mg, 0.4 mmol) was dissolved in a mixed solution of OLA (1.0 mL), DDT (1.0 mL), and ODE (5.0 mL) at 50 ℃ under an N_2 atmosphere. The $Zn(OAc)_2$ solution was injected into the obtained raw solution of Cu:$ZnInSe_2$ core QDs. Subsequently, the sonicated Se stock solution containing Se powder (0.35 mol, 28 mg) in the mixture of OLA (0.5 mL) and DDT (0.5 mL) was injected into the above solution. The solution was heated to 220 ℃ for 1 min to form Cu:$ZnInSe_2$/ZnSe core/shell QDs.

Mn^{2+} doped shell on the Cu:$ZnInSe_2$/ZnSe QDs:

$Mn(OAc)_2$ (7 mg, 0.04 mmol) was dissolved along with $Zn(OAc)_2$ stock solution by heating the mixed solution at 50 °C under N_2 flow. The solution was injected into the raw solution of Cu:$ZnInSe_2$ QDs at 200 °C. The reaction temperature gradually increased to 220 °C and kept for 1 min to obtain Cu:$ZnInSe_2$/Mn:ZnSe. The Cu:$ZnInSe_2$/ZnSe, $ZnInSe_2$/Mn:ZnSe and $ZnInSe_2$/ZnSe core/shell QDs were synthesized using the same procedure. The obtained QDs were precipitated by adding acetone and centrifuged at 8000 rpm for 10 min, then washed twice with a mixture of hexane and acetone. Finally, the precipitate was re-dispersed into the toluene solution for further characterization.

Novelty of methodology: Studies on ternary Cu based QDs are not well-advanced due to the lack of suitable synthetic methods for producing QDs with sizes below the Bohr excitonic radius of ~10.6 nm [181]. Earlier methods using amine-based precursors resulted in larger, non-quantum-confined particles resembling bulk materials [182, 183]. Subsequently, a general route employing alkylphosphine precursors was developed. For instance, Malik et al. [61] synthesized CuInSe QDs with a diameter of 4.5 nm using trioctylphosphine (TOP)-dissolved selenium, though this approach required prolonged reaction times. Similarly, Maynard et al. [184] utilized dodecanethiol (DDT)-capped CuInSe QDs with selenium powder dissolved in tributylphosphine (TBP).

Despite these advancements, most reported methods uses expensive phosphine and involves multiple steps, including post-treatment processes and separate purification steps for core/shell QDs [185, 186]. In contrast, the proposed method simplifies the process, saves time and resources by adopting a single-pot synthesis approach to produce both core/shell and core/alloyed shell QDs. This method eliminates the need for phosphine-based precursors and instead uses a high-boiling-point amine/thiol binary solvent system to dissolve selenium at high temperatures. Unlike earlier studies [186, 187], this combination offers good chemical stability and reactivity, enabling efficient synthesis of selenide QDs without the limitations of low boiling points or inadequate solvent power. The adopted methodology provides a phosphine-free alternative and one-pot synthesis route that overcomes the challenges associated with existing methods, demonstrating significant advancement in the synthesis of ternary Cu-based nanocrystals.

Reason for Choice of parameters: The shell thickness was carefully selected to achieve complete surface passivation with a gradient alloyed shell. This design improves charge extraction and enhances PL lifetime and PLQY. The chosen thickness in accordance with literature values shown to be optimal for gradient shell layers, ensuring both stability and high performance [179, 188].

For doping levels, a Cu doping concentration of 5% was employed, as it demonstrated superior performance with high PL lifetime in prior studies [178]. The percentage of doping was found to effectively modify the electronic structure without significantly impacting the crystallinity or stability of the QDs. To further enhance PL lifetime, an equivalent doping level of Mn (5%) was introduced [189]. This dual-doping strategy enhances the complementary effects of Cu and Mn. The resulting QDs to have prolonged PL lifetimes and improved performance. These parameters were chosen to strike a balance between performance, stability, and reproducibility for making the synthesized QDs suitable for targeted applications.

The hot-injection technique produces QDs in high-quality with precise control on size, shape, composition. The control of parameters is important for achieving good optical and electronic properties [75]. The specific reason is that different reaction conditions can be tuned such as temperature, reaction time, and precursor concentration to modify properties for specific applications. While continuous flow synthesis and SILAR are alternative methods with their own advantages, as described earlier in Section 1.2, continuous flow synthesis allows for precise control of reaction parameters and sequential analysis with inherent scalability. However, it is less suitable for lab-scale synthesis and involves significant upfront investment in specialized equipment. In contrast, hot injection is ideal for laboratory-scale synthesis, where high quality and reproducibility are prioritized over scalability.

2.2.3 Fabrication of the photoanode

Cleaning FTO glass substrate:

A conducting substrate is typically used to transport the photogenerated charge carrier from a thin film to an external circuit. Fluorine-doped tin oxide conductive glass substrate (FTO) is widely used in PEC applications due to its excellent electrical conductivity (~15 Ω.cm), high thermal stability (~650 °C), and optical transparency (~85%). Cleaning FTO is one of the crucial steps before preparing a thin film. FTO glass substrates are often coated with polymers to protect them from contamination and scratches. So, it should be completely removed before preparing thin films. Therefore, the FTO glass substrate was cleaned by the following steps:

a. Marking: To differentiate the conductive side of the FTO glass substrate from the non-conductive side, a diamond pen is used.
b. Initial Cleaning: The FTO substrate is cleaned with soap and water.
c. Acetone Cleaning: The FTO substrate is placed in a cleaning basket and immersed in acetone. It is then cleaned by ultrasonication in acetone for 20 min.
d. DI Water Cleaning: The FTO substrate is washed using DI water and sonicated in DI water for 10 min. This procedure is followed by drying under N_2 flow.
e. UV/Ozone Treatment: The FTO substrate is further treated in UV/ozone for 20 min to remove surface organic contaminants.

Preparation of thin film:

(i) TiO_2

Two types of TiO_2 paste were used to produce different layers of TiO_2 film i.e. transparent and scattering layers. The transparent TiO_2 (18NR-T) contains an average particle size of 20 nm with 99.9% crystalline anatase structure, whereas the scattering TiO_2 (18NR-AO) contains particles up to 450 nm in diameter. The transparent TiO_2 improve the light transparency, and the scattering TiO_2 enhances the light scattering efficiency by increasing the path length of incident light. These titania pastes were deposited onto the cleaned substrate by tape-casting method, also popularly known as the doctor blade approach (Figure 2.2). First, two layers of TiO_2 18NR-T paste were coated on the FTO surface and dried at room temperature for 15 min. Then, placed on a hot plate and dried at 120 °C for 6 min. A second layer of 18NR-AO TiO_2 was coated to obtain a thick film using the same method. The films were annealed at 500 °C for 1 h to yield mesoporous TiO_2 films. The annealing process increases the crystallite size and contact between particles and removes the organic residues in the film.

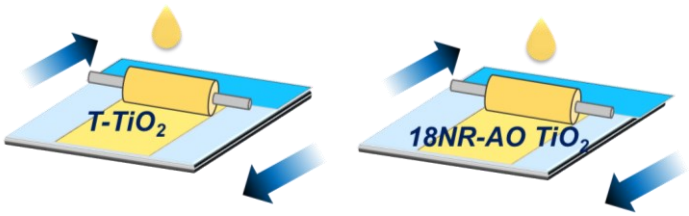

Figure 2.2 Graphical representation of fabricating different TiO_2 layers using doctor blade approach.

(ii) TiO_2-MWCNTs nanohybrid

The MWCNTs was integrated with TiO_2 to improve the electron transport property of the photoanode. A MWCNTs suspension was prepared by adding 10 mg MWCNTs in 15 mL ethanol. The ethanolic solution containing MWCNTs sonicated for 1 h to form a suspension. The sonicated MWCNTs (16.05 mg/0.015 wt%) was added to TiO_2 transparent paste. The procedure used to prepare TiO_2 film was followed to obtain the TiO_2-MWCNTs nanohybrid.

(iii) ZrO_2

ZrO_2 thin films are used as a benchmark with respect to TiO_2 due to their improper band alignment with QDs for water splitting. The methodology to prepare ZrO_2 thin films was adopted from the literature [190]. In detail, 1g of ZrO_2 powder, 1.0 mL alpha-terpineol, 0.5 g Ethyl cellulose, 1.0 mL DI water, 5.0 mL ethanol were stirred to form a homogenous solution. In addition, the solution was kept under vacuum to remove the solvent. The decrease in total volume produces a thick ZrO_2 paste. The ZrO_2 paste was coated on FTO by the doctor blade

approach. After drying at RT for 10 min, the ZrO_2/FTO was annealed at 500 °C for 30 min in ambient conditions.

Sensitization of QDs on TiO_2 films: The purified QDs were deposited on TiO_2 films using the electrophoretic deposition (EPD) technique (Figure 2.3). The principle of this technique involves the migration of charged QDs in a stable suspension towards the oppositely charged electrode by applying an external electric field. The driving force aids in the homogenous deposition of QDs on the mesoporous TiO_2 thin film. In a typical process, two pieces of FTO/TiO_2 thin films were immersed vertically into QDs/toluene solution. A voltage difference up to 200 V was applied between two electrodes fixed at 0.5 cm. The deposition was carried out for 2 h. The electrodes are washed several times with toluene after the deposition process for removing the unbounded QDs and dried under N_2 gas.

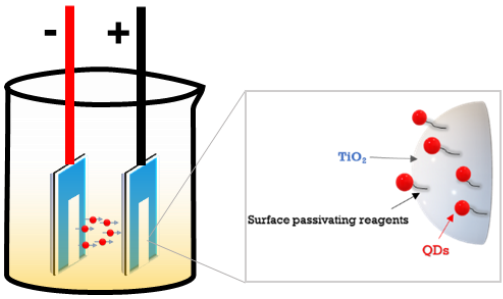

Figure 2.3 Electrophoretic deposition of QDs

ZnS SILAR and SiO_2 coating: ZnS is chemically stable and corrosion resistant, which have proven to protect QDs from degradation and dissolution upon direct contact with electrolyte [191]. For this reason, three layers of inorganic semiconductor ZnS layer were coated on QDs/TiO_2 photoanode using successive ionic layer adsorption and reaction (SILAR) technique. To deposit ZnS, the photoanode was immersed alternatively into 0.1 M $Zn(OAc)_2.2H_2O$ and 0.1 M $Na_2S.9H_2O$. Then, each time washed with methanol solution and DI water/methanol solution corresponding to the Zn and S solutions, followed by drying using N_2 flow. Immediately, the ZnS-coated photoanode was placed inside an ethanolic solution (10 mL) of tetraethyl orthosilicate (TEOS) (20 μL) and kept for 2 h at 35 °C to coat SiO_2. After this process, the photoanode was washed with ethanol and purged with N_2. The PEC device fabrication was completed by covering the surface of photoanodes with epoxy resin, leaving a rectangular area as an active region.

2.2.4 Photoelectrochemical measurements

The photoelectrochemical (PEC) measurements were performed using a three-electrode setup, which included a working electrode, a platinum (Pt) sheet as the counter electrode, and an Ag/AgCl electrode saturated with KCl serving as the reference electrode. This configuration was used to assess the PEC performance of the QDs-sensitized photoanode. The electrodes were immersed inside the electrolyte solution (Na_2S/Na_2SO_3 – 0.25 M/0.35 M), which serves as a hole scavenger. Prior to PEC measurement, the electrolyte solution was purged with N_2 for 30 min to remove the dissolved oxygen.

The three-electrode system is the most used configuration to perform PEC measurements. The advantage is that it provides insights on into the efficiency of photoelectrode rather than the full device. Nevertheless, the overall cell efficiency (STH) cannot be measured using this type of system. An electrochemical workstation (CHI-760D) was employed to conduct the linear sweep voltammetry (LSV), Chronoamperometry, open circuit voltage (OCP), and electrochemical impedance spectroscopy (EIS) measurements. The potential measured (vs Ag/AgCl) is transformed to a standard reversible hydrogen electrode (RHE) using the formula provided below (Equation 2):

Equation 2 Nernest equation to convert the potential measured (vs Ag/AgCl) to standard reversible hydrogen electrode (RHE).

$$V_{RHE} = V_{Ag/AgCl} + 0.1976 + pH \times 0.059 \quad (2)$$

A Class AAA sun simulator (model SLB-300A by Sciencetech Inc.) with a 300 W xenon arc lamp as a light source was used, and the light was filtered using an AM 1.5G filter. The intensity of light from the sun simulator to the sample is adjusted to 100 mW/cm^2 using a silicon reference cell.

2.2.4.1 Open circuit potential (OCP):

Open circuit potential is measured to investigate the photovoltage, electron lifetime and onset potential of the designed photoanode. Typically, the light illumination on the photoanode generates an electron/hole pair under open circuit conditions. Under illumination, photogenerated electrons accumulate in the bulk of the material, while the holes are neutralized by the hole-scavenger present in the electrolyte. This separation of charge creates an internal electric field, shifting the field-free potential toward a more cathodic direction. The onset potential is the point where a stable open-circuit potential (OCP) is achieved under light exposure. When the light source is turned off, the electrons recombine with oxidized species in

the electrolyte, causing the potential to gradually decrease. The photovoltage represents the voltage generated by a PEC device, which is the difference between the potentials measured in the dark and under illumination. Figure 2.4 depicts the typical open-circuit potential curve. Moreover, the recombination rate and electron lifetime are determined from the potential decay using the following equation (Equation 3):

Equation 3 Formula used to calculate the Electron lifetime.

$$\tau = \left(\frac{K_B T}{e}\right) * \left(\frac{dV_{oc}}{dt}\right)^{-1} \quad (3)$$

Where T is temperature, K_B is Boltzmann's constant, e is the charge of the electron, τ is the potential dependant electron lifetime, and V_{oc} is the open circuit potential values.

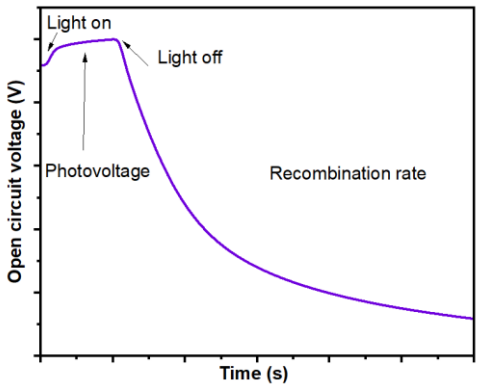

Figure 2.4 OCP curve

2.2.4.2 Linear sweep voltammetry (LSV):

Linear sweep voltammetry is to investigate the properties of the fabricated QDs sensitized photoanode, and to measure the photocurrent density against the applied potential. The onset potential value and maximum photocurrent density that a photoanode can generate are directly measured. Initially, the photoanode is slightly forward biased and then reverse biased (more negative potential with respect to reference) to increase the electric field strength on the space charge region. This improved electric field strength promotes charge separation, and transportation to enhance the photocurrent. The potential window of the photoanode was first identified to set the scanning range. The experiments are carried out in dark, light and chopped conditions as depicted in Figure 2.5.

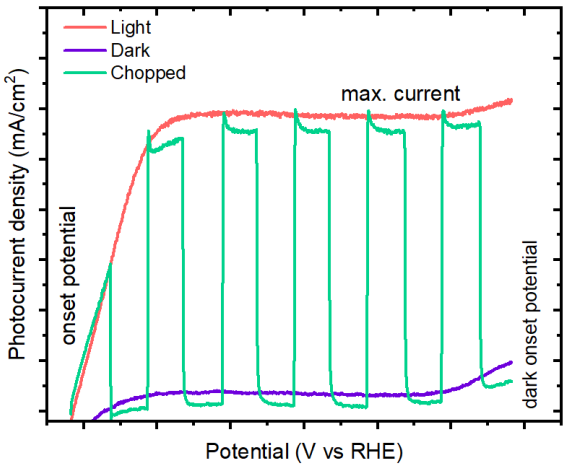

Figure 2.5 LSV curve

2.2.4.3 Chronoamperometry:

Chronoamperometry is used to measure the durability of the photoelectrode. This measures the photocurrent over time at a constant applied potential. Usually, the constant potential value is taken from the obtained maximum photocurrent density value to measure the long-term photocurrent with respect to time. The long-term stability measurements were conducted for a period of 3600 s.

2.2.4.4 Electrochemical impedance spectroscopy:

Electrochemical impedance spectroscopy (EIS) is an effective tool for understanding carrier dynamics because of its sensitivity to processes occurring at interfaces. The electron recombination at different interfaces, such as photoanode/electrolyte and inside photoanode, can be extracted from the response by applying frequency over a broad range. The experiment was conducted by applying an AC voltage in the frequency range of 300 KHz to 10 mHz. The corresponding response from the photoanode is recorded. EIS measurements are performed under dark conditions. The Nyquist plot represents the data obtained from the applied AC signal that displays the imaginary part of impedance against the real part of the impedance. In the Nyquist plot, the semi-circle arc corresponds to the charge transfer resistance. It indicates the electron transport process at the photoanode interfaces.

2.2.5 Fabrication of the luminescent inks and anti-counterfeiting labels

400 mg of PMMA was added into 2 mL of toluene, and stirred overnight under dark at RT. The obtained homogenous polymer solution was added to 2 mL of purified QDs, followed by sonication for 1 h, and stirred for 10 min. The prepared luminescent inks are depicted in Figure 2.6. Invisible security labels were created by drawing patterns using luminescent ink onto different types of packaging materials. The patterns were dried at RT for 10 min to obtain the security labels. UV light of 365 nm was used as an excitation light source.

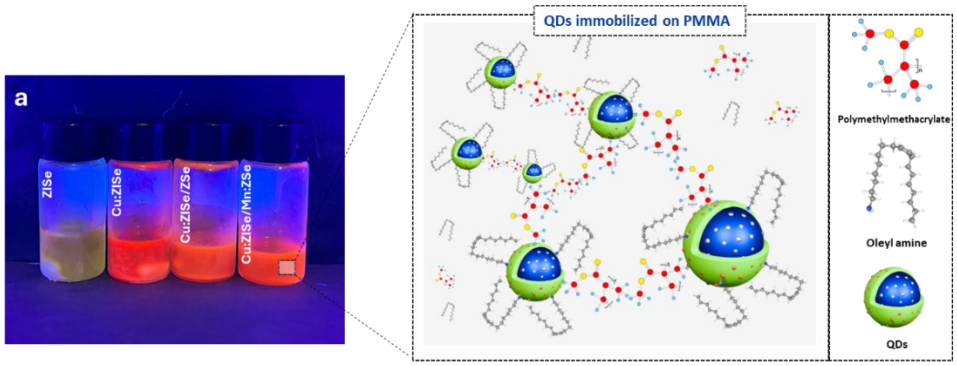

Figure 2.6 Photograph of vials containing prepared luminescent inks under UV light exposure.

2.2.6 Stability evaluation of anti-counterfeiting labels.

To understand the reliability of the fabricated anti-counterfeiting labels for real-time application, the printed patterns were tested by long-term water exposure and direct-thermal exposure. The thermal stability of the printed patterns was evaluated in the temperature range between 20 °C to 170 °C. The printed patterns soaked directly in water and the luminescence was monitored for over 10 weeks. A photograph of the printed patterns was taken under UV light for both the thermal and water exposure studies.

2.3 Characterization techniques

To examine and understand the physiochemical properties of the designed QDs and their devices, various characterization techniques were used, and the crystalline nature, size, morphology, elemental composition, optical properties, and electrochemical behaviour were studied to optimize the design and justify the selection of materials and synthesis methods. The characterization techniques adopted to validate the main objectives of each project are provided in the following:

2.3.1 X-ray diffraction

XRD is to investigate the crystal structure and the phase transformation in the synthesised QDs. The principle of XRD is based on diffraction of incident X-rays (0.1 – 10 Å) by the atomic planes in a crystal structure (Figure 2.7). The X-ay scattering is governed by bragg's law as given below (Equation 4):

Equation 4 Bragg's Equation

$$n\lambda = 2dsin\theta \quad (4)$$

Where d refers to the distance between the two atomic planes, λ refers to the x-ray wavelength, and θ refers to the incident angle.

X-ray diffractions (XRD) analysis was carried out in the Philips Xpert diffractometer using a Cu Kα radiation source (λ = 0.154 nm).

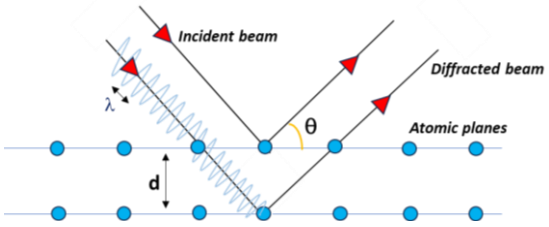

Figure 2.7 Electron diffraction according to Braggs law.

2.3.2 Transmission electron microscopy

TEM is used to study the morphology of the QDs. The TEM images are acquired by passing the high-energy electron beam generated by an electron gun. When the tungsten filament is subjected to high electric field or heated, the electrons are emitted and accelerated at high energy (60 keV to 300 keV). A series of electromagnetic lenses connected converges the beam into the sample area. The electrons transmitted without deflection inside the sample are focused by objective lens to form an image (Figure 2.8). TEM images of QDs were produced using a JEOL 2100F TEM system.

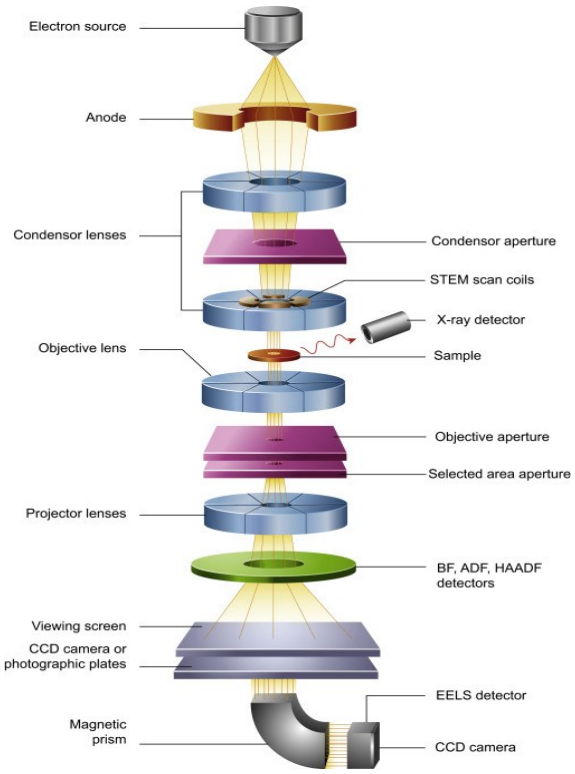

Figure 2.8 TEM instrumentation ***[192]***

2.3.3 Scanning electron microscopy

To study the surface morphology and composition of the samples, Scanning electron microscopy (SEM) is used. SEM images of the photoanodes were acquired using the JEOL JSM-6900F. TEM and SEM works on similar principle. The TEM transmits electron through sample whereas SEM scans a focused electron beams across the surface to acquire image. Two different signals are produced when the electron beam interacts with sample as follows:

Secondary electrons (SE): the inelastic scattering from the atoms ejects low-energy electrons, providing high-resolution surface topographic images.

Backscattered electrons (BSE): the elastic scattering from atoms generates high-energy electrons, providing a compositional contrast (Figure 2.9).

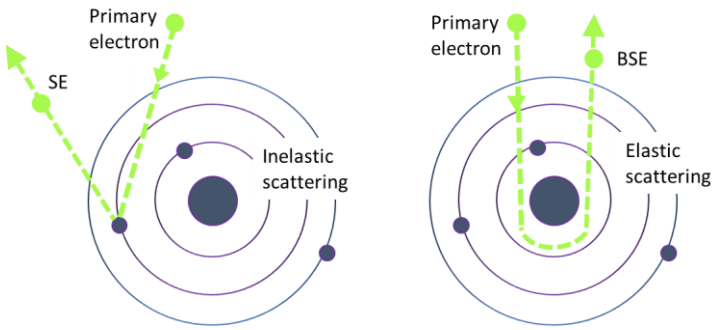

Figure 2.9 Elastic and Inelastic scattering on irradiation with X-ray source.

2.3.4 Energy dispersive X-ray spectroscopy

EDS is in conjunction with SEM which is used to analyze the elemental composition. When a focused high-energy beam of electrons is directed in the sample, inner-shell electrons are displaced from orbitals. The electron in the outer orbital fills the vacancy of the displaced electron by emitting X-ray (Figure 2.10). The energy of emitted X-rays corresponds to specific element. Based on emitted X-rays, the chemical composition and elemental mapping of photoanodes was evaluated.

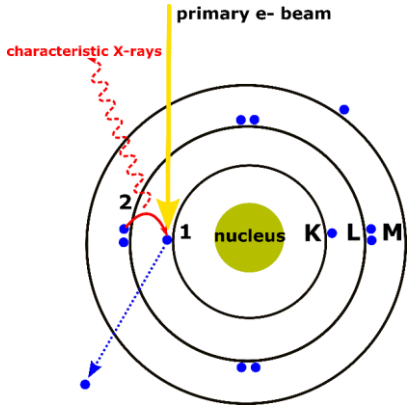

Figure 2.10 Working principle of EDS [193]

2.3.5 X-ray photoelectron spectroscopy

XPS is a surface-sensitive spectroscopic technique that is used to analyze the surface chemical state and chemical composition of material. To obtain a XPS spectra, a beam of X-rays is irradiated on the sample and the kinetic energies of the ejected electrons are analyzed. The photoelectric equation provided below is used to determine the binding energy of each electron (Equation 5):

Equation 5 Photoelectric equation

$$E_b = E_p - (E_k + \varphi) \quad (5)$$

Where E_p is energy of x-ray photons, E_k is the kinetic energy of photoelectron, and ϕ is work function which is the difference of vacuum level and fermi level. VG Escalab 220i-XL was used to perform XPS and a twin anode X-ray source is applied on the hemispherical analyzer.

2.3.6 UV-vis-NIR absorption spectroscopy

UV-vis-NIR absorption spectroscopy is used to determine the absorbance of light in a solution or solid. The principle behind UV-vis-NIR absorption spectroscopy is Beer-lambert law (Equation 6).

Equation 6 Beer-Lambert equation

$$A = \varepsilon . l . C \quad (6)$$

Where C refers to concentration of absorbing species, ε is the molar absorptivity, and l refers to the path length (differs based on cuvette). Beer-Lambert law states that absorption of light by a sample is proportional to tits concentration. The absorbance of the sample can be calculated using the formula (Equation 7):

Equation 7 Formula to calculate the Absorbance of the sample.

$$A = -\log\left(\frac{I}{I_0}\right) \quad (7)$$

The UV-vis-NIR absorption spectra was measured using Varian Cary 5000 in the range from 380 - 700 nm.

2.3.7 Fluorescence spectroscopy

Fluorescence spectroscopy is used to analyze the fluorescence from the sample. When light is directed onto a sample, the electrons move into excited states and relaxes to ground state by emitting a low-energy photons. The light emission is also called PL, which is measured based on intensity or frequency using fluorescence spectrophotometer. The PL emission spectra of QDs were obtained using Fluorolog-3 system instruments.

2.3.8 Time-resolved photoluminescence spectroscopy

The time-resolved photoluminescence spectroscopy (TRPL) is used to measure the lifetime decay of photogenerated electrons in QDs and QDs based photoanode. In addition, the charge transfer rate can be calculated based on average PL lifetime value. The transient PL decay curves of the QDs dispersed in toluene was measured at an excitation wavelength of 500 nm. The PL lifetime is characterized by three major processes, as follows: (i) short lifetime of non-

radiative decay process (τ_1), (ii) medium lifetime of radiative decay process due to recombination of photogenerated carriers (τ_2), and (iii) long lifetime related to the energy transfer process (τ_3). Each component that contributes to the multiexponential decay is linked to a distinct PL decay channel, and the representation of each channel is reflected by its respective relative amplitude. The PL decay curves were fitted using a triexponential function. The average PL lifetime "$\tau_{average}$" of the prepared QDs was calculated using the following equation (Equation 8):

Equation 8 Formula to calculate Average PL lifetime

$$\tau_{average} = \frac{A_1{\tau_1}^2 + A_2{\tau_2}^2 + A_3{\tau_3}^2}{A_1\tau_1 + A_1\tau_1 + A_1\tau_1} \quad (8)$$

where A_x (x = 1, 2, 3) are the weighted coefficients from the components, while the τ_x (x = 1, 2, 3) refers to the characteristic lifetimes. Based on the calculated average carrier lifetime values of photoanode, the charge transfer rates was determined by using the following equation (Equation 9):

Equation 9 Average carrier lifetime formula

$$K_{et\ or\ ht} = \left[\frac{1}{QDs\ (\tau_{avg})/e^{-}or\ h^{+}scavenger} - \frac{1}{ZrO_2\ (\tau_{avg})}\right] \quad (9)$$

The PL lifetime of the QDs was measured in the time-correlated single-photon counting (TCSPC) mode with a laser filter of 550 nm (laser λ: 401.6 nm; pulse width: 77.4 ps) using Edinburg instruments EPL405.

CHAPTER 3: Dynamic Ternary Surface-engineered Colloidal Cu-based QDs towards Enhanced and Stable Photoelectrochemical H_2 Production

3.1 Project plan

Ternary I-III-VI_2 quantum dots (QDs) have recently received wide attention in solar energy conversion technologies because of their non-toxicity, tunable band gap, and composition-dependant optoelectronic properties [56, 60]. Nevertheless, ternary QDs often exhibit abundant surface defects and trap states due to their complex crystal structure, which can cause severe non-radiative recombination, resulting in poor photo/chemical stability. The design of inorganic wide band gap semiconductors (such as ZnS and ZnSe) used as passivation layers for QDs has proven effective in addressing issues related to limited operational stability, including unfavourable non-radiative recombination and insufficient separation and transfer of photogenerated charge carriers.

In this project, we aim to develop ternary colloidal $CZISe_2$/ZSeS core/alloyed shell QDs as efficient light harvesters for PEC H_2 production. To ensure uniform shell growth, we utilized an in-situ growth passivation approach via a single-step hot injection method. We investigated the optical properties and charge carrier dynamic behaviour to understand the carrier recombination after shell passivation. The effect of the shell on PEC performance and long-term operational stability was studied under illumination. Integrating multi-walled carbon nanotubes (MWCNTs) on QD-based devices is expected to improve conductivity and enhance PEC performance.

3.2 Structural and morphological features

Environment-friendly ZnSeS shell engineered Cu:$ZnInSe_2$ QDs ($CZISe_2$/ZSeS core/shell QDs) were synthesized via a hot-injection technique (Figure 3.1a). The $CZISe_2$ core QDs was prepared by heating a mixture of $Zn(OAc)_2$, $In(OAc)_3$, Selenium powder, 1-octadecene, oleyl amine, and 1-dodecanethiol at 200 °C for 25 min. Following the synthesis of core QDs, without purification, the shell precursors $Zn(OAc)_2$, TOP-Se and TOP-S were sequentially introduced into the same solution at 200 °C and heated to 235 °C for 30 min. A uniform composition gradient shell can be obtained in a radial direction because of the faster reactivity of TOP-Se than TOP-S [179]. The difference in reactivity leads to the preferential formation of a ZnSe shell near the $CZISe_2$ core, followed by the growth of ZnS that facilitates the creation of ZSeS shell. The as-synthesized $CZISe_2$ exhibit three distinct characteristics peaks in X-ray diffraction (XRD)

spectra located at 26.49°, 45.36°, and 52.69°, which corresponds to tetragonal $ZnInSe_2$ crystal structure (Figure 3.1b) [54, 194]. Upon growth of a ZSeS shell, the diffraction peaks shift to higher angles towards zinc-blende ZnS and no distinct peaks related to ZnS or ZnSe were found [195]. The shift towards a higher angle indicates the decrease in the lattice parameter of the $CZISe_2$ core with the growth of the ZSeS shell in accordance with Bragg's [196]. Therefore, the observations provide strong evidence for the successful formation of core/shell nanocrystals. The $CZISe_2$ QDs exhibit tetrahedral shape with a diameter of 3.53±0.85 nm (Figure 3.1c). The inset high-resolution transmission electron microscopy (TEM) image of $CZISe_2$ QDs shows a lattice spacing of 0.34 nm corresponding to the (112) hkl planes. The average crystalline size does not show an apparent contrast (3.40±1.09 nm) due to the ultrasmall size as observed in the TEM, suggesting the shrinkage of core QDs after ZSeS shell growth and the corresponding decrease in lattice spacing to 0.33 nm, which is consistent with the shift in XRD peaks (Figure 3.1d).

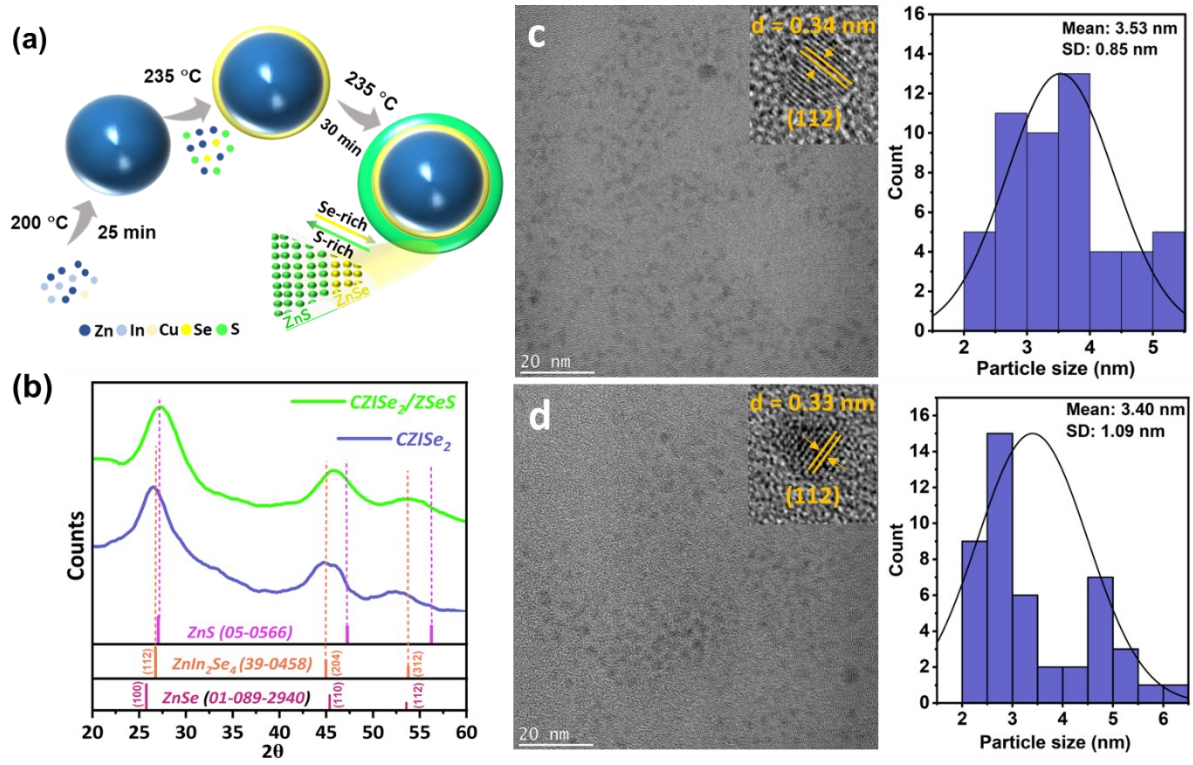

Figure 3.1 (a) Schematic illustration of synthesis of $CZISe_2$ and $CZISe_2$/ZSeS QDs. (b) XRD patterns of $CZISe_2$ and $CZISe_2$/ZSeS QDs, and JCPDS line patterns of ZnS, $ZnInSe_2$, ZnSe. (c) Representative TEM image of $CZISe_2$ QDs and the relevant size distribution histograms. (d) Representative TEM image of $CZISe_2$/ZSeS QDs and the relevant size distribution histograms. The inset HR-TEM image shows the lattice fringes.

X-ray photoelectron spectroscopic (XPS) studies were conducted to investigate the chemical states and surface elemental composition for the $CZISe_2$ core and $CZISe_2$/ZSeS core/shell QDs.

The wide-scan XPS survey spectrum in Figure 3.2a reveals the peaks originating from the elements Zn, Cu, In, S and Se are ascribed to the $CZISe_2$ and $CZISe_2$/ZSeS core/shell QDs, and the additional peaks point out the presence of O, Si, C. The narrow-scan HR-XPS of individual elements were recorded (Figure 3.2b-f). O 2p and Si 2p peaks correspond to the glass substrate on which the QDs were deposited. C 1s peaks correspond to the surface organic ligands, including the tri octyl phosphine ($P(C_8H_{17})_3$ and oleyl amine ($C_{18}H_{35}NH_2$) (Figure 3.3). The Zn 2p core level has been split into Zn $2p_{3/2}$ (1020.9) and Zn $2p_{1/2}$ (1043.88) with spin-orbital splitting energy of ~22.9 eV, which corresponds to Zn^{2+} (Figure 3.2b) [197]. The Cu 2p peaks split into $2p_{1/2}$ and $2p_{3/2}$ peaks, as depicted in Figure 3.2c, indicating the successful doping of Cu into the $ZnInSe_2$ crystal structure. While Cu^{2+} was used as Cu precursor source, the observed Cu^{+} state could be ascribed to the complete reduction of Cu^{2+} into Cu^{+} at high temperatures (Figure 3.2c) [198]. Their spin-orbit splitting (20.5) is also consistent with the standard Cu^{+} monovalent copper ion [199]. As shown in Figure 3.2d, the two peaks at 451.6 and 444.1 eV correspond to In $3d_{3/2}$ and In $3d_{5/2}$, respectively, assigned to valence state of +3 [200]. The characteristic peaks of Se 3d located at 53.62 and 54.88 eV indicate the existence of Se^{2-} of Zn-Se (Figure 3.2e). The peak at 59.24 eV corresponds to SeO_2, which is evident in the Se 3d fitting spectra, suggesting the surface oxidation of selenium. For ZSeS passivated core QDs, the intensity of Se-O has completely diminished due to the elimination of surface oxidation, indicating the effective passivation of surface defects/trap states. The two deconvoluted S 2p peaks at 160.58 and 162.65 eV can be attributed to the S^{2-} in Zn-S (Figure 3.2f). Compared with the binding energy (B.E) of chemical states in $CZISe_2$, the peaks of Zn 2p, Se 3d, In 3d shifted towards lower B.E whereas Cu 2p shift to higher B.E in $CZISe_2$/ZSeS core/shell QDs. The observed shift in B.E reflects the changes in the chemical coordination environment as a consequence of the formation of core/shell structure, which is in accordance with the XRD results.

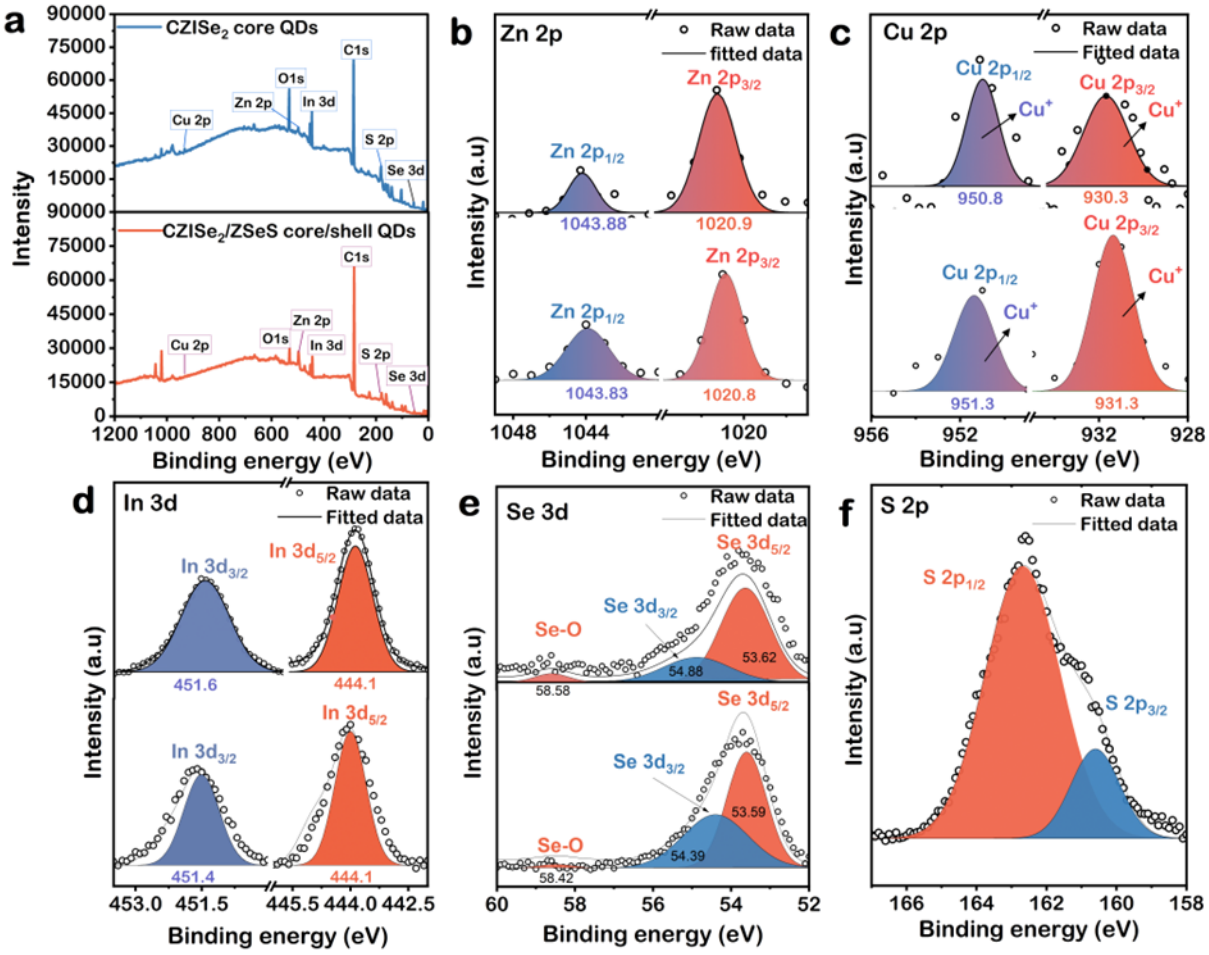

Figure 3.2 (a) Wide-scan XPS Survey spectrum. HR-XPS spectra of (b) Zn 2p, (c) Cu 2p, (d) In 3d, and (e) Se 3d core levels for $CZISe_2$ QDs and $CZISe_2$/ZSeS QDs. HR-XPS spectra of (f) S 2p core levels for $CZISe_2$/ZSeS QDs.

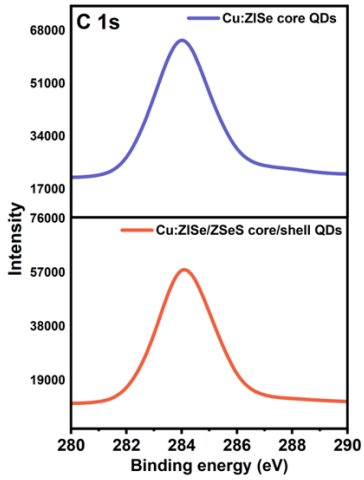

Figure 3.3 Narrow scan XPS spectra of C1s for $CZISe_2$ core QDs and $CZISe_2$/ZSeS core/shell QDs.

3.3 Optical properties

The optical properties of QDs were studied by investigating the UV-vis absorption and PL spectra. UV-visible absorption spectra (absorption values normalised at 420 nm for all the spectra) of as-synthesized $CZISe_2$ QDs and $CZISe_2$/ZSeS core/shell QDs are depicted in Figure 3.4a. Generally, the excitonic absorption and emission features are poorly resolved for ternary and quaternary alloyed QDs owing to their intra-gap states and the irregular elemental distribution [201, 202]. The $CZISe_2$ QDs exhibit an absorption edge around 600 nm and simultaneously, have a broad PL emission peak at 615 nm. The PL emission originates from the electron recombination from CB of host semiconductor with holes in the Cu^+ states [203]. After growth of ZSeS on $CZISe_2$ QDs, the absorption edge of synthesized $CZISe_2$/ZSeS core/shell QDs shifted to shorter wavelength around 590 nm. The same phenomenon is observed in the PL spectra (Figure 3.4b), where the PL peaks blue-shifts from 615 nm to 605 nm after overgrowth of ZSeS shell. As shown in Figure 3.4c, the optical band gaps of $CZISe_2$ QDs observed to increase by coating ZSeS shell. According to previous reports, the sublattice sites of anions and original shapes remain intact while the cations of similar ionic radii undergo substitutions during the reaction. Based on this, we could attribute the enlarged band gap and blue-shift is due to the exchange of Cu^+ and In^{3+} with excess Zn^{2+} near the surface at high temperatures that leads to the reduced size of $CZISe_2$ core QDs [204]. In addition, a much higher PL intensity of $CZISe_2$/ZSeS core/shell QDs explains the suppression of surface traps/defects that causes non-radiative decay (Figure 3.5). The transient PL (TRPL) spectroscopy was applied to investigate the lifetime of photoinduced charge carriers, a crucial performance indicator in PEC devices. The PL lifetime decay curve of QDs dispersed in toluene are shown in Figure 3.4d. The $CZISe_2$/ZSeS QDs presents an average PL time of ≈153.97 ns, which is much longer than the bare $CZISe_2$ QDs. The prolonged lifetime with shell coating would be mainly attributed to the reduced e^-/h^+ overlap caused by the gradient energy structure and the strong electron leakage from core into the shell [157, 205]. The alloyed ZSeS shell can facilitate a stepwise band alignment, effectively lowering the energy barrier for charge transfer, which is beneficial for solar energy conversion.

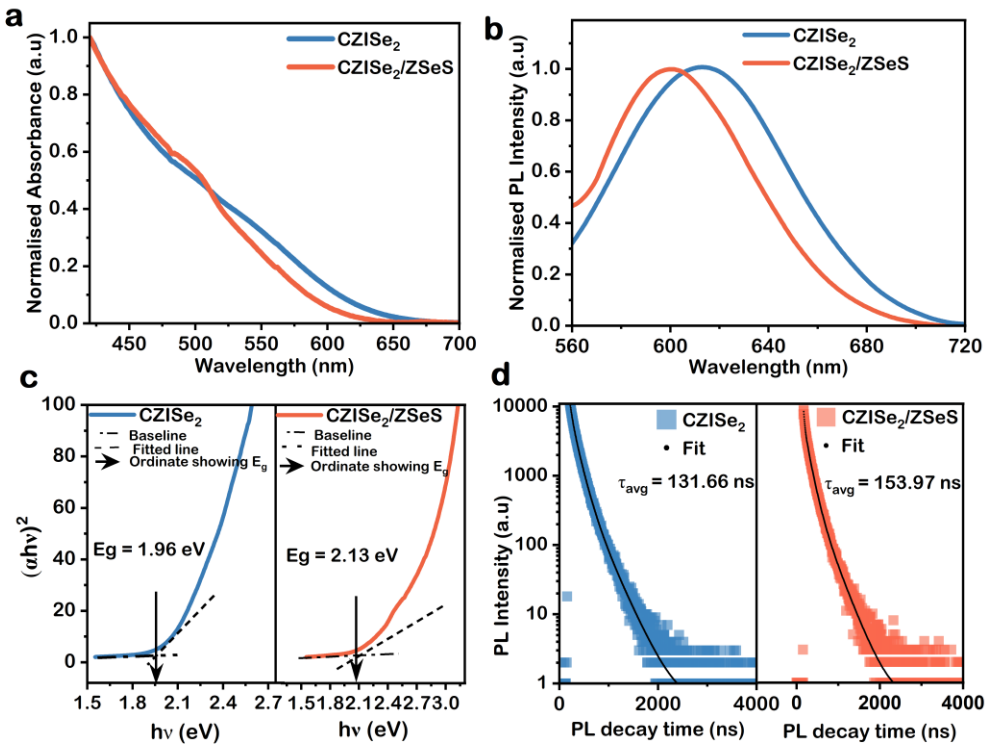

Figure 3.4 (a) Normalized absorption spectra of $CZISe_2$ and $CZISe_2$/ZSeS QDs. (b) Normalised PL spectra of $CZISe_2$ and $CZISe_2$/ZSeS QDs. Tauc plots of (c) $CZISe_2$ and $CZISe_2$/ZSeS QDs. (d) Transient PL decay spectra of $CZISe_2$ and $CZISe_2$/ZSeS QDs in toluene.

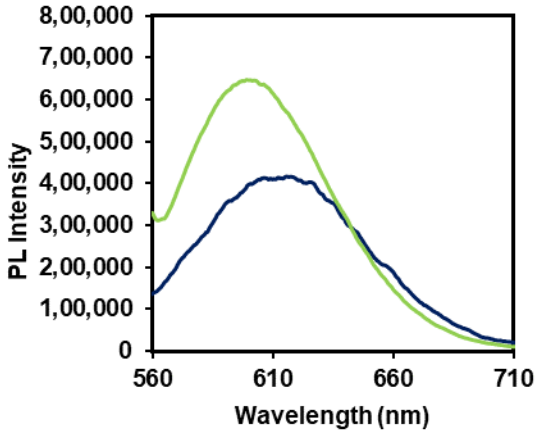

Figure 3.5 PL spectra of $CZISe_2$ (blue line) and $CZISe_2$/ZSeS core/shell QDs (green line).

3.4 Carrier dynamics

PL lifetime decay measurements were conducted to investigate the dissociation of photogenerated charge carriers (e^-/h^+ pairs) in QDs which is in interface with different carrier scavengers. The core and core/shell QDs were sensitized on different components, including

TiO_2, TiO_2-MWCNTs and ZrO_2 thin films, and the lifetime was measured with and without electrolyte. The electrolyte composed of 0.25 M Na_2S/0.35 M Na_2SO_3 (pH≈13) serves as a hole scavenger. TiO_2 accepts the e- from QDs due to the lower conduction band minimum (CBM) than the CBM of QDs. The ZrO_2 with a wider band gap (~5 eV) and a more negative CBM do not have suitable band alignment for electron transfer from QDs and thus, ZrO_2 was used as benchmark for the carrier dynamic study. Also, we rule out the energy transfer possibility between QDs and TiO_2 because of the no overlap between their absorption spectra. Thus, we strongly confirm that the reduced PL lifetime can be attributed to the e^-/h^+ from QDs to scavengers. The average PL decay time of TiO_2-QDs is much shorter than ZrO_2-QDs, confirming that the electron transfer is efficient from QDs to TiO_2 (Figure 3.6a & e and Scheme I). The improper electronic band alignment between ZrO_2 and QDs results in slow charge transfer kinetics. Similarly, the PL lifetime of ZrO_2-QDs/electrolyte is much lower than ZrO_2-QDs, indicating the faster hole transfer kinetics in presence of electrolyte (Figure 3.6d & 6f, Scheme III). The calculated average PL lifetime and the corresponding fitting parameters is provided in the Table 3.1.

Table 3.1 Transient PL decay fitted parameters and the calculated average PL lifetime for all the fabricated photoanodes.

Sample	a_1	a_2	a_3	τ_1 (ns)	τ_2 (ns)	τ_3 (ns)	$\tau_{average}$
TiO_2/CZISe$_2$	4910.81	1929.32	178.74	15.19	76.1	287.82	99.36
TiO_2/MWCNTs/CZISe$_2$	4920.61	1963.31	190.54	14.2	69.39	255.02	89.66
ZrO_2/CZISe$_2$	4882.71	2924.6	253.11	28.34	123.28	411.82	151.36
ZrO_2/CZISe$_2$/EL	4553.83	3570.49	307.27	26.18	107.55	354.87	135.75
TiO_2/CZISe$_2$/ZSeS	4723.62	1148.5	62.18	6.9	27.3	122.89	28.21
TiO_2/MWCNTs/CZISe$_2$/ ZSeS	4874.61	711.39	18.68	8.51	39.87	146.34	25.94
ZrO_2/CZISe$_2$/ZSeS	478.66	5365.97	2939.32	9.17	36.24	119.49	58.63
ZrO_2/CZISe$_2$/ZSeS/EL	5820.94	1822.5	115.5	8.73	35.87	113.34	39.51

Based on the calculated average carrier lifetime values, we determined the charge transfer rates by using the following equation (Equation 10):

Equation 10 Charge transfer rate calculation

$$K_{et\ or\ ht} = \left[\frac{1}{QDs\,(\tau_{avg})/e^{-}or\ h^{+}scavenger} - \frac{1}{ZrO_2\,(\tau_{avg})}\right] \quad (10)$$

Compared with $CZISe_2$ QDs, the $CZISe_2$/ZSeS core/shell QDs (1.8×10^7 s^{-1}) show higher electron and hole transfer rate to TiO_2 and the electrolyte, respectively (Table 3.2). First, the stepwise band alignment of the ZSeS shell improves the charge injection rate to TiO_2 and increases the possibility of hole recombination with the electrolyte. Secondly, the passivation of surface traps/defects has mitigated charge recombination sites present in $CZISe_2$ QDs. To further improve the electron transport properties, the MWCNTs were integrated with TiO_2 by addition of appropriate amount of MWCNTs to TiO_2 using doctor blade technique [153]. A substantial improvement in electron and hole transfer rate (2.1×10^7 s^{-1}) in presence of MWCNTs (Figure 3.4b & f and Scheme II) confirms that the high electrical conductivity facilitates efficient electron transport, thereby reducing electron-hole recombination and ensuring that charge carriers effectively reach the electrode to contribute to the water splitting process.

Table 3.2 Electron transfer rate and hole transfer rate calculated from PL lifetime studies for all the photoanode samples.

Photoanodes	K_{et} $(10^7 s^{-1})$	K_{ht} $(10^7 s^{-1})$
TiO_2 core/shell QDs	1.8386	1.0137
T-M core/shell QDs	2.1482	1.3233
TiO_2 core QDs	0.4546	0.3786
T-M core QDs	0.3457	0.2697

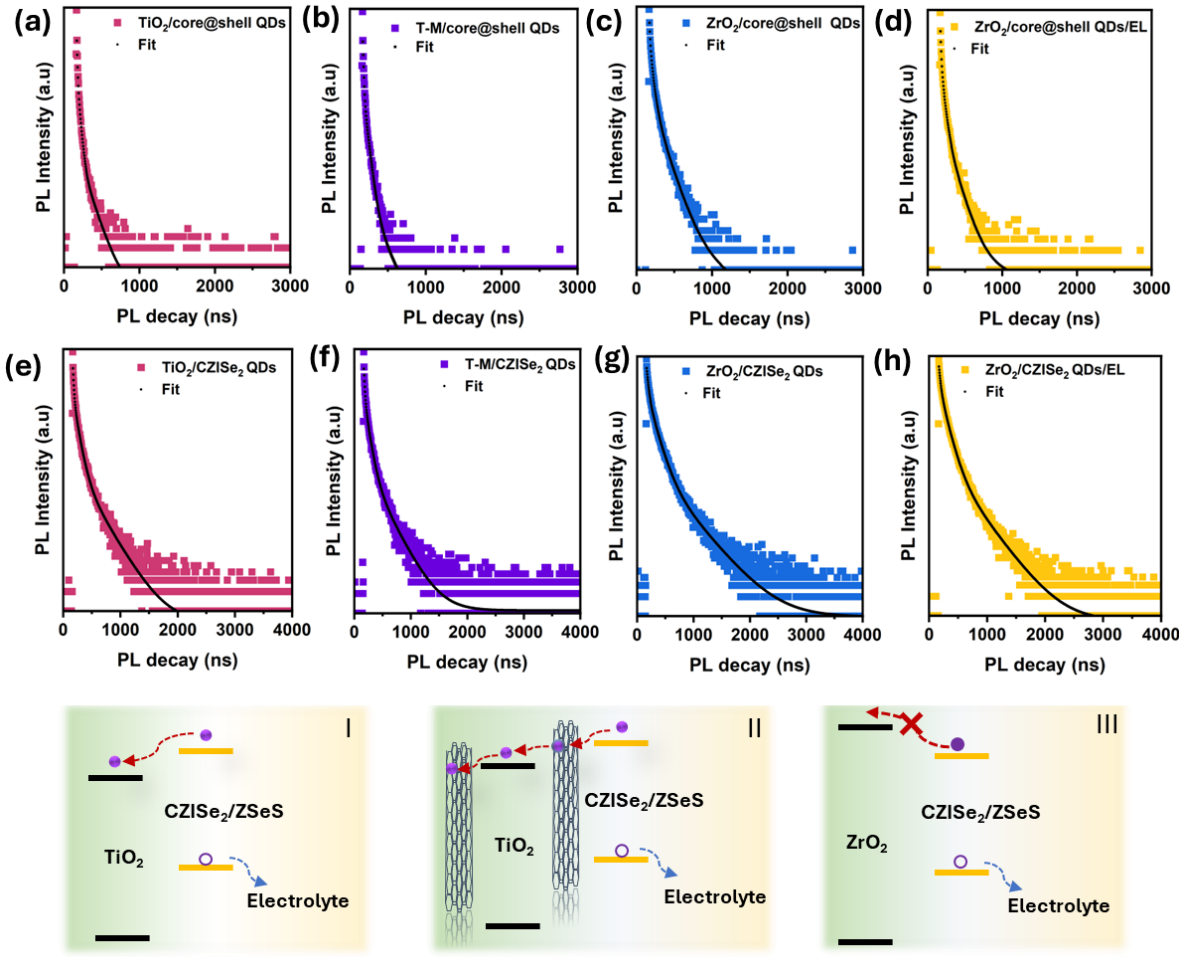

Figure 3.6 Transient PL decay curve of (a) TiO_2-core@shell QDs, (b) TiO_2-MWCNTs/core@shell QDs, (c) ZrO_2-core@shell QDs, (d) ZrO_2-core@shell QDs-Electrolyte, (e) TiO_2/$CZISe_2$ QDs, (f) TiO_2-MWCNTs/$CZISe_2$ QDs, (g) ZrO_2/$CZISe_2$ QDs, (h) ZrO_2/$CZISe_2$ QDs/Electrolyte. The schematic illustration shows the charge transfer for core/shell QDs in three different configurations: TiO_2 (I), TiO_2-MWCNTs (II) and ZrO_2 (III).

3.5 Photoelectrochemical performance

To assess the potential of the designed $CZISe_2$/ZSeS QDs for PEC H_2 production, we fabricated the photoanodes based on QDs and evaluated the PEC performance of the corresponding photoanode. The purified QDs were deposited on TiO_2 by EPD, and the elemental distribution of QDs were studied by EDS and SEM imaging. EDAX spectra shows the appearance of peaks corresponding to energy levels of different elements present in QDs (Cu, Zn, In, S, Se, Ti, O) (Figure 3.7a & d) and the corresponding weight percentage are listed in Table 3.3. In $CZISe_2$/ZSeS QDs, the weight content of Zn, Se increase and presence of S energy levels indicates the ZSeS shell formation. The average thickness of $CZISe_2$-TiO_2 and $CZISe_2$/ZSeS-

TiO_2 is 25.44 μm and 26.21 μm (Figure 3.7b and 3.7e). In addition, the elemental mapping shows the homogenous distribution of all elements including Zn, In, Se, S, Cu, Ti and O (Figure 3.7c and 3.7f). To protect QDs from photo corrosion and undesired charge recombination, we deposited ZnS layers of two cycles using SILAR based approach.

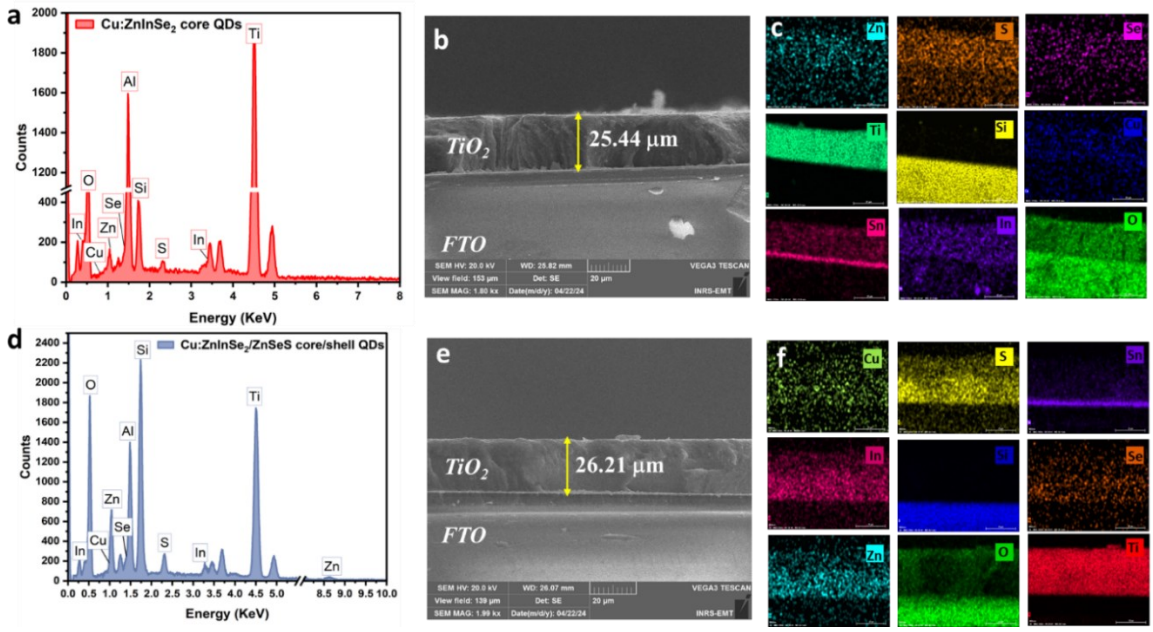

Figure 3.7 (a) EDAX spectra (b) cross-sectional SEM image, (c) EDS mapping of $CZISe_2$ core QDs and (d) EDAX spectra, (e) cross-sectional SEM image, (f) EDS mapping of $CZISe_2$/ZnSeS core/shell QDs.

The PEC performance was subsequently evaluated by using the as fabricated photoanode as working electrode. According to the Michael Faraday law, the amount of substance liberated (H_2) at an electrode is directly proportional to the charge (Q) thereafter photocurrent density is chosen as indicator to evaluate the activity of electrode [206]. In a typical PEC cell, the three-electrode system consists of a working electrode, Pt sheet as counter electrode and Ag/AgCl electrode saturated with KCl as reference electrode. All the electrodes were immersed into a strong alkaline electrolyte (Na_2S/Na_2SO_3, pH≈ 13) solution. The change in current value under applied potential (-1.2 to 0 mV) was measured, since the number of electrons set free at the anode is equal to the number of electrons reacting at the Pt electrode to split H_2O and produce H_2. Figure 3.11a-d shows the photocurrent density-potential (J-V) curve of different photoanodes under dark, continuous (AM 1.5 G 1 sun illumination) and chopped conditions. The saturated photocurrent density of bare $CZISe_2$ QDs is 10.91 mA/cm^2 (at 0.8 V vs RHE) as depicted in Figure 3.11a. The $CZISe_2$/ZSeS QDs exhibit higher photocurrent density of 11.80 mA/cm^2 (Figure 3.11b). This improved photocurrent density can be attributed to the suppression

of surface traps/defects through effective surface passivation. In addition, the energy loss associated with charge transfer is prevented owing to the enough surface passivation, which facilitate the photoexcited electron transfer from QDs to TiO_2. Although the $CZISe_2$/ZSeS QDs shows wider photo absorption, the enhanced photocurrent density of $CZISe_2$/ZSeS QDs is due to the advantage of high electron transfer rate.

To enhance charge transport properties for PEC water splitting, highly conductive MWCNTs were integrated with TiO_2. Due to the addition of small amount (0.015wt%), we did not observe the XRD peaks corresponding to MWCNTs in the TiO_2/MWCNTs-QDs (Figure 3.8).

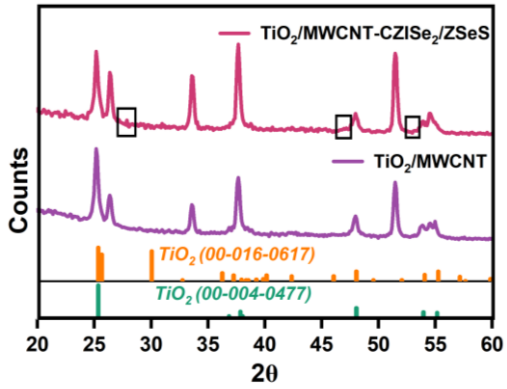

Figure 3.8 XRD spectra of TiO_2/MWCNTs-$CZISe_2$/ZSeS QDs and TiO_2/MWCNTs photoanode.

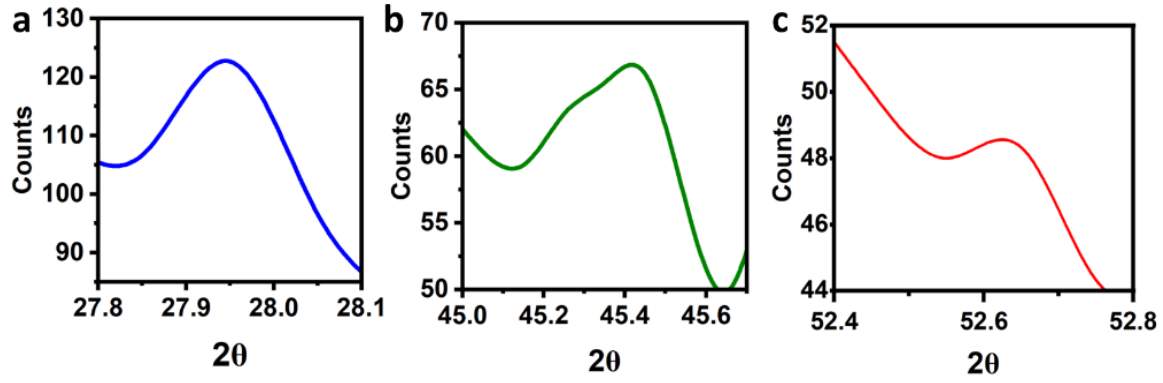

Figure 3.9 XRD spectra of TiO_2/MWCNT-$CZISe_2$/ZSeS QDs at different intervals (a) 27.8 – 28.1°, (b) 45.0 – 45.7° and 52.4 – 52.8°.

The structural integrity of the QDs deposited on the TiO_2/MWCNTs hybrid was confirmed by the presence of the $ZnInSe_2$ tetragonal crystal structure as observed in the XRD pattern (Figure 3.9). The QDs were sensitized on TiO_2-MWCNTs (T:M) to evaluate the PEC performance. We observed an enhanced photocurrent density of 11.23 mA/cm^2 for the T:M-$CZISe_2$ QDs (Figure

3.11c). The highest saturated photocurrent density for T:M-CZISe$_2$/ZSeS QDs based PEC cells is 13.15 mA/cm^2, which is 11.4% higher than the PEC cells based on T-CZISe$_2$/ZSeS QDs (Figure 3.11d-e). The photocurrent density of TiO$_2$-MWCNTs is 20% higher than the bare TiO$_2$ (Figure 3.10).

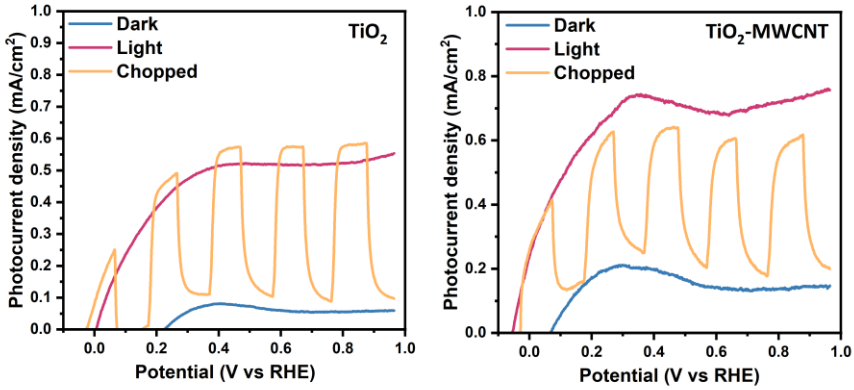

Figure 3.10 Photocurrent density (J) vs applied potential (V vs RHE) for TiO$_2$ (Left) and TiO$_2$-MWCNTs (right).

The beneficial effects of the introduced MWCNTs (0.015 wt%) is the better charge transport and inhibited charge transfer resistance, thereby greater collection of electrons. Theoretical simulations have been performed to understand the spatial electron/hole distribution within QDs by solving the stationary Schrödinger equation in a spherical geometry. The spatial overlap of electron and hole wavefunctions within QDs provide crucial insights to achieve higher photoexcited electron transfer efficiency, as it directly competes with the e-h recombination. Reducing the spatial overlap between electrons and holes decreases the probability of their recombination, thereby promoting their spatial separation. Figure 3.11f-g represents the comparison of variation of calculated e-h wavefunction overlap probability for CZISe$_2$ QDs and CZISe$_2$/ZSeS core/shell QDs. CZISe$_2$/ZSeS core/shell QDs exhibit a decrease of spatial e-h overlap area compared to CZISe$_2$ QDs. Therefore, in CZISe$_2$/ZSeS core/shell QDs, the delocalization of electrons and holes from the core to the shell region have significantly reduced the e-h recombination, thereby enhancing charge transfer efficiency. The theoretical simulation results are found to be consistent with experimental studies.

Figure 3.11i depicts the proposed schematic representation of working mechanism of QDs-TiO$_2$ based PEC device for hydrogen evolution. Under solar light irradiation, the photon energy larger than the band gap of QDs are absorbed, generating electron/hole (e^-/h^+) pairs. In CZISe$_2$/ZSeS QDs, the electrons will transfer from CZISe$_2$ QDs to ZnSe shell while the holes are captured by Cu^+ state, and electrolyte scavenge the holes. Further, the electron leak into

ZnS and subsequently, due to the favourable band electronic band bending, the electrons transfer to CB of TiO_2. Then, electron moves to Pt counter electrode through FTO, and the proton reduction (H^+) produces H_2. The ZSeS shell increases the carrier transfer efficiency by providing strong driving force and suppressed recombination for effective carrier separation. In comparison, the $CZISe_2$ QDs have high surface traps/defects that reduces the number of charge carriers for injection into TiO_2 and participate in water splitting reactions.

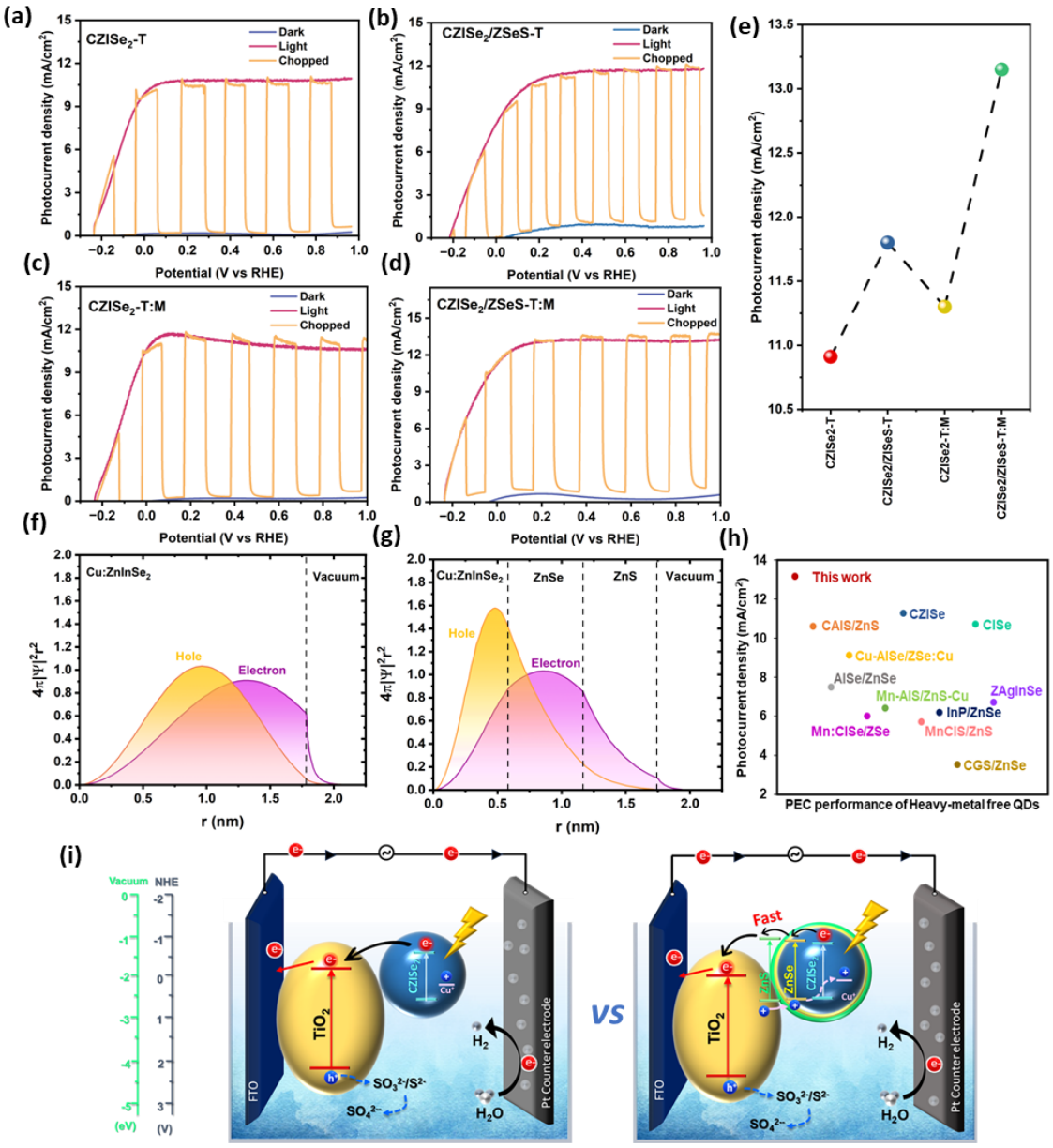

Figure 3.11 J-t plots of (a) FTO|TiO_2|$CZISe_2$ QDs|ZnS, (b) FTO|TiO_2|$CZISe_2$/ZSeS QDs|ZnS, (c) FTO|MWCNTs|TiO_2|$CZISe_2$, (d) FTO|MWCNTs|TiO_2|$CZISe_2$/ZSeS in the dark, under chopped and continuous 1 sun illumination (AM 1.5 G, 100 mW/cm²), (e) Comparison of J values at 0.8 V vs RHE for all the samples, (f) The approximate band alignment and schematic diagram of $CZISe_2$/ZSeS QDs sensitized TiO_2 photoanodes.

To get deeper understanding of transfer and recombination of charge carriers at the interface of QDs/TiO_2 and QDs/TiO_2/electrolyte, we conducted transient photovoltage decay measurements to measure the open-circuit voltage (V_{oc}) decay curves. The PEC device was illuminated for 20 sec to reach steady state condition, followed by shutting down to observe the recombination rate, and the voltage decay were recorded. Upon illumination, the band gap excitation of QDs leads to the separation of electrons and holes. The photoexcited electrons are injected into the CB of TiO_2 and accumulate there, while the photoexcited holes are captured by the electrolyte at the interface. The V_{oc} reaches a steady state when there is a balance between the accumulation of electrons and the recombination of carriers. Figure 3.12a depicts the representative V_{oc} decay curves for the QDs based PEC devices. A significantly slower V_{oc} decay is displayed for T:M-$CZISe_2$/ZSeS QDs than the PEC devices based on T-$CZISe_2$/ZSeS QDs, T:M-$CZISe_2$ QDs and T-$CZISe_2$ QDs. The photogenerated electron lifetime was calculated from the obtained V_{oc} decay, according to the following equation (Equation 11):

Equation 11 Photogenerated electron lifetime calculated from open-circuit decay values.

$$\tau = \left(\frac{K_B T}{e}\right) * \left(\frac{dV_{oc}}{dt}\right)^{-1} \quad (11)$$

Where T is temperature, K_B is Boltzmann's constant, e is the charge of the electron, τ is the potential dependant electron lifetime, and V_{oc} is the open circuit potential values. The longer electron lifetime relates to the higher electron collection, which is due to the efficient suppression of non-radiative recombination at the QDs/TiO_2/electrolyte interfaces. The observed results are in consistent with the PEC performance of the $CZISe_2$ QDs and $CZISe_2$/ZSeS QDs based photoanodes (Figure 3.12b).

The charge transfer resistance (R_{ct}) behavior of the electrode interfaces was studied by electrochemical impedance spectroscopy (EIS). EIS measurements were conducted under dark conditions in the frequency range from 100 KHz - 1Hz. In Nyquist curve, the diameter of the semicircle at mid-frequency is directly related to the R_{ct} [207]. Generally, the smaller arc radius of the semicircle indicates lower R_{ct}, which means an improved charge transfer. Figure 3.12c depicts the Nyquist plots of the as fabricated PEC devices. The observation clearly demonstrates an inverse trend in terms of photocurrent values obtained T:M-$CZISe_2$/ZSeS QDs> T:M-$CZISe_2$ QDs>T-$CZISe_2$/ZSeS QDs>T-$CZISe_2$ QDs. Thus, the improved charge transfer ability of the constructed photoanode can be attributed to better charge separation efficiency that affirms the reduced exciton recombination in this ZSeS architecture.

In view of practical applications, the long-term stability is another major challenge to be addressed during the operation of PEC cells. The long-term stability of QDs can be affected by the accumulation of charge carriers that are not transferred which eventually causes self-oxidation and decrease in photocurrent stability over time [208]. To investigate the long-term operation stability, we applied -0.6 V vs RHE under continuous 1 sun illumination for 3600s. To compare the long-term stability performance of the photoanodes, the current density values were normalised by dividing it with initial photocurrent value. Figure 3.12d shows the photocurrent density vs time for PEC cells based on QDs-T and QDs-T:M. The T-$CZISe_2$ QDs and T-$CZISe_2$/ZSeS QDs maintain 60% and 67% of initial current values illuminated for 3600s. The poor long-term stability of T- $CZISe_2$ QDs could be attributed to the hole induced self-oxidation which results in degradation of QDs [209, 210]. As a result of uniform surface passivation by our approach, i.e., growth of ZSeS shell, the QDs exhibit improved (~7%) compared to bare $CZISe_2$ QDs. At the same time, the T:M-$CZISe_2$/ZSeS QDs and T:M-$CZISe_2$ QDs maintain 76 and 80% of its initial current values. The device stability is much better than most of the reported environment-friendly QDs based PEC cells [123, 211-213] [214, 215]. The high photocurrent stability of QDs-T integrated with MWCNTs is primarily due to the enhanced electron transport and collection efficiency, as well as the reduced charge transfer resistance. The structural defects in TiO_2, which typically undermine long-term stability, are mitigated by the incorporation of MWCNTs [153].

Table 3.3 Comparison of atomic and weight percentages of elements in $CZISe_2$ core and $CZISe_2$/ZSeS core/shell QDs.

Elements	$CZISe_2$ QDs		$CZISe_2$/ZSeS core/shell QDs	
	Atomic (%)	Weight (%)	Atomic (%)	Weight (%)
Ti	42.15	37.35	7.99	14.99
O	75.19	45.38	78.51	49.22
Cu	0.07	0.16	0.04	0.02
Zn	0.14	0.31	0.13	0.34
In	0.28	1.20	0.18	0.81
Se	0.14	0.43	0.15	0.46
S	0.20	0.24	0.33	0.42

Si	3.33	3.52	12.69	13.96

Several works have recently been reported on environment friendly QDs based PEC device for H_2 production. A comparative table of some of typical results are listed in Table 3.4 and the photocurrent density of different environment friendly QDs based PEC device are shown in Figure 3.12d. This work focused on both improving the photocurrent density and long-term operational stability. Long et al. [214] reported an improved stability of 71% of the initial value after 1 h chopped irradiation for ZAISe QDs/TiO_2-0.015 wt% GO but with a low photocurrent density (6.7 mA/cm^2). At the same time, Luo et al. [178] reported Cu5%ZnInSe(1:4) QDs-TiO_2 photoanode with 60% retention of initial photocurrent value of ~10 mA/cm^2. To the best of our knowledge, among the reported environment friendly QDs based photoanodes, the highest photocurrent density obtained was ~11 mA/cm^2. This work on T:M-CZISe_2/ZSeS QDs based photoanode have achieved a record photocurrent density of 13.15 mA/cm^2 at 0.8 V and excellent photocurrent stability (~80%) after continuous illumination for 3600s.

Table 3.4 Comparison of PEC performance of environment friendly QDs based photoanode reported in previous literatures.

Photoanode	**Photocurrent density (mA/cm^2)**	**Long-term stability**	**Voltage (RHE)**	**Ref.**
CuZnInSe_2/ZnSeS QDs-TiO_2/MWCNTs	13.15	80%	0.8 V	This work
CuZnInSe_2/ZnSeS QDs-TiO_2	11.80	67%	0.8 V	This work
Cu5%ZnInSe (Zn:In – 1:4) QDs/TiO_2	11.23	60%	0.8 V	[178]
CuZnInS_3 QDs/TiO_2	4.4	71%	0.6 V	[212]
AgInS_2 QDs/ZnS passivation/TiO_2	5.7	60%	1 V	[215]
Cu$In_{1.5}Se_3$ QD ZnS/SiO_2/TiO_2	8.5	47%	0.5 V	[216]
Ag$InSe_2$/AgInSeS/AgInS_2 core/shell QDs/TiO_2	1.3	50%	0.2 V	[211]
InP/GaP/ZnSe core/multi-shell QDs/TiO_2	4.3	90%	1.23 V	[217]

Mn-alloyed $AgInS_2$/Cu-doped ZnS core/shell QDs/TiO_2	5.7	73%	0.8 V	[218]
Cu-doped InP/ZnSe core/shell QDs/TiO_2	7.4	60%	0.6 V	[219]

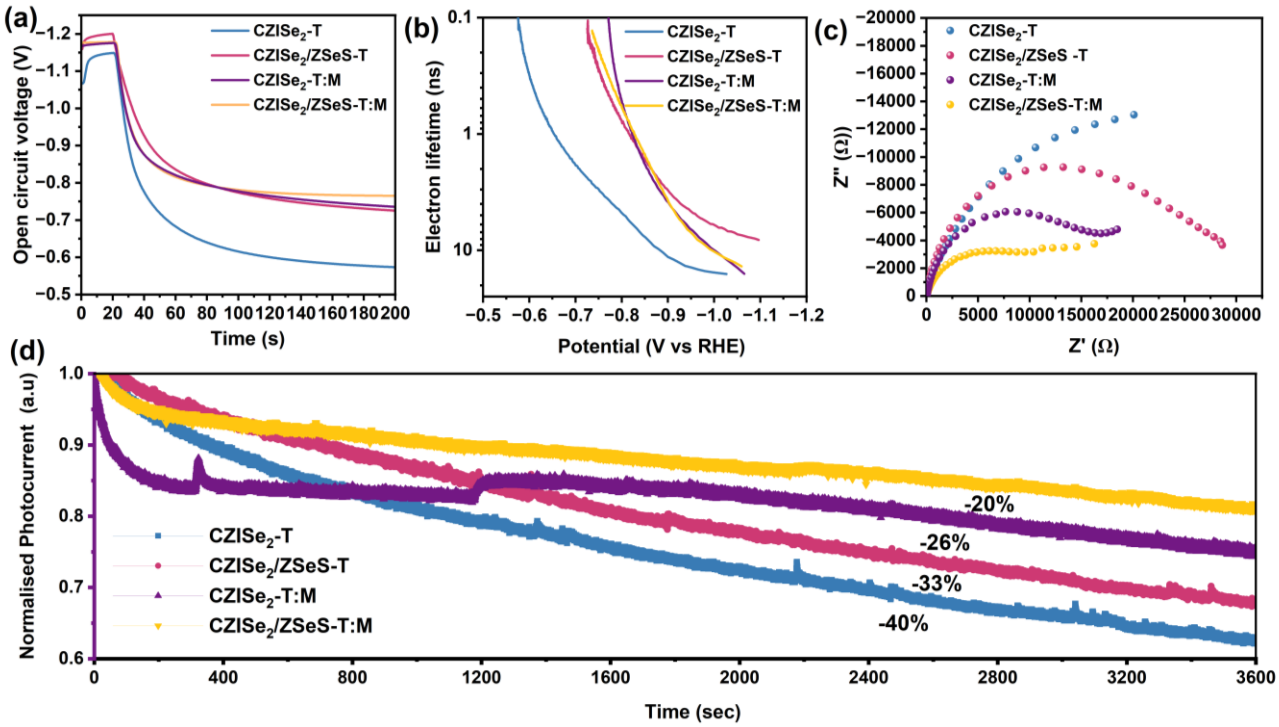

Figure 3.12 (a) Open circuit voltage vs Time (s), (b) Electron lifetime as a function of V_{oc}, (c) Nyquist plots and (d) J–t plots of photoanodes under 1 sun illumination at -0.6 V versus Ag/AgCl.

3.6 Summary

In summary, we adopted an in-situ growth strategy to fabricate ZSeS shell passivated $CZISe_2$ ($CZISe_2$/ZSeS) QDs via a single-step hot-injection technique. The synthesized QDs were sensitized on TiO_2 for solar-driven photoelectrochemical H_2 production. The T-$CZISe_2$/ZSeS QDs based PEC cells exhibit a 7.5% improvement in photocurrent density (11.80 mA/cm^2) compared to $CZISe_2$ QDs. This is mainly because of longer charge carrier lifetime and faster charge carrier injection rates with passivation of ZSeS shell. Charge carrier dynamic studies reveal efficient charge carrier separation at QDs/TiO_2 and electrolyte/QDs/TiO_2 interfaces. To further improve the PEC performance and long-term stability, we integrated MWCNTs. On adding MWCNTs, we obtained a remarkable photocurrent density of 13.15 mA/cm^2 at 0.8 V vs. RHE which is the highest photocurrent density reported among environment friendly QDs based

photoanodes. Further, the T:M-CZISe_2/ZSeS QDs based photoanode maintained ~80% of its initial current density after 3600s, highlighting its potential as an efficient photoanode for PEC H_2 production. Future research direction could focus on engineering a multi-shell structures and shape tunable architectures to broaden the light absorption range as well as enhance the charge extraction for high performance solar-to-fuel conversion efficiency and for other uses in optoelectronic applications.

Chapter 4: Dual aliovalent dopants Cu, Mn engineered heavy-metal-free QDs for ultra-stable anti-counterfeiting

4.1 Project Plan

Doping in semiconductor quantum dots (QDs) using optically active dopants tailors their optical, electronic, and magnetic properties beyond what is achieved by controlling size, shape, and composition. In this project, we synergistically modulated the optical properties of heavy-metal-free $ZnInSe_2$/ZnSe core/shell QDs by incorporating Cu-doping and Mn-alloying into their core and shell to investigate their use in anti-counterfeiting and information encryption. The effect on how the Cu and Mn dopants influence the optical properties such as PL lifetime, PL Intensity, and emission color of the core/shell QDs are studied. We hypothesize that the addition of Mn^{2+} ions to the ZnSe shell of Cu doped $ZnInSe_2$ QDs will not only improve the fluorescence efficiency of the Cu-emitting core but also create new synergistic properties. These properties are expected to enhance both the photophysical behaviour and environmental stability, producing results not observed in individually doped QD systems. Luminescent inks were made by dispersing QDs directly into a PMMA matrix to write and print security labels. The invisible characteristics of inks make them highly versatile and suitable to print on different types of surfaces, including paper, glass, rubber, wood, steel, and fabrics. The thermal and water stability of the printed patterns were investigated to validate their ability to form highly stable concealed ink for anti-counterfeiting. This work is published in Chemistry European A Journal 202402026 (*https://doi.org/10.1002 /chem.202402026*).

4.2 Structural, morphology and optical properties

The schematic illustration of the synthesis of Cu:$ZnInSe_2$/Mn:ZnSe core/shell QDs via hot-injection technique and their corresponding structural evolution is depicted in Figure 4.1a. Firstly, the Cu:$ZnInSe_2$ QDs were synthesized by inducing the nucleation process with rapid injection of Se into the hot-coordinating solvents that contain Cu, Zn and In precursor at 200 °C. After core growth for 25 min, the shell precursors (Zn, Mn and Se) were introduced sequentially at elevated temperature (220 °C) to induce the growth of Mn:ZnSe shell over the Cu:$ZnInSe_2$ QDs.

The XRD pattern of $ZnInSe_2$ QDs shows three distinct peaks at 2θ = 27.56°, 45.69°, and 53.44°, corresponding to the (112), (204) and (312) planes of tetragonal $ZnIn_2Se_4$, respectively (see the

JCPDS 85-1409 reference, provided as stick pattern at the bottom of Figure 4.1c). In Cu:$ZnInSe_2$ QDs, the absence of secondary peaks related to Cu or CuO indicates that the crystal structure remains unaltered after the introduction of Cu dopant. Upon growth of the ZnSe shell, a gradual shift to higher diffraction angles is observed due to the smaller lattice constant of ZnSe (5.61 Å) than $ZnIn_2Se_4$ (5.70 Å), indicating the formation of an epitaxial shell (JCPDS 010-080-0021, provided as stick pattern in Figure 4.1b) [220]. In addition, individual peaks related to ZnSe are not observed, which confirms the formation of core/shell structure only. Upon Mn alloying in the ZnSe shell, a slight shift to lower diffraction angles is observed which is attributed to the decrease in Zn content [221]. Figure 4.1c-f illustrates typical HR-TEM images of the as-synthesized $ZnInSe_2$, Cu:$ZnInSe_2$, Cu:$ZnInSe_2$/ZnSe, and Cu:$ZnInSe_2$/Mn:ZnSe core/shell QDs. All the prepared QDs are found to exhibit quasi-spherical shapes with narrow size-distribution. The diameters of QDs are estimated to be 2.87±0.48, 3.20±0.33, 2.99±0.45 and 3.02±0.24 nm for $ZnInSe_2$, Cu:$ZnInSe_2$, Cu:$ZnInSe_2$/ZnSe, and Cu:$ZnInSe_2$/Mn:ZnSe core/shell QDs. Such a uniformity in size reported for Cu:$ZnInSe_2$ and Cu:$ZnInSe_2$/ZnSe core/shell QDs is attributed to the thin shell obtained with a growth time of 1 min.

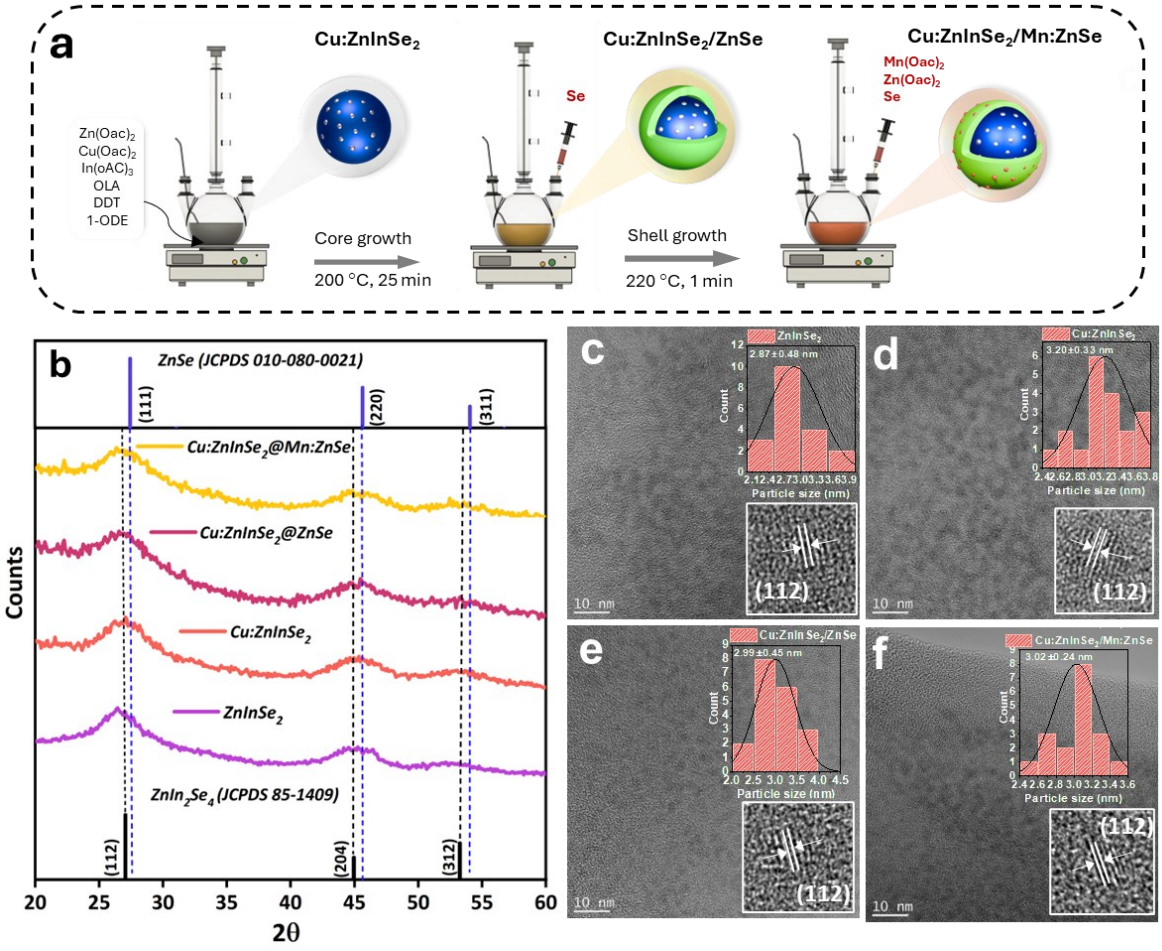

Figure 4.1 (a) Schematic representation of the synthesis of Cu:ZnInSe$_2$@Mn:ZnSe core/shell QDs. (b) XRD patterns of ZnInSe$_2$, Cu:ZnInSe$_2$, Cu:ZnInSe$_2$@ZnSe and Cu:ZnInSe$_2$@Mn:ZnSe. HR-TEM images, inset size-distribution histogram plot and interplanar distance of (c) ZnInSe$_2$, (d) Cu:ZnInSe$_2$, (e) Cu:ZnInSe$_2$@ZnSe core/shell QDs and (f) Cu:ZnInSe$_2$@Mn:ZnSe core/shell QDs.

The measured interatomic spacing is identical for all samples and associated with the (112) planes of the tetragonal ZnInSe$_2$ crystal structure (in the inset of Figure 4.1c-f). The small size distribution of QDs, as revealed from TEM observation, is consistent with the distinct optical absorption peaks presented in Figure 4.2a. ZnInSe$_2$ QDs display an optical absorption onset at 480 nm. Cu:ZnInSe$_2$ displays an absorption peak onset at 580 nm with a gradual increase in absorption range towards longer wavelengths (700 nm). After overcoating the ZnSe shell, the absorption peak is blue-shifted from 580 to 500 nm, while a redshift is observed with Mn alloying into the ZnSe shell. Similarly, as shown in Figure 4.2b, the photoluminescence (PL) emission peak of Cu:ZnInSe$_2$/ZnSe core/shell QDs is blue-shifted by 25 nm compared to the Cu:ZnInSe$_2$ core QDs emission. The observed blue shift can be attributed to the reduced core diameter resulting from the exchange of In^{3+} or Cu^{2+} with excess Zn^{2+} during surface passivation [204].

After Mn incorporation, the PL peak of Cu:$ZnInSe_2$/Mn:ZnSe core/shell QDs is slightly redshifted to display a single emission peak at 606 nm. From our observations, the QDs having both dopants but a single PL emission peak suggest that the recombination is allowed with the involvement of one dopant state. Generally, the Mn d-d transition can only be obtained when both electron and hole migrate towards their d-states, and the emission is spin-forbidden, which results in longer lifetimes of several hundreds of milliseconds [222]. Based on previous spectral observations of Mn-doped QDs reported in the literature [55-57], a PL emission peak should be centred at ~580 nm and show milliseconds PL lifetime to confirm the existence of Mn d-states emission. The absence of such a phenomenon clearly indicates that the Cu emission becomes the allowed one. To examine the influence of Mn in the absence of Cu luminescence centers, the optical properties of $ZnInSe_2$/ZnSe and $ZnInSe_2$/Mn:ZnSe have been investigated. Compared to undoped $ZnInSe_2$/ZnSe, PL emission spectra of $ZnInSe_2$/Mn:ZnSe exhibit a moderate redshift with PL emission peak centred at 577 nm, indicating the occurrence of band edge emission (Figure 4.3). The PL emission spectra of $ZnInSe_2$/Mn:ZnSe and $ZnInSe_2$/ZnSe core/shell QDs exhibit narrow peaks compared to $ZnInSe_2$ QDs. This narrowing can be attributed to the slow rise in temperature during the shell growth that effectively mitigates Ostwald ripening of the cores [223]. By preventing the Ostwald ripening, a more uniform size distribution of the QDs is maintained, resulting in narrower PL emission peaks. The PL emission intensity of Cu:$ZnInSe_2$/Mn:ZnSe core/shell QDs is enhanced 1.2 and 3.75 times compared to Cu:$ZnInSe_2$/ZnSe core/shell QDs and bare Cu:$ZnInSe_2$ QDs, respectively, as a consequence of effective passivation provided by the Mn alloyed ZnSe shell (Figure 4.4). The PL spectral data have been converted to Commission Internationale de l'Eclairage (CIE 1931) colour coordinates and the chromaticity characteristics of the prepared QDs are shown in Figure 4.2d. The fluorescence color of all QDs exhibit monochromatic light with excellent color discrimination properties. The color coordinates corresponding to the fluorescence of prepared QDs are listed in the inset table of Figure 4.2d.

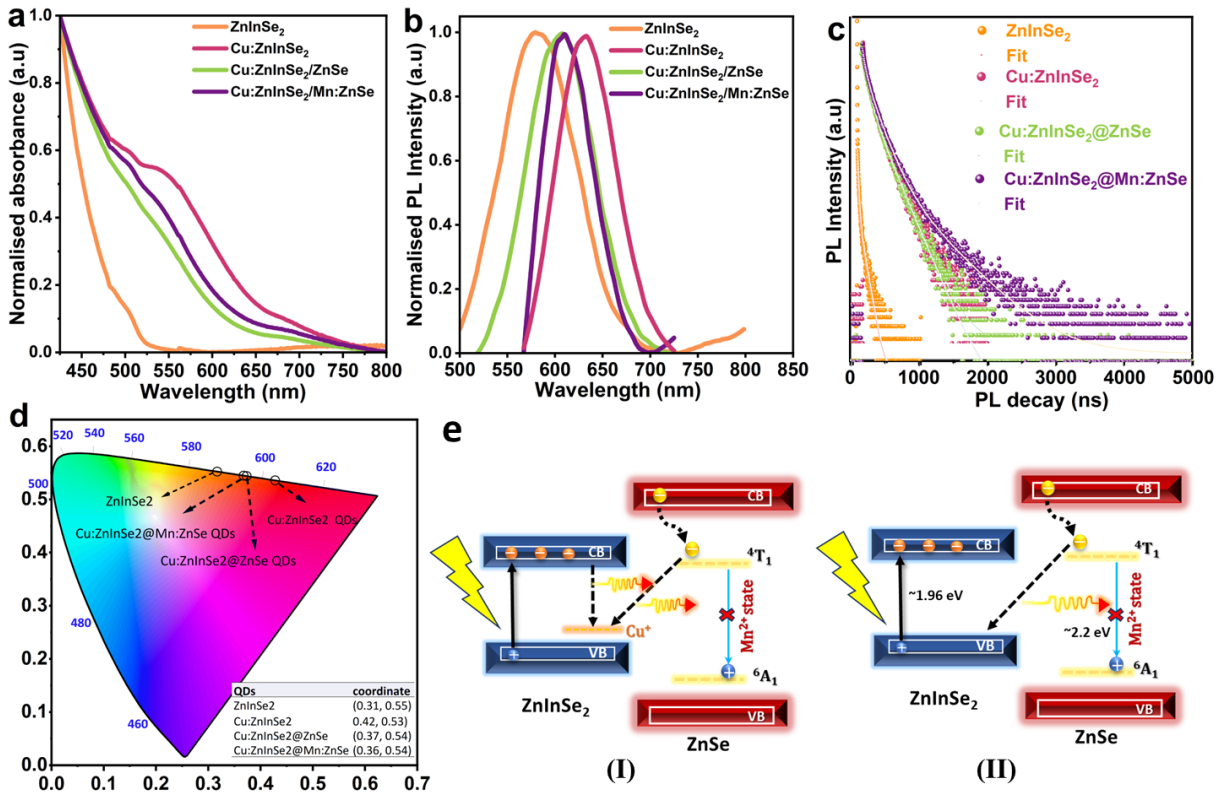

Figure 4.2 (a) Normalized absorption spectra, (b) Normalized PL emission spectra, (c) Time-resolved PL decay curves, (d) CIE chromaticity coordinates of of $ZnInSe_2$, $Cu:ZnInSe_2$, $Cu:ZnInSe_2$@ZnSe and $Cu:ZnInSe_2$@Mn:ZnSe QDs. (e) Proposed possible mechanism of PL emission of $Cu:ZnInSe_2$/Mn:ZnSe (I) and $ZnInSe_2$/Mn:ZnSe (II).

The transient PL decay curves of the QDs dispersed in toluene have been measured for an excitation wavelength of 500 nm. The PL lifetime is characterized by three major processes, as follows: (i) short lifetime of non-radiative decay process (τ_1), (ii) medium lifetime of radiative decay process due to recombination of photogenerated carriers (τ_2), and (iii) long lifetime related to the energy transfer process (τ_3). Each component that contributes to the multiexponential decay is linked to a distinct PL decay channel, and the representation of each channel is reflected by its respective relative amplitude. The average fluorescence decay of the prepared $ZnInSe_2$ is calculated to be 7.28 ns. A much larger value of 153.70 ns was estimated for $Cu:ZnInSe_2$ QDs, due to the presence of the Cu^+ state, which captures the holes to produce long-lived hot electrons [224]. The $Cu:ZnInSe_2$/ZnSe core/shell QDs exhibit a longer lifetime of 167 ns, which is attributed to the delocalization of electrons from the core to the shell region. A largely prolonged average lifetime of 201.3 ns was measured after Mn alloying into the shell (Figure 4.4c).

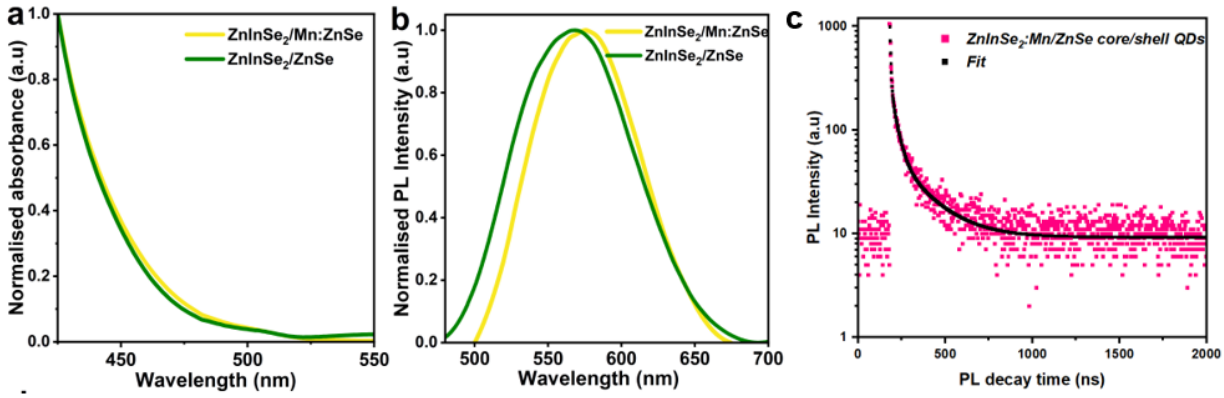

Figure 4.3 (a) Absorption spectra and (b) PL emission spectra of $ZnInSe_2$/ZnSe and $ZnInSe_2$/Mn:ZnSe. (c) PL lifetime of $ZnInSe_2$/Mn:ZnSe.

However, in the absence of Cu dopant, the average PL lifetime of $ZnInSe_2$/Mn:ZnSe is significantly reduced to 87 ns (Figure 4.3c) rather than a long lived PL emission of several milliseconds associated with the Mn d-d transition [225, 226]. The extended PL lifetime of Cu:$ZnInSe_2$/Mn:ZnSe core/shell QDs can be attributed to the decreasing probability of photocarriers' recombination which will be discussed later. The calculated average lifetime and fitted parameters of all the prepared QDs are listed in Table 4.1.

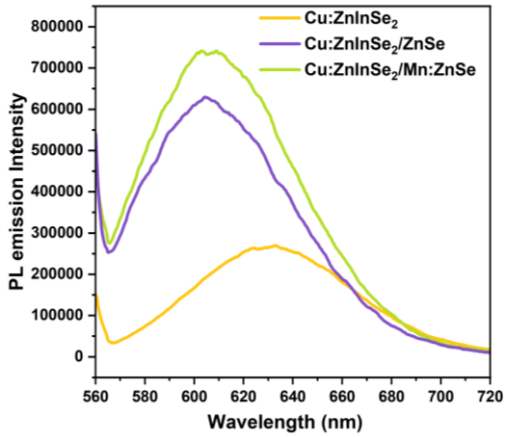

Figure 4.4 PL emission spectra of Cu:$ZnInSe_2$, Cu:$ZnInSe_2$/ZnSe core/shell QDs and Cu:$ZnInSe_2$/Mn:ZnSe core/shell QDs.

Table 4.1 Fitted parameters of transient PL decay curves for $ZnInSe_2$, Cu:$ZnInSe_2$, Cu:$ZnInSe_2$, Cu:$ZnInSe_2$/ZnSe and Cu:$ZnInSe_2$/Mn:ZnSe.

Sample	a_1	a_2	a_3	τ_1 (ns)	τ_2 (ns)	τ_3 (ns)	$\tau_{average}$
$ZnInSe_2$	102336.10	1331.12	127.03	1.29	13.25	77.22	7.28
Cu:$ZnInSe_2$	1605.8	2243.38	1045.23	15.1	84.08	224.12	153.70
Cu:$ZnInSe_2$/ZnSe	2918.91	1413.76	-	74.69	227.92	-	167.00
$ZnInSe_2$/Mn:ZnSe	1089.02	235.81	50.19	4.46	33.58	179.33	87.32
Cu:$ZnInSe_2$/Mn:ZnSe	3880.75	4597.8	376.63	42.57	161.44	498.54	201.30

4.3 Possible PL mechanism

A possible photoemission mechanism is proposed based on the aforementioned results. To elucidate the role of Cu and Mn dopants, the PL emission mechanism of Cu:$ZnInSe_2$/Mn:ZnSe (I) and $ZnInSe_2$/Mn:ZnSe (II) is depicted in Figure 4.2e. Depending on the bandgap of the host semiconductor, the ligand field states of $^4T_1$ and $^6A_1$ of the Mn doped ions could be involved in the PL emission. In our case, it is different from other Mn-doped wide band gap QDs [227-229], in which the Mn d-state are located between the VB and CB of host QDs. For the Cu:$ZnInSe_2$/Mn:ZnSe core/shell system, the electron (e-) excited to CB_{ZnInSe_2} undergoes radiative relaxation to the Cu^+ state. The e- in CB_{ZnSe} undergoes non-radiative relaxation to the Mn $^4T_1$ state, followed by radiative relaxation to Cu^+ state as the $^6T_1$ state lies below the VB_{ZnInSe_2}. In the absence of Cu^+ dopant in the $ZnInSe_2$/Mn:ZnSe core/shell system, the mechanism for radiative recombination differs from that observed in Mn-doped wide band gap semiconductors, where Mn d-d transitions are typically observed [230, 231]. In $ZnInSe_2$/Mn:ZnSe QDs, although the PL emission is at 580 nm, the absence of a longer PL lifetime associated with Mn d-d transition (milliseconds) indicates that a different recombination pathway may occur in this core/shell system. $ZnInSe_2$ has a narrower band gap (1.96 eV) with an absorption peak around 500 nm, lower than the Mn $^4T_1$-$^6A_1$ gap energy (2.12 eV). According to previous studies, the band edge positions of $ZnInSe_2$ QDs and Mn $^4T_1$-$^6A_1$ states are consistent with the observed PL emission characteristics [112, 178]. In this case, electrons that are excited from the VB to CB of the $ZnInSe_2$/ZnSe host undergo non-radiative relaxation to the

Mn $^4T_1$ level. Since the $^6A_1$ level lies below the VB of $ZnInSe_2$/ZnSe, the electrons relax radiatively towards the VB of $ZnInSe_2$ instead of the Mn $^6A_1$ level, consistent with the observed emission in $ZnInSe_2$/Mn:ZnSe. In addition, this unique exciton behavior leads to a significant red shift in the PL peak position which is consistent with the spectra shown in Figure 4.3b. A similar recombination mechanism has been reported by Zhang and co-workers for a narrow band gap Mn-doped PbS QDs system with no Mn d-d transitions and PL emission in the millisecond range [232].

4.4 Optical anti-counterfeiting application

In examining the potential of these QDs for practical applications in anticounterfeiting, our investigation focused on assessing the stability of the samples by studying the effect of heat and exposure to water on their optical properties. Firstly, the fabricated luminescent QDs ink is used to draw a letter pattern (“INRS”) onto a plastic sheet. The corresponding photograph has been taken under UV light (365 nm) as depicted in Figure 4.5. A bright luminescence color of red, orange and pink is observed for the luminescent inks prepared with Cu:$ZnInSe_2$ core, Cu:$ZnInSe_2$/ZnSe core/shell QDs, and Cu:$ZnInSe_2$/Mn:ZnSe core/shell QDs. All the deposited luminescent inks exhibit strong fluorescence whereas no fluorescence is evident for the ink prepared with the core $ZnInSe_2$ QDs. This lack of fluorescence is due to the presence of excess surface defects that act as nonradiative recombination centers [233]. Also, we did not examine the applicability of $ZnInSe_2$/Mn:ZnSe core/shell QDs and $ZnInSe_2$/ZnSe core/shell QDs for anticounterfeiting given that their PL emission is weak and their characteristics are similar to $ZnInSe_2$. To determine the stability of the ink sketched “INRS” pattern on plastic sheet, the plastic sheets were directly soaked into deionized water. The photographs of the representative water-soaked printed plastic sheets taken under UV light are illustrated in Figure 4.5. After four weeks, the Cu:$ZnInSe_2$ QDs undergo a faster fluorescence quenching and a gradual loss in brightness. The brightness of both Cu:$ZnInSe_2$/ZnSe core/shell QDs and Cu:$ZnInSe_2$/Mn:ZnSe core/shell QDs remained unchanged even after ten weeks. This improved stability is attributed to the complete surface passivation of core QDs with the suitable ZnSe and Mn:ZnSe shell layer. In such system, the shell serves as a barrier, preventing degradation and oxidation from external environmental factors.

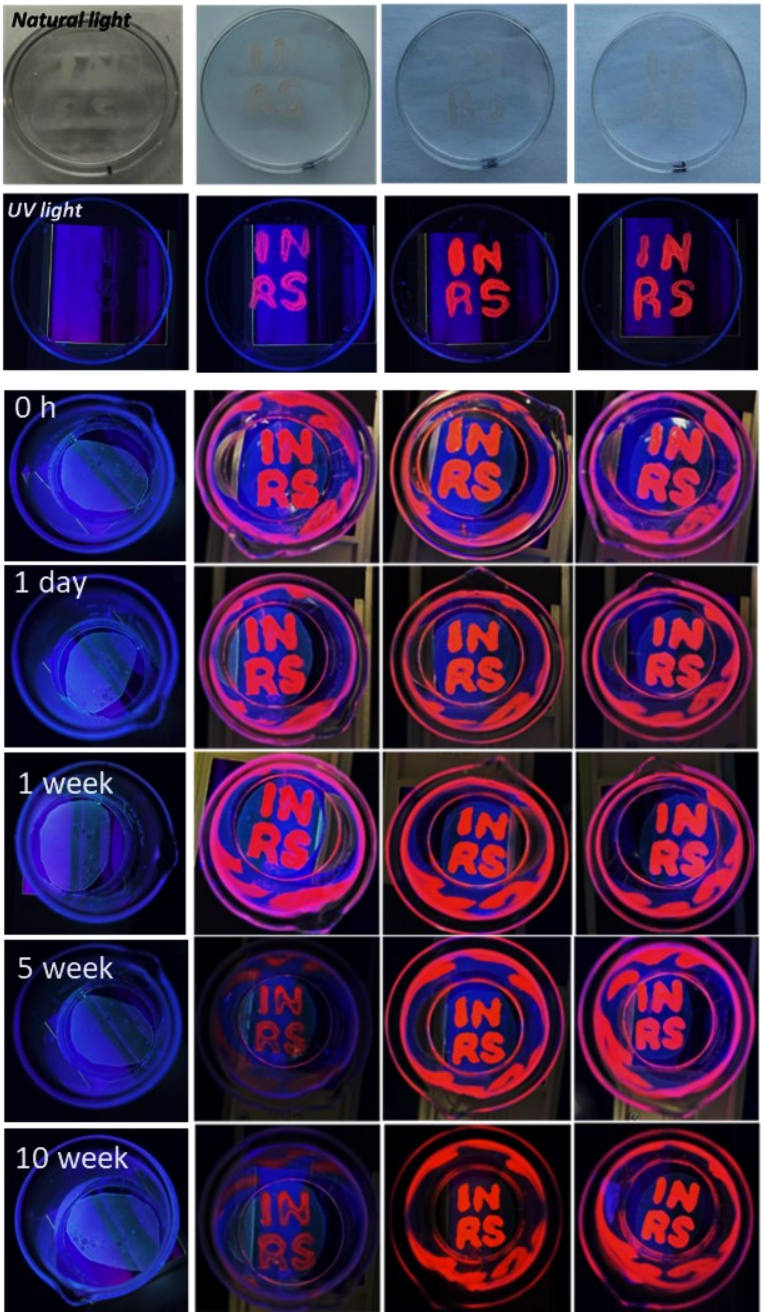

Figure 4.5 The letter "INRS" printed on a plastic sheet with the prepared luminescent inks using $ZnInSe_2$, Cu:$ZnInSe_2$, Cu:$ZnInSe_2$@ZnSe and Cu:$ZnInSe_2$@Mn:ZnSe QDs under normal light and UV light. Stability test - Photographs of the printed "INRS" plastic sheets placed inside water for ten weeks.

Temperature can significantly impact the stability and luminescence properties of materials used in security features for anticounterfeiting applications. Studying the influence of temperature allows to ensure the durability and reliability of security features to make them resistant to harsh environmental conditions. Similar "INRS" luminescent ink patterns were created on a glass to

investigate the thermal stability. These printed glasses were exposed to varying temperatures as high as 170 °C (Figure 4.6). The thermal studies were conducted only up to 170 °C due to the low boiling point (190 °C) of the PMMA polymer [234]. In sharp contrast to Cu:$ZnInSe_2$ core QDs, Cu:$ZnInSe_2$/ZnSe core/shell QDs and Cu:$ZnInSe_2$/Mn:ZnSe core/shell QDs maintained their fluorescence brightness even at elevated temperatures. It clearly reflects that the shell greatly improved the thermal stability of QDs. Figure 4.7a-d depicts the PL spectral change recorded from room temperature to 170 °C for the "INRS" printed on glass using the QDs ink. The PL intensity of Cu:$ZnInSe_2$ QDs was observed to decrease rapidly even below 90 °C due to the significant loss of Cu dopants at high temperatures, which leads to the drastic decrease of fluorescence (Figure 4.7b). The possible reason for fluorescence quenching of Cu:$ZnInSe_2$ QDs when exposed to heat can be due to the combination of ligand dissociation and surface oxidation [235]. For Cu:$ZnInSe_2$/ZnSe QDs, the degree of attenuation of PL intensity (55%) reduces significantly after ZnSe shell passivation at a high temperature of 170 °C, demonstrating a substantially enhanced thermal stability. In this regard, we consider that the ZnSe shell effectively passivates the electronic trap states by eliminating surface dangling bonds and prevents the possibility of agglomeration and thermal oxidation. This phenomenon could be well understood by introducing oxidation to the core QDs. The blue shift of the PL peak observed in Figure 4.7b after increasing the temperature can be attributed to several factors affecting the energy bandgap of QDs. For instance, the thermal expansion of the crystal lattice associated with the increase in temperature leads to a change in the electronic band structure, thus a blue shift in the PL peak [236]. Also, the electron-phonon coupling, where enhanced phonon interactions at higher temperatures increase the energy bandgap, causing a blue shift [237]. Furthermore, high temperatures cause ligand dissociation that leads to an incomplete ZnSe shell and allows oxygen diffusion into the core QDs, thus forming a $ZnCuInSe_2Ox$ layer that reduces core QD size and further contributes to the blue shift [238]. Despite this, the current level of thermal stability remains unsatisfactory and further needs to be improved because the PL decay was not suppressed completely. Following Mn:ZnSe shell encapsulation, 70% of PL intensity is maintained, which is 3.2 times higher than Cu:$ZnInSe_2$/ZnSe core/shell QDs (Figure 4.7c and d). Consequently, all of the instability issues that make Cu:$ZnInSe_2$ vulnerable can be overcome with passivation of suitable Mn:ZnSe Shell for superior stability under extreme environmental conditions. A comparative analysis of the stability performance of previously reported printed patterns based on QDs highlights the superior stability in water and thermal conditions achieved in our study (Table 4.2 Comparative table of stability performance of reported QDs based anti-counterfeiting devices**.**).

Table 4.2 Comparative table of stability performance of reported QDs based anti-counterfeiting devices.

QDs based anti-counterfeiting device	Water stability (Period/PL)	Thermal stability (Temp. /PL)	Ref
$Ti_3C_2T_x$ MXene QDs	-	80 °C/80%	[239]
C-dots@PVP	-	150 °C/70%	[240]
N-CDs	-	95 °C/90%	[241]
$CsPbBr_3$/LP/SiO_2 QD composites	35 min	-	[242]
CNC/QDs	3.5 h	-	[176]
$MAPbBr_3$@PbBr(OH) Nanocrystals	-	60 °C/80%	[243]
Mn-doped $CsPbCl_3$ QDs	40 min/53.56%	-	[244]
$CsPbBr_3$/PAN composite film	100 days/93.5%	-	[245]
$CsPbBr_3$@EuBTC composite	-	60 °C/80%	[246]
PMMA/Cu:$ZnInSe_2$@Mn:ZnSe QDs	10 weeks	170 °C/70%	This work

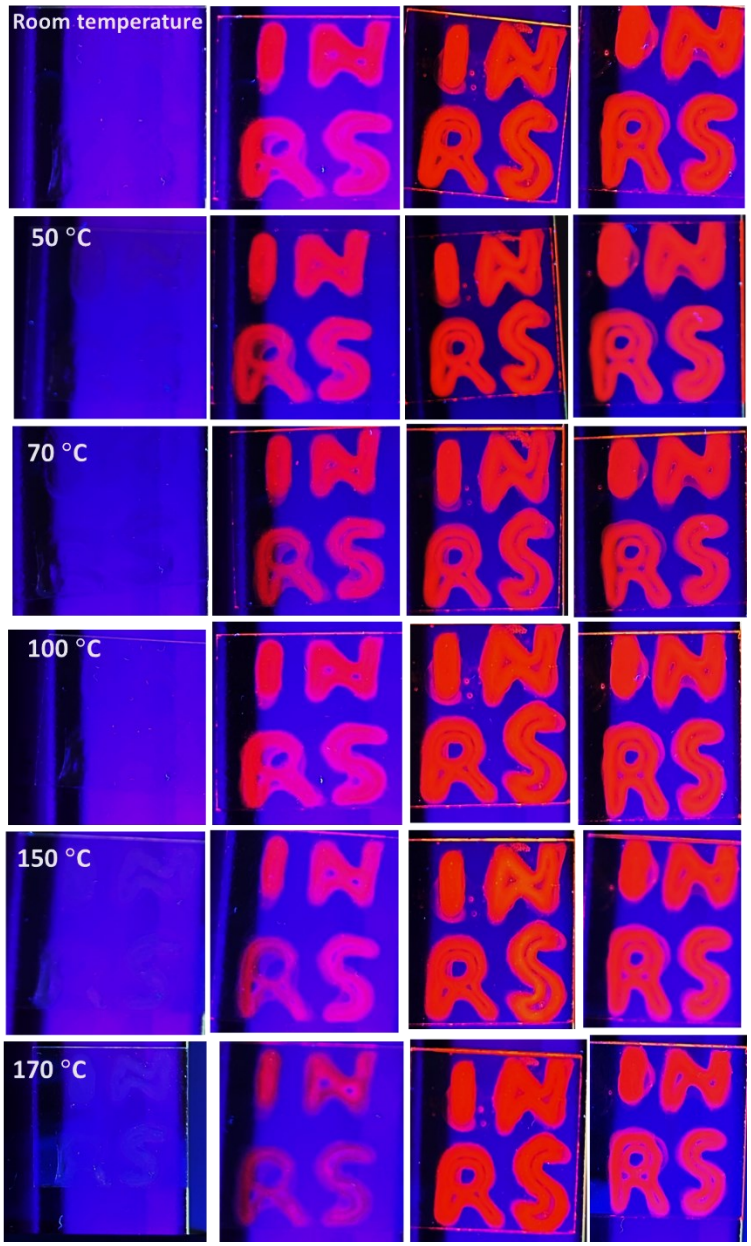

Figure 4.6 Digital photographs of "INRS" letter printed on glass using luminescent inks at different temperatures under UV light.

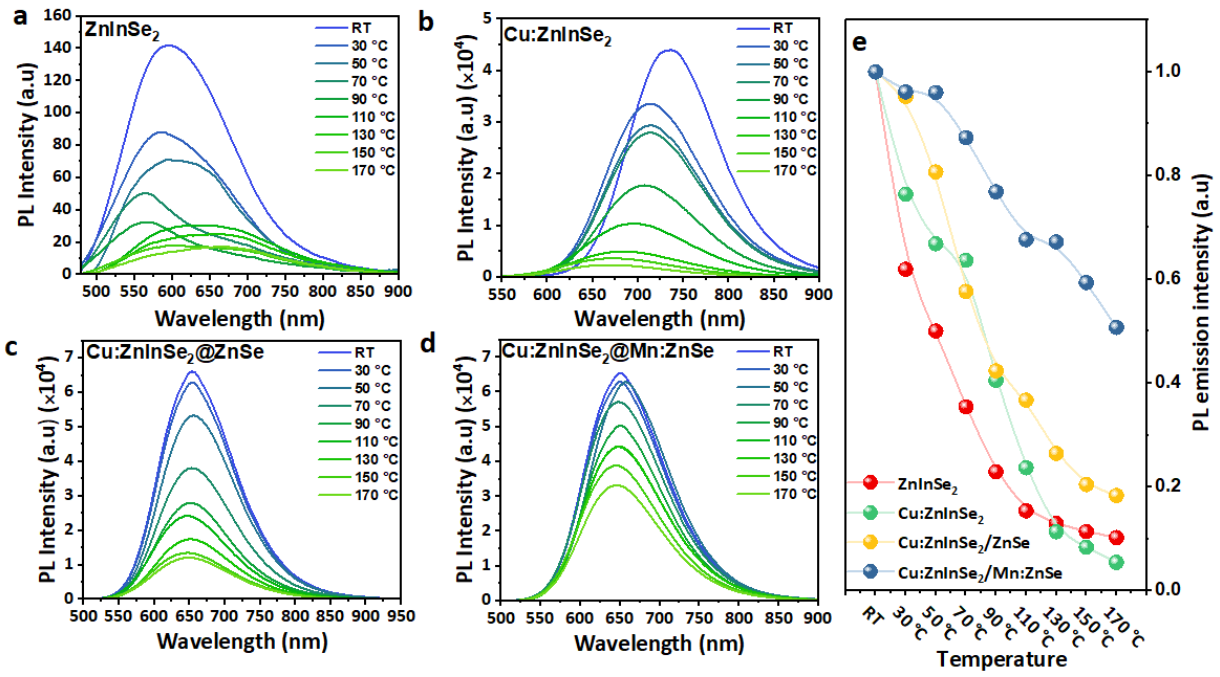

Figure 4.7 PL spectral change from room temperature to 170 °C of (a) $ZnInSe_2$, (b) $Cu:ZnInSe_2$, (c) $Cu:ZnInSe_2/ZnSe$, (d) $Cu:ZnInSe_2/Mn:ZnSe$ and the corresponding (e) Plot of relative PL emission change vs different temperatures.

To further realize the luminescent inks for practical anti-counterfeiting, the luminescent QDs inks are printed on most widely used packaging materials such as glass, plastic, rubber, metals, fabrics, and wood (Figure 4.8). These printed inks are invisible on all kind of surfaces and become visualized under UV light. In addition, the luminescent inks are compatible with flexible plastics and good fluorescence was visualized when submerged in water. Therefore, the fabricated luminescent QDs ink demonstrated excellent adaptability on to different type of surfaces for real-time anti-counterfeiting technologies.

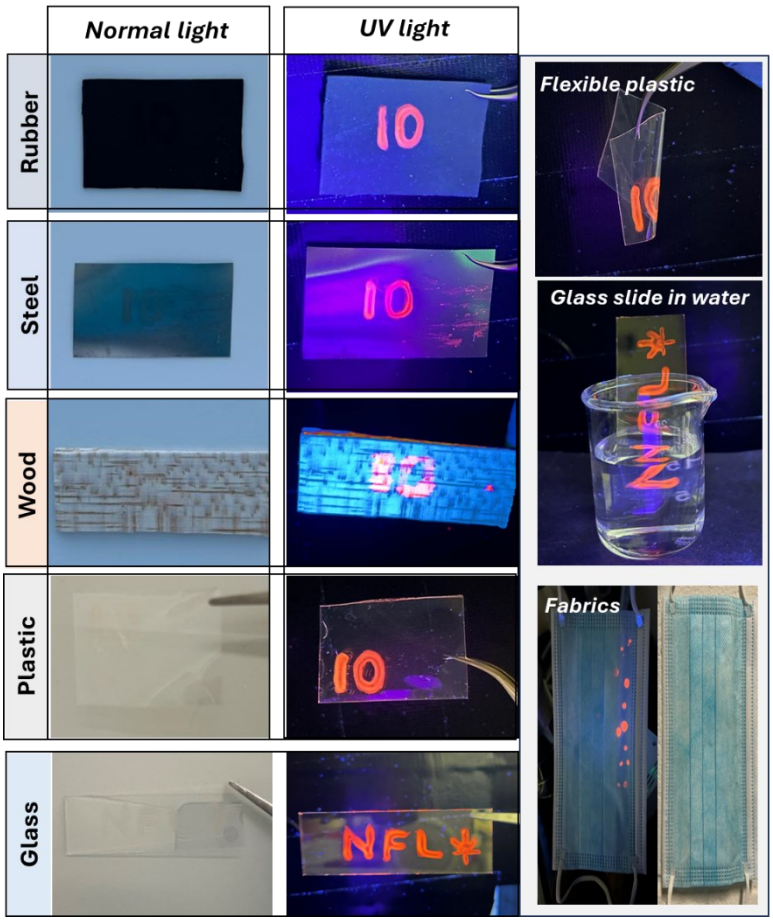

Figure 4.8 Image of luminescent ink printed on different materials under UV light and normal light.

4.5 Summary

In our study, we have effectively tailored the optical properties of heavy-metal-free $ZnInSe_2$/ZnSe core/shell QDs by employing a synergistic approach involving Cu doping inside core and Mn alloying into the shell. These engineered "green" Cu:$ZnInSe_2$/Mn:ZnSe QDs were used as luminescent security inks for anti-counterfeiting applications. Our findings reveal that Cu-doping within the $ZnInSe_2$ efficiently captures holes, while Mn alloying in the ZnSe shell provides mid-gap states for electron relaxation. This synergistic effect results in a significantly prolonged PL lifetime of 201 ns and improved PL emission intensity compared to Cu:$ZnInSe_2$/ZnSe and Cu:$ZnInSe_2$ QDs. Despite the presence of two optically active dopants (Cu and Mn), the Cu dopant emission is predominant in the Cu:$ZnInSe_2$/Mn:ZnSe due to the narrow band gap of host material as confirmed by PL spectra. The Cu and Mn dopants modulated core/shell QDs could produce huge coding capacity and realize complex information

encryption. The anti-counterfeit characteristics of the printed patterns remained intact even after direct water soaking for a prolonged period of 10 weeks. Furthermore, they exhibited superior thermal stability, retaining 70% of the PL intensity at 170°C. These results indicate that synergistic manipulation of Cu and Mn dopants in heavy-metal-free core/shell QDs shows promising potential to realize highly stable luminescent inks for anti-counterfeiting applications. Moreover, by exploring various transition metal ion dopants, we anticipate that more heavy-metal-free QDs with high-security features like our work will emerge in the near future.

CONCLUSION AND FUTURE OUTLOOK

In this thesis, heavy-metal-free colloidal core/shell QDs-based PEC devices and optical anti-counterfeiting devices were developed, and their performance was improved through different surface and interfacial engineering strategies. The first project focuses to enhance the stability and charge carrier generation/transportation of QDs-based PEC devices by shell engineering strategy. The goal of the second project is to develop a robust anti-counterfeiting device based on QDs that can encrypt complex security information and withstand harsh environmental conditions by using a dual dopant engineering strategy. The conclusion drawn for each project is as follows:

In chapter three, a ZnSeS alloyed shell overcoated Cu:$ZnInSe_2$ QDs ($CZISe_2$/ZSeS core/shell QDs) was designed and synthesized by an in-situ growth passivation approach. The $CZISe_2$/ZSeS core/shell QDs were decorated onto TiO_2 mesoporous film and applied as working photoanode in the PEC device for H_2 production. The objective of this project is to mitigate surface traps and defects in $CZISe_2$ core QDs by employing a ZnSeS alloyed shell, thereby reducing non-radiative carrier recombination during device operation. The effect of shell engineering was investigated on the charge carrier dynamic and PEC performance. The PEC device based on $CZISe_2$/ZSeS QDs exhibits an unprecedented photocurrent density of 11.80 mA/cm^2, which is 7% higher than bare $CZISe_2$ QDs. In addition, the long-term operational stability was enhanced by 10% compared to the reference $CZISe_2$ QDs based PEC device over 3600 s. The carrier dynamics and electronic band structure were studied to understand the enhancement of photocurrent density. The ZnSeS shell acts as an effective passivation layer that reduces carrier recombination, resulting in a higher charge injection rate at the QDs/TiO_2 and QDs/electrolyte interfaces. A record photocurrent density of 13.15 mA/cm^2 at 0.8 V vs RHE was achieved by incorporating MWCNTs into the above optimized $CZISe_2$/ZSeS QDs/TiO_2 photoanode. Furthermore, the 80% of initial photocurrent retention demonstrates the excellent long-term stability of this PEC device.

In chapter four, a synergistic approach was adopted to modulate the optical properties of $ZnInSe_2$/ZnSe core/shell QDs by Cu doping inside the core and Mn alloying into the shell. The engineered Cu:$ZnInSe_2$/Mn:ZnSe QDs were integrated with PMMA polymer to use as luminescent security inks for anti-counterfeiting applications. Based on PL-related studies, the findings indicate that Cu doping within the $ZnInSe_2$ efficiently captures holes, while Mn alloying in the ZnSe shell provides mid-gap states for electron relaxation. This dual doping strategy

significantly prolonged the PL lifetime (201 ns) and improved PL emission intensity compared to undoped and singly doped QDs. Despite the presence of two optically active dopants (Cu and Mn), the Cu dopant emission is predominant in the Cu:$ZnInSe_2$/Mn:ZnSe due to the narrow band gap of host material as confirmed by PL spectra. The Cu and Mn dopants modulated core/shell QDs could produce huge coding capacity and realize complex information encryption. The anti-counterfeit characteristics of the printed patterns remained intact even after direct water soaking for a prolonged period of 10 weeks. Furthermore, they exhibited superior thermal stability, retaining 70% of the PL intensity at 170°C. These results indicate that synergistic manipulation of Cu and Mn dopants in heavy-metal-free core/shell QDs shows promising potential to realize highly stable luminescent inks for anti-counterfeiting applications.

The work presented in this thesis provides an effective strategy for developing highly stable, environmentally friendly QDs aimed at enhancing the performance of PEC devices and anti-counterfeiting technologies. Our findings offer valuable insights into improving the stability and performance of ternary and multinary QDs by precisely tailoring their band structure, making them highly effective for solar energy conversion applications (i.e. solar cells and photodetectors).

Scalability and Compatibility with Industrial Production:

Although QDs are available as products in the market, they remain expensive, with costs reaching up to ten thousand dollars per gram. This high cost limits their widespread application in areas such as anti-counterfeiting and solar energy conversion technologies. To overcome this barrier, low-cost and large-scale production methods must be developed. The currently employed hot-injection method in my study presents challenges for scaling up, including maintaining precise temperature control and ensuring consistent production of uniform QDs with desirable properties in scaled batch-synthesis. However, combining hot-injection protocols with continuous flow synthesis offers a potential solution to these issues.

The synthesis process utilizes eco-friendly precursors such as zinc (Zn), indium (In), and selenium (Se), which reduces reliance on toxic or rare materials like cadmium or lead. Automation and real-time monitoring could further enhance the scalability of the synthesis process without compromising the quality of the QDs. Such advancements make QD production more viable for industrial applications and align with industrial trends toward green manufacturing. The industrial compatibility of QDs depends on cost-effectiveness,

environmental sustainability, and material stability. For anti-counterfeiting devices, manufacturing processes need to advance beyond lab-scale methods like inkjet printing and roll-to-roll techniques. In parallel, at the device level, it is essential to evaluate performance metrics under conditions relevant to the final application. The standardized stress tests and material degradation studies are necessary to improve the reliability and durability of QD-based devices. The release of QDs to environment can occur during synthesis and end-product manufacturing. An accurate evaluation of impact on environment should be assessed, and similarly, exposure from environment to human health as well. These assessments validate the applicability of QDs in large-scale applications.

Furthermore, our research establishes a robust platform for utilizing transition metal ion dopants, paving the way for the emergence of more heavy-metal-free QDs with advanced security features. These advancements promise to contribute significantly to the fields of renewable energy and security technologies. Future research direction could focus on exploiting Machine-learning (MI) based prediction models to select and optimize suitable ligands and metal precursors for quantum dots sizing as required for application. MI integrated with experimental data provide critical guidance and strategies for exploring the synthetic parameters to construct advanced QDs with multi-shell structures and shape tunable architectures, optimizing their optical and electrical properties for energy conversion and optoelectronic applications.

REFERENCES

[1] S. Shishodia, B. Chouchene, T. Gries, R. Schneider, Selected I-III-VI2 Semiconductors: Synthesis, Properties and Applications in Photovoltaic Cells, Nanomaterials, 13 (2023) 2889.

[2] U. Banin, Y. Cao, D. Katz, O. Millo, Identification of atomic-like electronic states in indium arsenide nanocrystal quantum dots, Nature, 400 (1999) 542-544.

[3] R. Ashoori, Electrons in artificial atoms, Nature, 379 (1996) 413-419.

[4] A.C. Berends, C. de Mello Donega, Ultrathin one-and two-dimensional colloidal semiconductor nanocrystals: pushing quantum confinement to the limit, The journal of physical chemistry letters, 8 (2017) 4077-4090.

[5] L. Brus, Electronic wave functions in semiconductor clusters: experiment and theory, The Journal of Physical Chemistry, 90 (1986) 2555-2560.

[6] F.P. García de Arquer, D.V. Talapin, V.I. Klimov, Y. Arakawa, M. Bayer, E.H. Sargent, Semiconductor quantum dots: Technological progress and future challenges, Science, 373 (2021) eaaz8541.

[7] M. Steigerwald, A. Alivisatos, J. Gibson, T. Harris, R. Kortan, A. Muller, A. Thayer, T. Duncan, Douglass DC and Brus LE, J. Am. Chem. Soc., 1988 (1988) 110.

[8] J.G. Brennan, T. Siegrist, P. Carroll, S. Stuczynski, L. Brus, M. Steigerwald, The preparation of large semiconductor clusters via the pyrolysis of a molecular precursor, Journal of the American Chemical Society, 111 (1989) 4141-4143.

[9] C. Murray, D.J. Norris, M.G. Bawendi, Synthesis and characterization of nearly monodisperse CdE (E= sulfur, selenium, tellurium) semiconductor nanocrystallites, Journal of the American Chemical Society, 115 (1993) 8706-8715.

[10] K. Yu, K.S. Schanze, Commemorating the Nobel Prize in Chemistry 2023 for the discovery and synthesis of quantum dots, in, ACS Publications, 2023, pp. 1989-1992.

[11] J.T.G. Overbeek, Monodisperse colloidal systems, fascinating and useful, Advances in Colloid and Interface Science, 15 (1982) 251-277.

[12] M. Faraday, X. The Bakerian Lecture.—Experimental relations of gold (and other metals) to light, Philosophical transactions of the Royal Society of London, (1857) 145-181.

[13] S. Kumar, T. Nann, Shape control of II–VI semiconductor nanomaterials, Small, 2 (2006) 316-329.

[14] C. Burda, X. Chen, R. Narayanan, M.A. El-Sayed, Chemistry and properties of nanocrystals of different shapes, Chemical reviews, 105 (2005) 1025-1102.

[15] H. Reiss, The growth of uniform colloidal dispersions, The Journal of Chemical Physics, 19 (1951) 482-487.

[16] D.V. Talapin, A.L. Rogach, M. Haase, H. Weller, Evolution of an ensemble of nanoparticles in a colloidal solution: theoretical study, The Journal of Physical Chemistry B, 105 (2001) 12278-12285.

[17] Y. De Smet, L. Deriemaeker, R. Finsy, A simple computer simulation of Ostwald ripening, Langmuir, 13 (1997) 6884-6888.

[18] K. Cheng, X. Han, J. Meng, S. Wang, Z. Du, A composition-tunable Zn x Cd 1− x Se/ZnO core–shell nanowire array: mechanisms for the enhanced charge separation and its photovoltaic applications, RSC Advances, 5 (2015) 11084-11090.

[19] C.B. Murray, C.R. Kagan, M.G. Bawendi, Synthesis and characterization of monodisperse nanocrystals and close-packed nanocrystal assemblies, Annual review of materials science, 30 (2000) 545-610.

[20] G.S. Selopal, H. Zhao, Z.M. Wang, F. Rosei, Core/shell quantum dots solar cells, Advanced Functional Materials, 30 (2020) 1908762.

[21] P. Reiss, M. Protiere, L. Li, Core/shell semiconductor nanocrystals, small, 5 (2009) 154-168.

[22] Y.C. Cao, J. Wang, One-pot synthesis of high-quality zinc-blende CdS nanocrystals, Journal of the American Chemical Society, 126 (2004) 14336-14337.

[23] H. Wang, I. Barceló, T. Lana-Villarreal, R. Gómez, M. Bonn, E. Cánovas, Interplay between structure, stoichiometry, and electron transfer dynamics in SILAR-based quantum dot-sensitized oxides, Nano letters, 14 (2014) 5780-5786.

[24] N. Guijarro, T. Lana-Villarreal, T. Lutz, S.A. Haque, R. Gomez, Sensitization of TiO2 with PbSe quantum dots by SILAR: how mercaptophenol improves charge separation, The Journal of Physical Chemistry Letters, 3 (2012) 3367-3372.

[25] J.H. Bang, P.V. Kamat, Quantum dot sensitized solar cells. A tale of two semiconductor nanocrystals: CdSe and CdTe, ACS nano, 3 (2009) 1467-1476.

[26] P. Cozzoli, L. Manna, Nature Mater., 2005, 4, 801;(c) M. Casavola, R. Buonsanti, G. Caputo and PD Cozzoli, Eur. J. Inorg. Chem, 6 (2008) 55.

[27] P.D. Cozzoli, T. Pellegrino, L. Manna, Synthesis, properties and perspectives of hybrid nanocrystal structures, Chemical Society Reviews, 35 (2006) 1195-1208.

[28] M.A. Hines, G.D. Scholes, Colloidal PbS nanocrystals with size-tunable near-infrared emission: observation of post-synthesis self-narrowing of the particle size distribution, Advanced materials, 15 (2003) 1844-1849.

[29] A.L. Rogach, A. Eychmüller, S.G. Hickey, S.V. Kershaw, Infrared-emitting colloidal nanocrystals: synthesis, assembly, spectroscopy, and applications, small, 3 (2007) 536-557.

[30] I. Moreels, K. Lambert, D. Smeets, D. De Muynck, T. Nollet, J.C. Martins, F. Vanhaecke, A. Vantomme, C. Delerue, G. Allan, Size-dependent optical properties of colloidal PbS quantum dots, ACS nano, 3 (2009) 3023-3030.

[31] A.L. Rogach, D.V. Talapin, E.V. Shevchenko, A. Kornowski, M. Haase, H. Weller, Organization of matter on different size scales: monodisperse nanocrystals and their superstructures, Advanced Functional Materials, 12 (2002) 653-664.

[32] K.-S. Cho, D.V. Talapin, W. Gaschler, C.B. Murray, Designing PbSe nanowires and nanorings through oriented attachment of nanoparticles, Journal of the American Chemical Society, 127 (2005) 7140-7147.

[33] L. Manna, D.J. Milliron, A. Meisel, E.C. Scher, A.P. Alivisatos, Controlled growth of tetrapod-branched inorganic nanocrystals, Nature materials, 2 (2003) 382-385.

[34] G. Tan, J. Du, Q. Zhang, Structural evolution and optical properties of CdSe nanocrystals prepared by mechanical alloying, Journal of Alloys and Compounds, 468 (2009) 421-431.

[35] Y. Chen, Y. Jiang, Z. Zhang, C. Wang, X. Liu, Synthesis spectrum properties of high-quality CdS quantum dots, Journal of Nanoscience and Nanotechnology, 10 (2010) 6544-6549.

[36] T. Kim, Y.K. Jung, J.-K. Lee, The formation mechanism of CdSe QDs through the thermolysis of Cd (oleate) 2 and TOPSe in the presence of alkylamine, Journal of Materials Chemistry C, 2 (2014) 5593-5600.

[37] Y.-w. Jun, S.-M. Lee, N.-J. Kang, J. Cheon, Controlled synthesis of multi-armed CdS nanorod architectures using monosurfactant system, Journal of the American Chemical Society, 123 (2001) 5150-5151.

[38] K. Subila, G. Kishore Kumar, S. Shivaprasad, K. George Thomas, Luminescence properties of CdSe quantum dots: role of crystal structure and surface composition, The Journal of Physical Chemistry Letters, 4 (2013) 2774-2779.

[39] M.C. Weidman, M.E. Beck, R.S. Hoffman, F. Prins, W.A. Tisdale, Monodisperse, air-stable PbS nanocrystals via precursor stoichiometry control, ACS nano, 8 (2014) 6363-6371.

[40] J.M. Pietryga, R.D. Schaller, D. Werder, M.H. Stewart, V.I. Klimov, J.A. Hollingsworth, Pushing the band gap envelope: mid-infrared emitting colloidal PbSe quantum dots, Journal of the American Chemical Society, 126 (2004) 11752-11753.

[41] J. Zhang, J. Gao, E.M. Miller, J.M. Luther, M.C. Beard, Diffusion-controlled synthesis of PbS and PbSe quantum dots with in situ halide passivation for quantum dot solar cells, ACS nano, 8 (2014) 614-622.

[42] W.K. Bae, J. Joo, L.A. Padilha, J. Won, D.C. Lee, Q. Lin, W.-k. Koh, H. Luo, V.I. Klimov, J.M. Pietryga, Highly effective surface passivation of PbSe quantum dots through reaction with molecular chlorine, Journal of the American Chemical Society, 134 (2012) 20160-20168.

[43] Y. Pan, M.A. Sohel, L. Pan, Z. Wei, H. Bai, M.C. Tamargo, R. John, Synthesis of Air-stable PbSe Quantum Dots Using PbCl2-oleylamine System, Materials Today: Proceedings, 2 (2015) 281-286.

[44] K.A. Abel, J. Shan, J.-C. Boyer, F. Harris, F.C. van Veggel, Highly photoluminescent PbS nanocrystals: the beneficial effect of trioctylphosphine, Chemistry of Materials, 20 (2008) 3794-3796.

[45] D. Franke, D.K. Harris, L. Xie, K.F. Jensen, M.G. Bawendi, The unexpected influence of precursor conversion rate in the synthesis of III–V quantum dots, Angewandte Chemie, 127 (2015) 14507-14511.

[46] V. Srivastava, E. Dunietz, V. Kamysbayev, J.S. Anderson, D.V. Talapin, Monodisperse InAs quantum dots from aminoarsine precursors: understanding the role of reducing agent, Chemistry of Materials, 30 (2018) 3623-3627.

[47] Q. Zhao, H.J. Kulik, Electronic structure origins of surface-dependent growth in III–V quantum dots, Chemistry of Materials, 30 (2018) 7154-7165.

[48] D.K. Harris, M.G. Bawendi, Improved precursor chemistry for the synthesis of III–V quantum dots, Journal of the American Chemical Society, 134 (2012) 20211-20213.

[49] D. Franke, D.K. Harris, O. Chen, O.T. Bruns, J.A. Carr, M.W. Wilson, M.G. Bawendi, Continuous injection synthesis of indium arsenide quantum dots emissive in the short-wavelength infrared, Nature communications, 7 (2016) 12749.

[50] T. Kim, S. Park, S. Jeong, Diffusion dynamics controlled colloidal synthesis of highly monodisperse InAs nanocrystals, Nature Communications, 12 (2021) 3013.

[51] R. Hu, F. He, R. Hou, Z. Wu, X. Zhang, H. Shen, The Narrow Synthetic Window for Highly Homogenous InP Quantum Dots toward Narrow Red Emission, Inorganic Chemistry, (2024).

[52] D.B. Berkinsky, A.H. Proppe, H. Utzat, C.J. Krajewska, W. Sun, T. Šverko, J.J. Yoo, H. Chung, Y.-H. Won, T. Kim, Narrow intrinsic line widths and electron–phonon coupling of InP colloidal quantum dots, ACS nano, 17 (2023) 3598-3609.

[53] J.F. Lox, Z. Dang, V.M. Dzhagan, D. Spittel, B. Martín-García, I. Moreels, D.R. Zahn, V. Lesnyak, Near-infrared Cu–In–Se-based colloidal nanocrystals via cation exchange, Chemistry of Materials, 30 (2018) 2607-2617.

[54] X. Dong, J. Xu, X. Zhang, S. Shi, H. Yang, Z. Mo, L. Li, S. Yin, Investigating photoluminescence mechanism of Cu-doped Zn–In–Se quantum dots by Zn/in ratio, The Journal of Physical Chemistry C, 121 (2017) 16978-16984.

[55] S. Cao, W. Ji, J. Zhao, W. Yang, C. Li, J. Zheng, Color-tunable photoluminescence of Cu-doped Zn–In–Se quantum dots and their electroluminescence properties, Journal of Materials Chemistry C, 4 (2016) 581-588.

[56] J. Du, Z. Du, J.-S. Hu, Z. Pan, Q. Shen, J. Sun, D. Long, H. Dong, L. Sun, X. Zhong, Zn–Cu–In–Se quantum dot solar cells with a certified power conversion efficiency of 11.6%, Journal of the American Chemical Society, 138 (2016) 4201-4209.

[57] T. Chevallier, A. Benayad, G. Le Blevennec, F. Chandezon, Method to determine radiative and non-radiative defects applied to AgInS 2–ZnS luminescent nanocrystals, Physical Chemistry Chemical Physics, 19 (2017) 2359-2363.

[58] G. Dagan, F. Abou-Elfotouh, D. Dunlavy, R. Matson, D. Cahen, Defect level identification in copper indium selenide (CuInSe2) from photoluminescence studies, Chemistry of Materials, 2 (1990) 286-293.

[59] C.-H.M. Chuang, A. Maurano, R.E. Brandt, G.W. Hwang, J. Jean, T. Buonassisi, V. Bulovic, M.G. Bawendi, Open-circuit voltage deficit, radiative sub-bandgap states, and prospects in quantum dot solar cells, Nano letters, 15 (2015) 3286-3294.

[60] P.M. Allen, M.G. Bawendi, Ternary I− III− VI quantum dots luminescent in the red to near-infrared, Journal of the American Chemical Society, 130 (2008) 9240-9241.

[61] M.A. Malik, P. O'Brien, N. Revaprasadu, A novel route for the preparation of CuSe and CuInSe2 nanoparticles, Advanced Materials, 11 (1999) 1441-1444.

[62] A. Dutta, R.K. Behera, P. Pal, S. Baitalik, N. Pradhan, Near‐unity photoluminescence quantum efficiency for all CsPbX3 (X= Cl, Br, and I) perovskite nanocrystals: a generic synthesis approach, Angewandte Chemie International Edition, 58 (2019) 5552-5556.

[63] Y. Tong, E. Bladt, M.F. Aygüler, A. Manzi, K.Z. Milowska, V.A. Hintermayr, P. Docampo, S. Bals, A.S. Urban, L. Polavarapu, Highly luminescent cesium lead halide perovskite nanocrystals with tunable composition and thickness by ultrasonication, Angewandte Chemie International Edition, 55 (2016) 13887-13892.

[64] T. Liu, C. Yang, Z. Fan, X. Chen, Z. Chen, Y. Su, H. Zhu, F. Sun, T. Jiang, W. Zhu, Spectral narrowing and enhancement of directional emission of perovskite light emitting diode by microcavity, Laser & Photonics Reviews, 16 (2022) 2200091.

[65] S. Wang, S. Feng, R. Li, J. Jin, J. Wu, W. Zheng, Z. Xia, X. Chen, Q. Ling, Z. Lin, Multiexciton Generation from a 2D Organic–Inorganic Hybrid Perovskite with Nearly 200% Quantum Yield of Red Phosphorescence, Advanced Materials, 35 (2023) 2211992.

[66] X. Zhang, B. Lin, F. Wang, Z. Cheng, X. Shi, B.G. Lougou, Design of biomimetic leaf-type hierarchical nanostructure for enhancing the solar energy harvesting of ultra-thin perovskite solar cells, ES Energy & Environment, 10 (2020) 22-33.

[67] G. Pacchioni, Highly efficient perovskite LEDs, Nature Reviews Materials, 6 (2021) 108-108.

[68] J. Fan, W. Li, Q. Zhou, G. Yang, P. Tang, J. He, L. Ma, J. Zhang, J. Xiao, Z. Yan, Metal Halide Perovskites for Direct X-Ray Detection in Medical Imaging: To Higher Performance, Advanced Functional Materials, (2024) 2401017.

[69] J.-P. Correa-Baena, M. Saliba, T. Buonassisi, M. Grätzel, A. Abate, W. Tress, A. Hagfeldt, Promises and challenges of perovskite solar cells, Science, 358 (2017) 739-744.

[70] Z. Li, M. Yang, J.-S. Park, S.-H. Wei, J.J. Berry, K. Zhu, Stabilizing perovskite structures by tuning tolerance factor: formation of formamidinium and cesium lead iodide solid-state alloys, Chemistry of Materials, 28 (2016) 284-292.

[71] A.A. Brown, P. Vashishtha, T.J. Hooper, Y.F. Ng, G.V. Nutan, Y. Fang, D. Giovanni, J.N. Tey, L. Jiang, B. Damodaran, Precise control of CsPbBr3 perovskite nanocrystal growth at room temperature: size tunability and synthetic insights, Chemistry of Materials, 33 (2021) 2387-2397.

[72] X. Sheng, G. Chen, C. Wang, W. Wang, J. Hui, Q. Zhang, K. Yu, W. Wei, M. Yi, M. Zhang, Polarized optoelectronics of CsPbX3 (X= Cl, Br, I) perovskite nanoplates with tunable size and thickness, Advanced Functional Materials, 28 (2018) 1800283.

[73] H. Diab, G. Trippé-Allard, F. Lédée, K. Jemli, C. Vilar, G. Bouchez, V.L. Jacques, A. Tejeda, J. Even, J.-S. Lauret, Narrow linewidth excitonic emission in organic–inorganic lead iodide perovskite single crystals, The journal of physical chemistry letters, 7 (2016) 5093-5100.

[74] D. Xu, Q. Wan, S. Wu, Y. Zhao, X. Xu, L. Li, G. He, Enhancing the performance of LARP-synthesized CsPbBr 3 nanocrystal LEDs by employing a dual hole injection layer, RSC advances, 10 (2020) 17653-17659.

[75] S. Miyata, Y. Iso, T. Isobe, Investigation on photoluminescence of CsPb (Br, I) 3 perovskite nanocrystals by comparison between hot-injection and ion-exchange methods, ECS Journal of Solid State Science and Technology, 10 (2021) 096003.

[76] L. Zhang, H. Zhou, Y. Chen, Z. Zheng, L. Huang, C. Wang, K. Dong, Z. Hu, W. Ke, G. Fang, Spontaneous crystallization of strongly confined CsSnxPb1-xI3 perovskite colloidal quantum dots at room temperature, Nature Communications, 15 (2024) 1609.

[77] Z. Chen, Y. Hu, J. Wang, Q. Shen, Y. Zhang, C. Ding, Y. Bai, G. Jiang, Z. Li, N. Gaponik, Boosting photocatalytic CO2 reduction on CsPbBr3 perovskite nanocrystals by immobilizing metal complexes, Chemistry of Materials, 32 (2020) 1517-1525.

[78] M. Grabolle, J. Ziegler, A. Merkulov, T. Nann, U. Resch-Genger, Stability and fluorescence quantum yield of CdSe–ZnS quantum dots—influence of the thickness of the ZnS shell, Annals of the New York Academy of Sciences, 1130 (2008) 235-241.

[79] H. Zhu, N. Song, T. Lian, Controlling charge separation and recombination rates in CdSe/ZnS type I core− shell quantum dots by shell thicknesses, Journal of the American Chemical Society, 132 (2010) 15038-15045.

[80] H. Zhang, L.V. Besteiro, J. Liu, C. Wang, G.S. Selopal, Z. Chen, D. Barba, Z.M. Wang, H. Zhao, G.P. Lopinski, Efficient and stable photoelectrochemical hydrogen generation using optimized colloidal heterostructured quantum dots, Nano Energy, 79 (2021) 105416.

[81] Z. Pan, H. Zhang, K. Cheng, Y. Hou, J. Hua, X. Zhong, Highly efficient inverted type-I CdS/CdSe core/shell structure QD-sensitized solar cells, ACS nano, 6 (2012) 3982-3991.

[82] Z.-J. Li, X.-B. Fan, X.-B. Li, J.-X. Li, F. Zhan, Y. Tao, X. Zhang, Q.-Y. Kong, N.-J. Zhao, J.-P. Zhang, Direct synthesis of all-inorganic heterostructured CdSe/CdS QDs in aqueous solution for improved photocatalytic hydrogen generation, Journal of Materials Chemistry A, 5 (2017) 10365-10373.

[83] L. Balet, S.A. Ivanov, A. Piryatinski, M. Achermann, V.I. Klimov, Inverted core/shell nanocrystals continuously tunable between type-I and type-II localization regimes, Nano Letters, 4 (2004) 1485-1488.

[84] S. Kim, B. Fisher, H.-J. Eisler, M. Bawendi, Type-II quantum dots: CdTe/CdSe (core/shell) and CdSe/ZnTe (core/shell) heterostructures, Journal of the American Chemical Society, 125 (2003) 11466-11467.

[85] H. Zhu, N. Song, W. Rodríguez-Córdoba, T. Lian, Wave function engineering for efficient extraction of up to nineteen electrons from one CdSe/CdS quasi-type II quantum dot, Journal of the American Chemical Society, 134 (2012) 4250-4257.

[86] J.M. Pietryga, D.J. Werder, D.J. Williams, J.L. Casson, R.D. Schaller, V.I. Klimov, J.A. Hollingsworth, Utilizing the lability of lead selenide to produce heterostructured nanocrystals with bright, stable infrared emission, Journal of the American Chemical Society, 130 (2008) 4879-4885.

[87] G. Zaiats, A. Shapiro, D. Yanover, Y. Kauffmann, A. Sashchiuk, E. Lifshitz, Optical and electronic properties of nonconcentric PbSe/CdSe colloidal quantum dots, The Journal of Physical Chemistry Letters, 6 (2015) 2444-2448.

[88] B. De Geyter, Y. Justo, I. Moreels, K. Lambert, P.F. Smet, D. Van Thourhout, A.J. Houtepen, D. Grodzinska, C. de Mello Donega, A. Meijerink, The different nature of band edge absorption and emission in colloidal PbSe/CdSe core/shell quantum dots, ACS nano, 5 (2011) 58-66.

[89] E. Lifshitz, M. Brumer, A. Kigel, A. Sashchiuk, M. Bashouti, M. Sirota, E. Galun, Z. Burshtein, A. Le Quang, I. Ledoux-Rak, Air-Stable PbSe/PbS and PbSe/PbSe x S1-x Core− Shell Nanocrystal Quantum Dots and Their Applications, The Journal of physical chemistry B, 110 (2006) 25356-25365.

[90] D. Yanover, R.K. Capek, A. Rubin-Brusilovski, R. Vaxenburg, N. Grumbach, G.I. Maikov, O. Solomeshch, A. Sashchiuk, E. Lifshitz, Small-sized PbSe/PbS core/shell colloidal quantum dots, Chemistry of Materials, 24 (2012) 4417-4423.

[91] C. de Mello Donegá, M. Bode, A. Meijerink, Size-and temperature-dependence of exciton lifetimes in CdSe quantum dots, Physical Review B—Condensed Matter and Materials Physics, 74 (2006) 085320.

[92] H. Zhao, G. Sirigu, A. Parisini, A. Camellini, G. Nicotra, F. Rosei, V. Morandi, M. Zavelani-Rossi, A. Vomiero, Dual emission in asymmetric “giant” PbS/CdS/CdS core/shell/shell quantum dots, Nanoscale, 8 (2016) 4217-4226.

[93] P. Reiss, J. Bleuse, A. Pron, Highly luminescent CdSe/ZnSe core/shell nanocrystals of low size dispersion, Nano letters, 2 (2002) 781-784.

[94] G. Zaiats, D. Yanover, R. Vaxenburg, J. Tilchin, A. Sashchiuk, E. Lifshitz, PbSe-based colloidal core/shell heterostructures for optoelectronic applications, Materials, 7 (2014) 7243-7275.

[95] W.K. Bae, L.A. Padilha, Y.-S. Park, H. McDaniel, I. Robel, J.M. Pietryga, V.I. Klimov, Controlled alloying of the core–shell interface in CdSe/CdS quantum dots for suppression of Auger recombination, ACS nano, 7 (2013) 3411-3419.

[96] D.V. Talapin, I. Mekis, S. Götzinger, A. Kornowski, O. Benson, H. Weller, CdSe/CdS/ZnS and CdSe/ZnSe/ZnS Core− Shell− Shell Nanocrystals, The Journal of Physical Chemistry B, 108 (2004) 18826-18831.

[97] J. McBride, J. Treadway, L. Feldman, S.J. Pennycook, S.J. Rosenthal, Structural basis for near unity quantum yield core/shell nanostructures, Nano Letters, 6 (2006) 1496-1501.

[98] R. Xie, U. Kolb, J. Li, T. Basché, A. Mews, Synthesis and characterization of highly luminescent CdSe− Core CdS/Zn0. 5Cd0. 5S/ZnS multishell nanocrystals, Journal of the American Chemical Society, 127 (2005) 7480-7488.

[99] A. Aharoni, T. Mokari, I. Popov, U. Banin, Synthesis of InAs/CdSe/ZnSe core/shell1/shell2 structures with bright and stable near-infrared fluorescence, Journal of the American Chemical Society, 128 (2006) 257-264.

[100] V.A. Vlaskin, N. Janssen, J. van Rijssel, R. Beaulac, D.R. Gamelin, Tunable dual emission in doped semiconductor nanocrystals, Nano letters, 10 (2010) 3670-3674.

[101] C. Wang, Z. Hu, S. Xu, Y. Wang, Z. Zhao, Z. Wang, Y. Cui, Tuning the emission of aqueous Cu: ZnSe quantum dots to yellow light window, Nanotechnology, 26 (2015) 305601.

[102] J.-Y. Kim, Y.J. Jang, J. Park, J. Kim, J.S. Kang, D.Y. Chung, Y.-E. Sung, C. Lee, J.S. Lee, M.J. Ko, Highly loaded PbS/Mn-doped CdS quantum dots for dual application in solar-to-electrical and solar-to-chemical energy conversion, Applied Catalysis B: Environmental, 227 (2018) 409-417.

[103] N.S. Karan, D. Sarma, R. Kadam, N. Pradhan, Doping transition metal (Mn or Cu) ions in semiconductor nanocrystals, The Journal of Physical Chemistry Letters, 1 (2010) 2863-2866.

[104] N. Pradhan, D. Goorskey, J. Thessing, X. Peng, An alternative of CdSe nanocrystal emitters: pure and tunable impurity emissions in ZnSe nanocrystals, Journal of the American Chemical Society, 127 (2005) 17586-17587.

[105] N. Pradhan, Mn-doped semiconductor nanocrystals: 25 years and beyond, in, ACS Publications, 2019, pp. 2574-2577.

[106] R. Bhargava, D. Gallagher, X. Hong, A. Nurmikko, Optical properties of manganese-doped nanocrystals of ZnS, Physical Review Letters, 72 (1994) 416.

[107] W. Liu, Q. Lin, H. Li, K. Wu, I. Robel, J.M. Pietryga, V.I. Klimov, Mn2+-doped lead halide perovskite nanocrystals with dual-color emission controlled by halide content, Journal of the American Chemical Society, 138 (2016) 14954-14961.

[108] S. Das Adhikari, A. Dutta, S.K. Dutta, N. Pradhan, Layered perovskites L2 (Pb1–x Mn x) Cl4 to Mn-doped CsPbCl3 perovskite platelets, ACS Energy Letters, 3 (2018) 1247-1253.

[109] W.J. Mir, M. Jagadeeswararao, S. Das, A. Nag, Colloidal Mn-doped cesium lead halide perovskite nanoplatelets, ACS Energy Letters, 2 (2017) 537-543.

[110] D.J. Norris, N. Yao, F.T. Charnock, T.A. Kennedy, High-quality manganese-doped ZnSe nanocrystals, Nano Letters, 1 (2001) 3-7.

[111] S. Acharya, N. Pradhan, Insertion/ejection of dopant ions in composition tunable semiconductor nanocrystals, The Journal of Physical Chemistry C, 115 (2011) 19513-19519.

[112] R. Beaulac, P.I. Archer, X. Liu, S. Lee, G.M. Salley, M. Dobrowolska, J.K. Furdyna, D.R. Gamelin, Spin-polarizable excitonic luminescence in colloidal Mn2+-doped CdSe quantum dots, Nano letters, 8 (2008) 1197-1201.

[113] G. Manna, S. Jana, R. Bose, N. Pradhan, Mn-doped multinary CIZS and AIZS nanocrystals, The journal of physical chemistry letters, 3 (2012) 2528-2534.

[114] R. Thakar, Y. Chen, P.T. Snee, Efficient emission from core/(doped) shell nanoparticles: applications for chemical sensing, Nano letters, 7 (2007) 3429-3432.

[115] P.K. Santra, P.V. Kamat, Mn-doped quantum dot sensitized solar cells: a strategy to boost efficiency over 5%, Journal of the American Chemical Society, 134 (2012) 2508-2511.

[116] S. Sarkar, R. Bose, S. Jana, N.R. Jana, N. Pradhan, Doped semiconductor nanocrystals and organic dyes: an efficient and greener FRET system, The Journal of Physical Chemistry Letters, 1 (2010) 636-640.

[117] C.S. Erickson, L.R. Bradshaw, S. McDowall, J.D. Gilbertson, D.R. Gamelin, D.L. Patrick, Zero-reabsorption doped-nanocrystal luminescent solar concentrators, ACS nano, 8 (2014) 3461-3467.

[118] Y. Dong, J. Choi, H.-K. Jeong, D.H. Son, Hot electrons generated from doped quantum dots via upconversion of excitons to hot charge carriers for enhanced photocatalysis, Journal of the American Chemical Society, 137 (2015) 5549-5554.

[119] S. Maiti, J. Dana, Y. Jadhav, T. Debnath, S.K. Haram, H.N. Ghosh, Electrochemical evaluation of dopant energetics and the modulation of ultrafast carrier dynamics in Cu-doped CdSe nanocrystals, The Journal of Physical Chemistry C, 121 (2017) 27233-27240.

[120] R. Xie, X. Peng, Synthesis of Cu-doped InP nanocrystals (d-dots) with ZnSe diffusion barrier as efficient and color-tunable NIR emitters, Journal of the American Chemical Society, 131 (2009) 10645-10651.

[121] J.T. Wright, K. Forsythe, J. Hutchins, R.W. Meulenberg, Implications of orbital hybridization on the electronic properties of doped quantum dots: the case of Cu: CdSe, Nanoscale, 8 (2016) 9417-9424.

[122] W. Zhang, Q. Lou, W. Ji, J. Zhao, X. Zhong, Color-tunable highly bright photoluminescence of cadmium-free Cu-doped Zn–In–S nanocrystals and electroluminescence, Chemistry of Materials, 26 (2014) 1204-1212.

[123] L. Xia, X. Tong, Y. Yao, Z. Long, M. Cai, L. Jin, A. Vomiero, Z.M. Wang, Simultaneous copper incorporation in core/shell-structured eco-friendly quantum dots for high-efficiency photoelectrochemical hydrogen evolution, Nano Energy, 122 (2024) 109302.

[124] A.A. Bol, R. van Beek, A. Meijerink, On the incorporation of trivalent rare earth ions in II− VI semiconductor nanocrystals, Chemistry of materials, 14 (2002) 1121-1126.

[125] B. Cheng, Z. Wang, Synthesis and optical properties of europium-doped ZnS: long-lasting phosphorescence from aligned nanowires, Advanced Functional Materials, 15 (2005) 1883-1890.

[126] A. Vilanova, T. Lopes, A. Mendes, Large-area photoelectrochemical water splitting using a multi-photoelectrode approach, Journal of Power Sources, 398 (2018) 224-232.

[127] T. Yao, X. An, H. Han, J.Q. Chen, C. Li, Photoelectrocatalytic materials for solar water splitting, Advanced Energy Materials, 8 (2018) 1800210.

[128] Z. Zhang, J.T. Yates Jr, Band bending in semiconductors: chemical and physical consequences at surfaces and interfaces, Chemical reviews, 112 (2012) 5520-5551.

[129] A.G. Pattantyus-Abraham, I.J. Kramer, A.R. Barkhouse, X. Wang, G. Konstantatos, R. Debnath, L. Levina, I. Raabe, M.K. Nazeeruddin, M. Gratzel, Depleted-heterojunction colloidal quantum dot solar cells, ACS nano, 4 (2010) 3374-3380.

[130] A.J. Cowan, J.R. Durrant, Long-lived charge separated states in nanostructured semiconductor photoelectrodes for the production of solar fuels, Chemical Society Reviews, 42 (2013) 2281-2293.

[131] A. Fujishima, K. Honda, Electrochemical photolysis of water at a semiconductor electrode, nature, 238 (1972) 37-38.

[132] J.N. Tiwari, A.N. Singh, S. Sultan, K.S. Kim, Recent advancement of p-and d-block elements, single atoms, and graphene-based photoelectrochemical electrodes for water splitting, Advanced Energy Materials, 10 (2020) 2000280.

[133] C. Wang, S. Cao, W.-F. Fu, A stable dual-functional system of visible-light-driven Ni (II) reduction to a nickel nanoparticle catalyst and robust in situ hydrogen production, Chemical Communications, 49 (2013) 11251-11253.

[134] Z. Chen, Y. Bu, L. Wang, X. Wang, J.-P. Ao, Single-sites Rh-phosphide modified carbon nitride photocatalyst for boosting hydrogen evolution under visible light, Applied Catalysis B: Environmental, 274 (2020) 119117.

[135] Y. Yu, Z. Zhang, X. Yin, A. Kvit, Q. Liao, Z. Kang, X. Yan, Y. Zhang, X. Wang, Enhanced photoelectrochemical efficiency and stability using a conformal TiO2 film on a black silicon photoanode, Nature Energy, 2 (2017) 1-7.

[136] A.J. Bard, M.A. Fox, Artificial photosynthesis: solar splitting of water to hydrogen and oxygen, Accounts of Chemical Research, 28 (1995) 141-145.

[137] F. Niu, D. Wang, F. Li, Y. Liu, S. Shen, T.J. Meyer, Hybrid photoelectrochemical water splitting systems: from interface design to system assembly, Advanced Energy Materials, 10 (2020) 1900399.

[138] L. Jin, H. Zhao, Z.M. Wang, F. Rosei, Quantum dots-based photoelectrochemical hydrogen evolution from water splitting, Advanced Energy Materials, 11 (2021) 2003233.

[139] F. Li, K. Fan, B. Xu, E. Gabrielsson, Q. Daniel, L. Li, L. Sun, Organic dye-sensitized tandem photoelectrochemical cell for light driven total water splitting, Journal of the American Chemical Society, 137 (2015) 9153-9159.

[140] H.M. Chen, C.K. Chen, Y.C. Chang, C.W. Tsai, R.S. Liu, S.F. Hu, W.S. Chang, K.H. Chen, Quantum dot monolayer sensitized ZnO nanowire-array photoelectrodes: true efficiency for water splitting, Angewandte Chemie International Edition, 34 (2010) 5966-5969.

[141] T.P. Yoon, M.A. Ischay, J. Du, Visible light photocatalysis as a greener approach to photochemical synthesis, Nature chemistry, 2 (2010) 527-532.

[142] J. Liu, H. Zhang, F. Navarro-Pardo, G.S. Selopal, S. Sun, Z.M. Wang, H. Zhao, F. Rosei, Hybrid surface passivation of PbS/CdS quantum dots for efficient photoelectrochemical hydrogen generation, Applied Surface Science, 530 (2020) 147252.

[143] Y. Jin-nouchi, T. Hattori, Y. Sumida, M. Fujishima, H. Tada, PbS quantum dot-sensitized photoelectrochemical cell for hydrogen production from water under illumination of simulated sunlight, ChemPhysChem, 11 (2010) 3592-3595.

[144] M. Seol, H. Kim, W. Kim, K. Yong, Highly efficient photoelectrochemical hydrogen generation using a ZnO nanowire array and a CdSe/CdS co-sensitizer, Electrochemistry communications, 12 (2010) 1416-1418.

[145] L. Jin, B. AlOtaibi, D. Benetti, S. Li, H. Zhao, Z. Mi, A. Vomiero, F. Rosei, Near-infrared colloidal quantum dots for efficient and durable photoelectrochemical solar-driven hydrogen production, Advanced Science, 3 (2016).

[146] Y. Chen, J. Vela, H. Htoon, J.L. Casson, D.J. Werder, D.A. Bussian, V.I. Klimov, J.A. Hollingsworth, “Giant” multishell CdSe nanocrystal quantum dots with suppressed blinking, Journal of the American Chemical Society, 130 (2008) 5026-5027.

[147] G. Ai, R. Mo, H. Xu, Q. Chen, S. Yang, H. Li, J. Zhong, Vertically aligned TiO2/(CdS, CdTe, CdSTe) core/shell nanowire array for photoelectrochemical hydrogen generation, Journal of Power Sources, 280 (2015) 5-11.

[148] X. Zhan, Q. Wang, F. Wang, Y. Wang, Z. Wang, J. Cao, M. Safdar, J. He, Composition-Tuned ZnO/Zn x Cd1–x Te Core/Shell Nanowires Array with Broad Spectral Absorption from UV to NIR for Hydrogen Generation, ACS applied materials & interfaces, 6 (2014) 2878-2883.

[149] H. Zhao, J. Liu, F. Vidal, A. Vomiero, F. Rosei, Tailoring the interfacial structure of colloidal “giant” quantum dots for optoelectronic applications, Nanoscale, 10 (2018) 17189-17197.

[150] C. Gao, T. Wei, Y. Zhang, X. Song, Y. Huan, H. Liu, M. Zhao, J. Yu, X. Chen, A photoresponsive rutile TiO2 heterojunction with enhanced Electron–Hole separation for high-performance hydrogen evolution, Advanced materials, 31 (2019) 1806596.

[151] R. Trevisan, P. Rodenas, V. Gonzalez-Pedro, C. Sima, R.S. Sanchez, E.M. Barea, I. Mora-Sero, F. Fabregat-Santiago, S. Gimenez, Harnessing infrared photons for photoelectrochemical hydrogen generation. A PbS quantum dot based “quasi-artificial leaf”, The journal of physical chemistry letters, 4 (2013) 141-146.

[152] R. Akilimali, G.S. Selopal, D. Benetti, M. Mohammadnezhad, H. Zhao, Z.M. Wang, B. Stansfield, F. Rosei, Graphene nanoribbon-TiO2-quantum dots hybrid photoanode to boost the performance of photoelectrochemical for hydrogen generation, Catalysis Today, 340 (2020) 161-169.

[153] G.S. Selopal, M. Mohammadnezhad, F. Navarro-Pardo, F. Vidal, H. Zhao, Z.M. Wang, F. Rosei, A colloidal heterostructured quantum dot sensitized carbon nanotube–TiO 2 hybrid photoanode for high efficiency hydrogen generation, Nanoscale Horizons, 4 (2019) 404-414.

[154] G.S. Selopal, M. Mohammadnezhad, L.V. Besteiro, O. Cavuslar, J. Liu, H. Zhang, F. Navarro-Pardo, G. Liu, M. Wang, E.G. Durmusoglu, Synergistic effect of plasmonic gold nanoparticles decorated carbon nanotubes in quantum dots/TiO2 for optoelectronic devices, Advanced Science, 7 (2020) 2001864.

[155] H. Han, F. Karlicky, S. Pitchaimuthu, S.H.R. Shin, A. Chen, Highly ordered N-doped carbon dots photosensitizer on metal–organic framework-decorated ZnO nanotubes for improved photoelectrochemical water splitting, Small, 15 (2019) 1902771.

[156] S. Cao, X. Yan, Z. Kang, Q. Liang, X. Liao, Y. Zhang, Band alignment engineering for improved performance and stability of ZnFe2O4 modified CdS/ZnO nanostructured photoanode for PEC water splitting, Nano Energy, 24 (2016) 25-31.

[157] K. Wang, X. Tong, Y. Zhou, H. Zhang, F. Navarro-Pardo, G.S. Selopal, G. Liu, J. Tang, Y. Wang, S. Sun, Efficient solar-driven hydrogen generation using colloidal heterostructured quantum dots, Journal of materials chemistry A, 7 (2019) 14079-14088.

[158] T. Zhou, S. Chen, L. Li, J. Wang, Y. Zhang, J. Li, J. Bai, L. Xia, Q. Xu, M. Rahim, Carbon quantum dots modified anatase/rutile TiO2 photoanode with dramatically enhanced photoelectrochemical performance, Applied Catalysis B: Environmental, 269 (2020) 118776.

[159] Z. Liang, H. Hou, Z. Fang, F. Gao, L. Wang, D. Chen, W. Yang, Hydrogenated TiO2 nanorod arrays decorated with carbon quantum dots toward efficient photoelectrochemical water splitting, ACS applied materials & interfaces, 11 (2019) 19167-19175.

[160] H. Zhao, C. Wang, G. Liu, D. Barba, F. Vidal, G. Han, F. Rosei, Efficient and stable hydrogen evolution based on earth-abundant SnSe nanocrystals, Applied Catalysis B: Environmental, 264 (2020) 118526.

[161] N. Alvi, P. Soto Rodriguez, P. Kumar, V. Gómez, P. Aseev, A. Alvi, M. Alvi, M. Willander, R. Nötzel, Photoelectrochemical water splitting and hydrogen generation by a spontaneously formed InGaN nanowall network, Applied Physics Letters, 104 (2014).

[162] X. Tong, Y. Zhou, L. Jin, K. Basu, R. Adhikari, G.S. Selopal, H. Zhao, S. Sun, A. Vomiero, Z.M. Wang, Heavy metal-free, near-infrared colloidal quantum dots for efficient photoelectrochemical hydrogen generation, Nano Energy, 31 (2017) 441-449.

[163] F. Li, M. Zhang, D. Benetti, L. Shi, L.V. Besteiro, H. Zhang, J. Liu, G.S. Selopal, S. Sun, Z. Wang, “Green”, gradient multi-shell $CuInSe_2/(CuInSe_xS_{1-x})_5/CuInS_2$ quantum dots for photo-electrochemical hydrogen generation, Applied Catalysis B: Environmental, 280 (2021) 119402.

[164] C. Kim, M. Kikumori, A. Kim, J. Kim, How do moral judgment and saving face interact with positive word–of–mouth regarding counterfeit luxury consumption?, Journal of Global Fashion Marketing, (2023) 1-17.

[165] R. Arppe, T.J. Sørensen, Physical unclonable functions generated through chemical methods for anti-counterfeiting, Nature Reviews Chemistry, 1 (2017) 0031.

[166] W. Ren, G. Lin, C. Clarke, J. Zhou, D. Jin, Optical nanomaterials and enabling technologies for high-security-level anticounterfeiting, Advanced Materials, 32 (2020) 1901430.

[167] Z. Zhuo, Y. Liu, D. Liu, P. Huang, F. Jiang, X. Chen, M. Hong, Manipulating energy transfer in lanthanide-doped single nanoparticles for highly enhanced upconverting luminescence, Chemical Science, 8 (2017) 5050-5056.

[168] Z. Feng, W. Zhao, Z. Liang, Y. Lv, F. Xiang, D. Sun, C. Xiong, C. Duan, L. Dai, Y. Ni, A new kind of nonconventional luminogen based on aliphatic polyhydroxyurethane and its potential application in ink-free anticounterfeiting printing, ACS applied materials & interfaces, 12 (2020) 11005-11015.

[169] P. Li, J. Zeng, B. Wang, Z. Cheng, J. Xu, W. Gao, K. Chen, Waterborne fluorescent dual anti-counterfeiting ink based on Yb/Er-carbon quantum dots grafted with dialdehyde nano-fibrillated cellulose, Carbohydrate polymers, 247 (2020) 116721.

[170] L. Xu, J. Chen, J. Song, J. Li, J. Xue, Y. Dong, B. Cai, Q. Shan, B. Han, H. Zeng, Double-protected all-inorganic perovskite nanocrystals by crystalline matrix and silica for triple-modal anti-counterfeiting codes, ACS applied materials & interfaces, 9 (2017) 26556-26564.

[171] C. Li, Z. Zang, W. Chen, Z. Hu, X. Tang, W. Hu, K. Sun, X. Liu, W. Chen, Highly pure green light emission of perovskite CsPbBr 3 quantum dots and their application for green light-emitting diodes, Optics express, 24 (2016) 15071-15078.

[172] S. Xie, G. Gong, Y. Song, H. Tan, C. Zhang, N. Li, Y. Zhang, L. Xu, J. Xu, J. Zheng, Design of novel lanthanide-doped core–shell nanocrystals with dual up-conversion and down-

conversion luminescence for anti-counterfeiting printing, Dalton Transactions, 48 (2019) 6971-6983.

[173] M. Zuo, W. Qian, T. Li, X.-Y. Hu, J. Jiang, L. Wang, Full-color tunable fluorescent and chemiluminescent supramolecular nanoparticles for anti-counterfeiting inks, ACS applied materials & interfaces, 10 (2018) 39214-39221.

[174] Y. Zhang, R. Huang, H. Li, Z. Lin, D. Hou, Y. Guo, J. Song, C. Song, Z. Lin, W. Zhang, Triple-mode emissions with invisible near-infrared after-glow from Cr3+-doped zinc aluminum germanium nanoparticles for advanced anti-counterfeiting applications, Small, 16 (2020) 2003121.

[175] M. Ding, B. Dong, Y. Lu, X. Yang, Y. Yuan, W. Bai, S. Wu, Z. Ji, C. Lu, K. Zhang, Energy manipulation in lanthanide-doped core–shell nanoparticles for tunable dual-mode luminescence toward advanced anti-counterfeiting, Advanced Materials, 32 (2020) 2002121.

[176] L. Chen, C. Lai, R. Marchewka, R. Berry, K. Tam, Use of CdS quantum dot-functionalized cellulose nanocrystal films for anti-counterfeiting applications, Nanoscale, 8 (2016) 13288-13296.

[177] Y. Liu, F. Han, F. Li, Y. Zhao, M. Chen, Z. Xu, X. Zheng, H. Hu, J. Yao, T. Guo, Inkjet-printed unclonable quantum dot fluorescent anti-counterfeiting labels with artificial intelligence authentication, Nature communications, 10 (2019) 2409.

[178] B. Luo, J. Liu, H. Guo, X. Liu, R. Song, K. Shen, Z.M. Wang, D. Jing, G.S. Selopal, F. Rosei, High efficiency photoelectrochemical hydrogen generation using eco-friendly Cu doped Zn-In-Se colloidal quantum dots, Nano Energy, 88 (2021) 106220.

[179] J. Lim, W.K. Bae, D. Lee, M.K. Nam, J. Jung, C. Lee, K. Char, S. Lee, InP@ ZnSeS, core@ composition gradient shell quantum dots with enhanced stability, Chemistry of Materials, 23 (2011) 4459-4463.

[180] X. Liu, B. Luo, J. Liu, D. Jing, D. Benetti, F. Rosei, Eco-friendly quantum dots for liquid luminescent solar concentrators, Journal of materials chemistry A, 8 (2020) 1787-1798.

[181] H. Zhong, Z. Wang, E. Bovero, Z. Lu, F.C. Van Veggel, G.D. Scholes, Colloidal CuInSe2 nanocrystals in the quantum confinement regime: synthesis, optical properties, and electroluminescence, The Journal of Physical Chemistry C, 115 (2011) 12396-12402.

[182] Q. Guo, S.J. Kim, M. Kar, W.N. Shafarman, R.W. Birkmire, E.A. Stach, R. Agrawal, H.W. Hillhouse, Development of CuInSe2 nanocrystal and nanoring inks for low-cost solar cells, Nano letters, 8 (2008) 2982-2987.

[183] M.G. Panthani, V. Akhavan, B. Goodfellow, J.P. Schmidtke, L. Dunn, A. Dodabalapur, P.F. Barbara, B.A. Korgel, Synthesis of CuInS2, CuInSe2, and Cu (In x Ga1-x) Se2 (CIGS) nanocrystal “inks” for printable photovoltaics, Journal of the American Chemical Society, 130 (2008) 16770-16777.

[184] M.G. Panthani, T.A. Khan, D.K. Reid, D.J. Hellebusch, M.R. Rasch, J.A. Maynard, B.A. Korgel, In Vivo Whole Animal Fluorescence Imaging of a Microparticle-Based Oral Vaccine Containing (Cuinse X S2–X)/Zns Core/Shell Quantum Dots, Nano letters, 13 (2013) 4294-4298.

[185] C.L. McCarthy, D.H. Webber, E.C. Schueller, R.L. Brutchey, Solution-Phase Conversion of Bulk Metal Oxides to Metal Chalcogenides Using a Simple Thiol–Amine Solvent Mixture, Angewandte Chemie, 127 (2015) 8498-8501.

[186] D.H. Webber, R.L. Brutchey, Alkahest for V2VI3 chalcogenides: dissolution of nine bulk semiconductors in a diamine-dithiol solvent mixture, Journal of the American Chemical Society, 135 (2013) 15722-15725.

[187] D.H. Webber, J.J. Buckley, P.D. Antunez, R.L. Brutchey, Facile dissolution of selenium and tellurium in a thiol–amine solvent mixture under ambient conditions, Chemical Science, 5 (2014) 2498-2502.

[188] J. Liu, S. Yue, H. Zhang, C. Wang, D. Barba, F. Vidal, S. Sun, Z.M. Wang, J. Bao, H. Zhao, Efficient Photoelectrochemical Hydrogen Generation Using Eco-Friendly “Giant” InP/ZnSe Core/Shell Quantum Dots, ACS Applied Materials & Interfaces, 15 (2023) 34797-34808.

[189] L. Jin, E. Hamzehpoor, G.S. Selopal, J. Liu, P. Kumar, D. Benetti, X. Tong, D.F. Perepichka, Z.M. Wang, F. Rosei, Harnessing the Synergetic Effects of Ag, Mn Dopants in Eco-Friendly Ultraviolet Selective Quantum Dots for Luminescent Solar Concentrators, Small Methods, (2024) 2301695.

[190] Y. Tao, Z. Tang, D. Bao, H. Zhao, Z. Gao, M. Peng, H. Zhang, K. Wang, X. Sun, Surface Stoichiometry Control of Colloidal Heterostructured Quantum Dots for High-Performance Photoelectrochemical Hydrogen Generation, Small, 19 (2023) 2206316.

[191] S. Hachiya, Q. Shen, T. Toyoda, Effect of ZnS coatings on the enhancement of the photovoltaic properties of PbS quantum dot-sensitized solar cells, Journal of Applied Physics, 111 (2012).

[192] B.J. Inkson, Scanning electron microscopy (SEM) and transmission electron microscopy (TEM) for materials characterization, in: Materials characterization using nondestructive evaluation (NDE) methods, Elsevier, 2016, pp. 17-43.

[193] J.I. Goldstein, D.E. Newbury, J.R. Michael, N.W. Ritchie, J.H.J. Scott, D.C. Joy, Scanning electron microscopy and X-ray microanalysis, springer, 2017.

[194] X. Dong, J. Xu, H. Yang, X. Zhang, Z. Mo, S. Shi, L. Li, S. Yin, Effect of Ligand Exchange on the Photoluminescence Properties of Cu-Doped Zn-In-Se Quantum Dots, Journal of Electronic Materials, 47 (2018) 2241-2248.

[195] G. Liu, W. Liang, X. Xue, F. Rosei, Y. Wang, Atomic identification of interfaces in individual core@ shell quantum dots, Advanced Science, 8 (2021) 2102784.

[196] Z. Kaszkur, Powder diffraction beyond the Bragg law: study of palladium nanocrystals, Journal of applied crystallography, 33 (2000) 1262-1270.

[197] L. Huang, R. Yao, X. Wang, S. Sun, X. Zhu, X. Liu, M.G. Kim, J. Lian, F. Liu, Y. Li, In situ phosphating of Zn-doped bimetallic skeletons as a versatile electrocatalyst for water splitting, Energy & Environmental Science, 15 (2022) 2425-2434.

[198] B. Ma, Q. Xu, H. Yao, Y. Chen, Y. Wang, Y. Yang, H. Shen, Y. Lu, Constructing the Cu_2O@Au/Cu_2O integrated heterostructure cooperated with LSPR effect for enhanced photocatalytic performance via a three-in-one synergy, Journal of Photochemistry and Photobiology A: Chemistry, 446 (2024) 115100.

[199] J. Vavra, G.P. Ramona, F. Dattila, A. Kormányos, T. Priamushko, P.P. Albertini, A. Loiudice, S. Cherevko, N. Lopéz, R. Buonsanti, Solution-based Cu+ transient species mediate the reconstruction of copper electrocatalysts for CO2 reduction, Nature Catalysis, (2024) 1-9.

[200] H. Dong, L. Tong, P. Zhang, D. Zhu, J. Jiang, C. Li, Built-in electric field intensified by photothermoelectric effect drives charge separation over Z-scheme 3D/2D In_2Se_3/PCN

heterojunction for high-efficiency photocatalytic CO2 reduction, Journal of Materials Science & Technology, 179 (2024) 251-261.

[201] N. Tsolekile, S. Parani, M.C. Matoetoe, S.P. Songca, O.S. Oluwafemi, Evolution of ternary I–III–VI QDs: Synthesis, characterization and application, Nano-Structures & Nano-Objects, 12 (2017) 46-56.

[202] L. Dhamo, F. Carulli, P. Nickl, K.D. Wegner, V.D. Hodoroaba, C. Würth, S. Brovelli, U. Resch-Genger, Efficient Luminescent Solar Concentrators Based on Environmentally Friendly Cd-Free Ternary AIS/ZnS Quantum Dots, Advanced optical materials, 9 (2021) 2100587.

[203] J. Zhu, S. Mei, W. Yang, G. Zhang, Q. Chen, W. Zhang, R. Guo, Tunable emission of Cu (Mn)-doped ZnInS quantum dots via dopant interaction, Journal of colloid and interface science, 506 (2017) 27-35.

[204] J. Park, S.-W. Kim, $CuInS_2$/ZnS core/shell quantum dots by cation exchange and their blue-shifted photoluminescence, Journal of Materials Chemistry, 21 (2011) 3745-3750.

[205] J. Cho, Y.K. Jung, J.-K. Lee, H.-S. Jung, Highly efficient blue-emitting CdSe-derived core/shell gradient alloy quantum dots with improved photoluminescent quantum yield and enhanced photostability, Langmuir, 33 (2017) 3711-3719.

[206] G. Wilcox, D. Gabe, Faraday's laws of electrolysis, Transactions of the IMF, 70 (1992) 93-94.

[207] B.-A. Mei, O. Munteshari, J. Lau, B. Dunn, L. Pilon, Physical interpretations of Nyquist plots for EDLC electrodes and devices, The Journal of Physical Chemistry C, 122 (2018) 194-206.

[208] M.M. Abouelela, G. Kawamura, A. Matsuda, Metal chalcogenide-based photoelectrodes for photoelectrochemical water splitting, Journal of Energy Chemistry, 73 (2022) 189-213.

[209] L. Jin, G. Sirigu, X. Tong, A. Camellini, A. Parisini, G. Nicotra, C. Spinella, H. Zhao, S. Sun, V. Morandi, Engineering interfacial structure in “Giant” PbS/CdS quantum dots for photoelectrochemical solar energy conversion, Nano Energy, 30 (2016) 531-541.

[210] Y. Shi, W. Du, W. Zhou, C. Wang, S. Lu, S. Lu, B. Zhang, Unveiling the promotion of surface-adsorbed chalcogenate on the electrocatalytic oxygen evolution reaction, Angewandte Chemie International Edition, 59 (2020) 22470-22474.

[211] L. Jin, J. Liu, X. Liu, D. Benetti, G.S. Selopal, X. Tong, E. Hamzehpoor, F. Li, D.F. Perepichka, Z.M. Wang, Rational Control of Near-Infrared Colloidal Thick-Shell Eco-Friendly Quantum Dots for Solar Energy Conversion, Small Methods, 8 (2024) 2300133.

[212] C. Liu, X. Tong, A.I. Channa, X. Li, Z. Long, H. Feng, Y. You, R. Wang, F. Lin, C.F. Dee, Tuning the composition of heavy metal-free quaternary quantum dots for improved photoelectrochemical performance, Journal of Materials Chemistry A, 9 (2021) 5825-5832.

[213] Y. You, X. Tong, A.I. Channa, X. Li, C. Liu, H. Ye, Z. Wang, Tailoring the optoelectronic properties of eco-friendly $CuGaS_2$/ZnSe core/shell quantum dots for boosted photoelectrochemical solar hydrogen production, EcoMat, 4 (2022) e12206.

[214] Z. Long, X. Tong, C. Liu, A.I. Channa, R. Wang, X. Li, F. Lin, A. Vomiero, Z.M. Wang, Near-infrared, eco-friendly ZnAgInSe quantum dots-sensitized graphene oxide-TiO_2 hybrid photoanode for high performance photoelectrochemical hydrogen generation, Chemical Engineering Journal, 426 (2021) 131298.

[215] X. Tong, A.I. Channa, Y. You, P. Wei, X. Li, F. Lin, J. Wu, A. Vomiero, Z.M. Wang, Boosting the performance of eco-friendly quantum dots-based photoelectrochemical cells via effective surface passivation, Nano Energy, 76 (2020) 105062.

[216] J. Kim, Y.J. Jang, W. Baek, A.R. Lee, J.-Y. Kim, T. Hyeon, J.S. Lee, Highly efficient photoelectrochemical hydrogen production using nontoxic CuIn1. 5Se3 quantum dots with ZnS/SiO2 double overlayers, ACS Applied Materials & Interfaces, 14 (2021) 603-610.

[217] H. Zhao, W. Wang, X. Li, P. Li, M. Cai, Y. You, R. Wang, A.I. Channa, X. Tong, Z.M. Wang, Engineering the Interfacial Structure of Heavy Metal-Free Colloidal Heterostructured Quantum Dots for High-Efficiency Photoelectrochemical Water Oxidation without Co-Catalyst, Advanced Energy and Sustainability Research, 4 (2023) 2200142.

[218] R. Wang, X. Tong, A.I. Channa, Q. Zeng, J. Sun, C. Liu, X. Li, J. Xu, F. Lin, G.S. Selopal, Environmentally friendly Mn-alloyed core/shell quantum dots for high-efficiency photoelectrochemical cells, Journal of Materials Chemistry A, 8 (2020) 10736-10741.

[219] H. Zhao, X. Li, M. Cai, C. Liu, Y. You, R. Wang, A.I. Channa, F. Lin, D. Huo, G. Xu, Role of copper doping in heavy metal-free InP/ZnSe core/shell quantum dots for highly efficient and stable photoelectrochemical cell, Advanced Energy Materials, 11 (2021) 2101230.

[220] A. Sabah, I. Shafaqat, A. Naifar, H. Albalawi, M.S. Alqahtani, M. Ashiq, S.A. Shabbir, Investigation of band parameters and electrochemical analysis of multi core-shell CdSe/CdS/ZnS quantum dots, Optical Materials, 142 (2023) 114065.

[221] Z. Zhang, T. Zhang, J. Wang, J. Han, L. Li, Photoluminescence from Cu/Mn: ZnSe quantum dots and their phase transformation in silicate glass, Journal of Luminescence, 258 (2023) 119766.

[222] V. Proshchenko, Y. Dahnovsky, Long-lived emission in Mn doped CdS, ZnS, and ZnSe diluted magnetic semiconductor quantum dots, Chemical Physics, 461 (2015) 58-62.

[223] F. Cao, S. Wang, F. Wang, Q. Wu, D. Zhao, X. Yang, A layer-by-layer growth strategy for large-size InP/ZnSe/ZnS core–shell quantum dots enabling high-efficiency light-emitting diodes, Chemistry of Materials, 30 (2018) 8002-8007.

[224] S. Das, G. Rana, F. Ali, A. Datta, Single particle level dynamics of photoactivation and suppression of Auger recombination in aqueous Cu-doped CdS quantum dots, Nanoscale, 15 (2023) 4469-4476.

[225] Y.-M. Sung, S.R. Gayam, P.-Y. Hsieh, H.-Y. Hsu, E.W.-G. Diau, S.-P. Wu, Quinone-modified Mn-doped zns quantum dots for room-temperature phosphorescence sensing of human cancer cells that overexpress NQO1, ACS applied materials & interfaces, 7 (2015) 25961-25969.

[226] P. KR, R. Viswanatha, Mechanism of Mn emission: Energy transfer vs charge transfer dynamics in Mn-doped quantum dots, APL Materials, 8 (2020).

[227] J. Wang, Y. Li, Q. Shen, T. Izuishi, Z. Pan, K. Zhao, X. Zhong, Mn doped quantum dot sensitized solar cells with power conversion efficiency exceeding 9%, Journal of materials chemistry A, 4 (2016) 877-886.

[228] L. Chang, X. He, L. Chen, Y. Zhang, Mercaptophenylboronic acid-capped Mn-doped ZnS quantum dots for highly selective and sensitive fluorescence detection of glycoproteins, Sensors and Actuators B: Chemical, 243 (2017) 72-77.

[229] S. Tomar, S. Gupta, S. Mukherjee, A. Singh, S. Kumar, R.K. Choubey, Manganese-doped ZnS QDs: an investigation into the optimal amount of doping, Semiconductors, 54 (2020) 1450-1458.

[230] T.P. Nguyen, Q.V. Lam, T.B. Vu, Effects of precursor molar ratio and annealing temperature on structure and photoluminescence characteristics of Mn-doped ZnS quantum dots, Journal of Luminescence, 196 (2018) 359-367.

[231] W. Zhang, Y. Li, H. Zhang, X. Zhou, X. Zhong, Facile synthesis of highly luminescent Mn-doped ZnS nanocrystals, Inorganic Chemistry, 50 (2011) 10432-10438.

[232] H. Zhang, J. Liu, C. Wang, G.S. Selopal, D. Barba, Z.M. Wang, S. Sun, H. Zhao, F. Rosei, Near-infrared colloidal manganese-doped quantum dots: Photoluminescence mechanism and temperature response, ACS photonics, 6 (2019) 2421-2431.

[233] T. Xue, Y. Shi, J. Guo, M. Guo, Y. Yan, Preparation of AgInS2 quantum dots and their application for Pb2+ detection based on fluorescence quenching effect, Vacuum, 193 (2021) 110514.

[234] M. Ferriol, A. Gentilhomme, M. Cochez, N. Oget, J. Mieloszynski, Thermal degradation of poly (methyl methacrylate)(PMMA): modelling of DTG and TG curves, Polymer degradation and stability, 79 (2003) 271-281.

[235] B. Bai, M. Xu, J. Li, S. Zhang, C. Qiao, J. Liu, J. Zhang, Dopant diffusion equilibrium overcoming impurity loss of doped QDs for multimode anti-counterfeiting and encryption, Advanced Functional Materials, 31 (2021) 2100286.

[236] J. Lewis, S. Wu, X. Jiang, Unconventional gap state of trapped exciton in lead sulfide quantum dots, Nanotechnology, 21 (2010) 455402.

[237] D. Kim, T. Kuwabara, M. Nakayama, Photoluminescence properties related to localized states in colloidal PbS quantum dots, Journal of luminescence, 119 (2006) 214-218.

[238] H. Kim, B.-H. Kwon, M. Suh, D.S. Kang, Y. Kim, D.Y. Jeon, Degradation characteristics of red light-emitting $CuInS_2$/ZnS quantum dots as a wavelength converter for LEDs, Electrochemical and Solid-State Letters, 14 (2011) K55.

[239] W. Han, X. Wen, Y. Ding, Z. Li, M. Lu, H. Zhu, G. Wang, J. Yan, X. Hong, Ultraviolet emissive Ti3C2Tx MXene quantum dots for multiple anti-counterfeiting, Applied Surface Science, 595 (2022) 153563.

[240] W. Li, Y. Han, L. Wang, G.S. Selopal, X. Wang, H. Zhao, Highly bright solid-state carbon dots for efficient anticounterfeiting, RSC advances, 14 (2024) 83-89.

[241] Y. Liu, L. Zhou, Y. Li, R. Deng, H. Zhang, Highly fluorescent nitrogen-doped carbon dots with excellent thermal and photo stability applied as invisible ink for loading important information and anti-counterfeiting, Nanoscale, 9 (2017) 491-496.

[242] F. Zhang, Z. Shi, S. Li, Z. Ma, Y. Li, L. Wang, D. Wu, Y. Tian, G. Du, X. Li, Synergetic effect of the surfactant and silica coating on the enhanced emission and stability of perovskite quantum dots for anticounterfeiting, ACS applied materials & interfaces, 11 (2019) 28013-28022.

[243] M. Chen, X. Zhang, C. Luo, R. Qi, H. Peng, H. Lin, Highly stable waterborne luminescent inks based on $MAPbBr_3$@PbBr (OH) nanocrystals for LEDs and anticounterfeit applications, ACS applied materials & interfaces, 13 (2021) 20622-20632.

[244] Z. Yang, C.-Q. Lin, M.-L. Liu, H. Wang, C.-Y. Pan, Dual-emission Mn-doped CsPbCl3 QDs in collaboration with CsPbBr3 QDs applied in excitation-sensitive flexible anti-counterfeiting technologies, Journal of Solid State Chemistry, 332 (2024) 124584.

[245] Y. Shi, X. Su, X. Wang, M. Ding, In Situ Synthesis of CsPbX3/Polyacrylonitrile Nanofibers with Water-Stability and Color-Tunability for Anti-Counterfeiting and LEDs, Polymers, 16 (2024) 1568.

[246] C. Zhou, F. Xu, W. Wang, W. Nie, W. You, X. Ye, Simple synthesis of dual-emission $CsPbBr_3$@ EuBTC composite for latent fingerprints and optical anti-counterfeiting applications, Materials Today Communications, 33 (2022) 104493.

[247] A.J. Nozik, O.I. Mićić, Colloidal quantum dots of III-V semiconductors, MRs Bulletin, 23 (1998) 24-30.

[248] O.E. Semonin, J.M. Luther, S. Choi, H.-Y. Chen, J. Gao, A.J. Nozik, M.C. Beard, Peak external photocurrent quantum efficiency exceeding 100% via MEG in a quantum dot solar cell, Science, 334 (2011) 1530-1533.

[249] K. Wu, H. Zhu, T. Lian, Ultrafast exciton dynamics and light-driven H_2 evolution in colloidal semiconductor nanorods and Pt-tipped nanorods, Accounts of Chemical Research, 48 (2015) 851-859.

[250] G. Liu, R. Mazzaro, Y. Wang, H. Zhao, A. Vomiero, High efficiency sandwich structure luminescent solar concentrators based on colloidal quantum dots, Nano Energy, 60 (2019) 119-126.

[251] Y.-H. Won, O. Cho, T. Kim, D.-Y. Chung, T. Kim, H. Chung, H. Jang, J. Lee, D. Kim, E. Jang, Highly efficient and stable InP/ZnSe/ZnS quantum dot light-emitting diodes, Nature, 575 (2019) 634-638.

List of Publications, Conference Presentations and Awards

Publications:

[1] S. Kokilavani, G.S. Selopal, L. Jin, P. Kumar, D. Barba, F. Rosei, (2024). Dual aliovalent dopants Cu, Mn engineered eco-friendly QDs for ultra-stable anti-counterfeiting. Chemistry–A European Journal, e202402026.

Conference presentations **:**

[1] S. Kokilavani, G.S. Selopal, L. Jin, F. Rosei, *Enhanced tuneable emission of environment-friendly Cu, Mn dopants modulated $ZnInSe_2$/ZnSe core/shell QDs for ultra-stable fluorescent anti-counterfeiting*, 36th International Conference on the Physics of Semiconductors (ICPS2024)-Foundation of Quantum Technology, Ottawa, Canada -**Poster**

[2] S. Kokilavani, G.S. Selopal, L. Jin, F. Rosei, *Environment-friendly Cu:$ZnInSe_2$/ZnSeS core/shell QDs sensitized TiO_2 photoanode for efficient photoelectrochemical hydrogen production*, Canadian Materials Science Conference, University of Alberta, Edmonton, Alberta, Canada, May 22-25, 2024 - **Oral**

[3] S. Kokilavani, G.S. Selopal, L. Jin, F. Rosei, *Advancing Clean Energy: Surface-Engineered heavy-metal-free Cu-doped $ZnInSe_2$ QDs for efficient and stable photoelectrochemical H_2 Production*, INRS-EMT Scientific Colloquium, Montreal, Quebec, February 20th, 2024 – **Oral**

[4] S. Kokilavani, G.S. Selopal, L. Jin, F. Rosei, *"Green" Cu@ZnInSe/ZnSeS core/composition gradient shell for boosted photoelectrochemical H_2 production*, 2024 MRS Spring Meeting & Exhibit, Seattle, Washington, USA, April 22-26th, 2024 – **E-Poster**

[5] S. Kokilavani, G.S. Selopal, L. Jin, F. Rosei, "*Green" Cu@ZnInSe/ZnSeS core/composition gradient shell for boosted Photoelectrochemical H_2 production*, 7th Montreal Photonics Networking event, ETS, Montreal, Quebec, December 1st, 2023 – **Poster**

Awards:

[1] Received *Student Travel Grant Award* of "**450$**" for the CMSC Conference, Alberta, Canada.

APPENDIX B SYNOPSIS

DEVELOPPEMENT DE POINTS QUANTIQUES COLLOÏDAUX TERNAIRES SANS METAUX LOURDS POUR DES APPLICATIONS DANS LA SECURITE ET L'ENERGIE

Introduction

Les nanocristaux semi-conducteurs colloïdaux, également connus sous le nom de points quantiques (QD) sont des particules à l'échelle nanométrique (généralement dans la plage de taille d'environ 2 à 20 nm) qui sont analogues aux semi-conducteurs en vrac et diffèrent en fonction de l'effet de confinement quantique (Figure 1a-c) [28]. Les QD présentent des propriétés optiques et électroniques dépendantes de la taille, de la composition et de la forme avec le potentiel de construire des dispositifs optoélectroniques. Les QD ouvrent des possibilités d'intégration aux semi-conducteurs inorganiques et peuvent être fabriqués comme un dispositif haute performance en utilisant des méthodes à basse température, à grande surface et basées sur des solutions plutôt que des procédés de fabrication coûteux, à vide élevé et à haute température [2, 3].

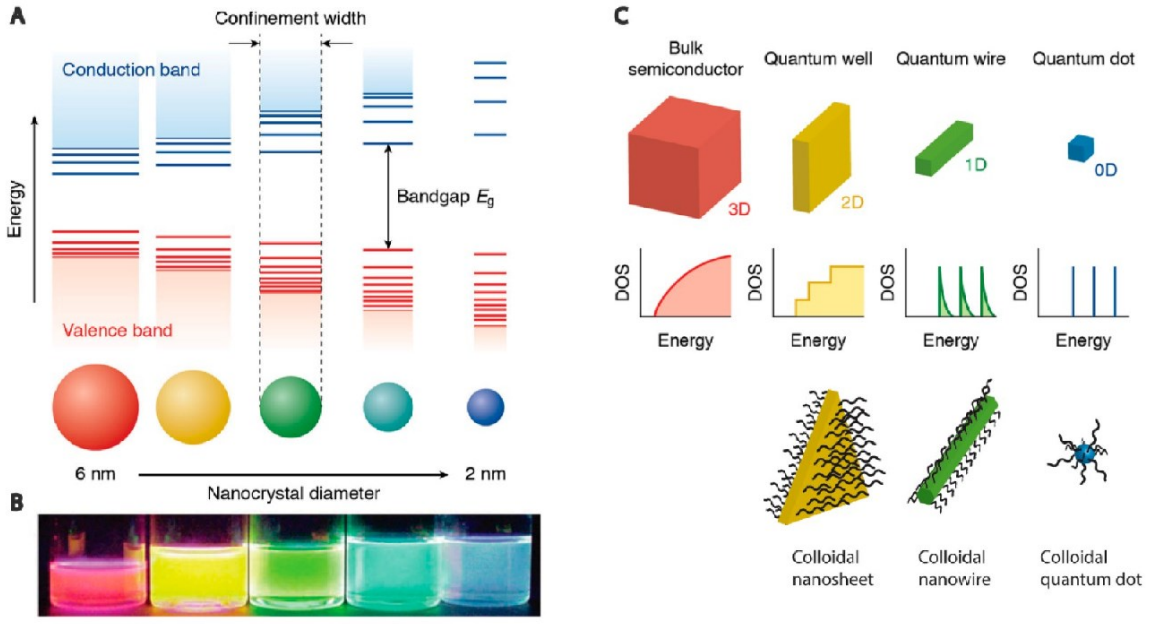

Figure 1 (a) Effets de confinement quantique dans les QDs. (b) CdSe QDs de différentes tailles sous irradiation de lumière UV. c) Représentation schématique du semi-conducteur dans différentes dimensions et de leur densité d'états correspondante. Les ligands organiques ont plafonné différents NCs colloïdaux de 2D à 0D (panneau inférieur) [4].

Les QD sont généralement constitués de semi-conducteurs II-VI, III-V et IV-VI en utilisant des approches synthétiques chimiques humides à faible coût et évolutives. La méthodologie synthétique a été avancée pour adapter avec précision les QDs en fonction de la taille, de la forme et de la composition pour des applications pertinentes [247]. Murray, Norris et Bawendi présentent une voie simple pour synthétiser des CdE monodispersés de haute qualité (E= Se, S et Te) [9]. Différentes tailles de 1,2 à 11,5 nm (diamètre par son axe principal) ont été produites avec une cristallinité cohérente, un degré élevé de monopersité et une dérivatisation de surface en une seule réaction. Le prix Nobel de chimie 2023 a été décerné pour la découverte et la synthèse de points quantiques colloïdalement stables en tant qu'invention révolutionnaire dans le domaine de la nanotechnologie [10]. Les CQD sont conçus pour avoir des propriétés optiques et électriques uniques par la composition de réglage, l'architecture de la structure et le dopage des impuretés pour de larges applications allant de l'imagerie biologique aux applications optoélectroniques (Figure 2).

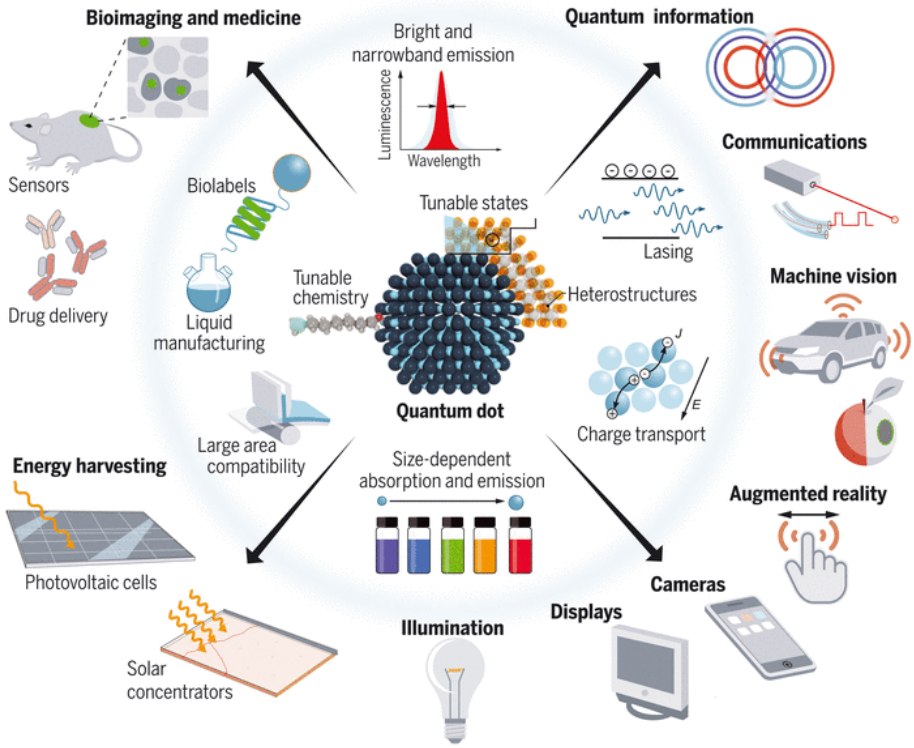

Figure 2 QDs avec leurs caractéristiques uniques pour différentes applications de l'information quantique à la bioimagerie et à la médecine [6].

QDs d'ingénierie de composition

Les QDs conçus pour la composition sont synthétisés avec une composition d'éléments spécifiques de différents groupes dans le tableau périodique. Les QD II-VI sont l'un des

systèmes les plus largement étudiés en raison de ses propriétés photophysiques idéales, notamment une cristallinité et une morphologie parfaites, une excellente stabilité, un PLQY proche de l'unité et une désintégration PL mono-exponentielle [23]. Les QD II-VI sont composés d'éléments des groupes II et VI du tableau périodique, tels que le CdS, cdSe, PbS, PbTe, CdTe et ainsi de suite. Parmi les réalisations notables, citons le développement de cellules PEC basées sur des QDs PbS avec une efficacité quantique externe supérieure à 100% [248], une efficacité quantique de 100% basée sur des QDs CdSe / CdS à bascule Pt [249] et une efficacité optique plus élevée des CDSe / CdS CdSe / CdSe / CdS CdSe / $Cd_{1-x}Zn_xS$ basés sur les LSC, et les QDs PbS / CdS [250]. Cependant, la présence de métaux lourds toxiques dans ces QDs de haute qualité reste un problème majeur non résolu qui limite sévèrement ses applications à l'échelle commerciale.

Les QDs du groupe III-V composés d'éléments non toxiques, y compris GaP, InP, InAs et InSb, présentent un intérêt particulier pour de nombreuses applications qui nécessitent des QDs sans Cd/Pb [46]. Depuis le milieu des années 1990 jusqu'à ce jour, la synthèse des QD III-V est connue depuis longtemps pour être extrêmement difficile par rapport à d'autres types de semi-conducteurs. En général, les QD III-V présentent une nature amorphe ou partiellement cristalline et s'oxydent facilement [47]. Bien que la cristallisation soit améliorée à haute température, elle provoque une agrégation et une précipitation irréversibles des particules. Un précurseur hautement réactif a été utilisé, comme la tris(triméthylsilyl)phosphine ou la tris(triméthylsilyl) arsine, pour obtenir un QD mono-dispersé hautement cristallin [251]. En raison du choix épars de précurseurs et des approches synthétiques limitées, les QDs du groupe III-V n'ont pas été atteints aux niveaux attendus en termes d'accordabilité spectrale [51, 52].

Récemment, respectueux de l'environnement Ternaire I-III-VI_2 QDs (où I = Cu, Ag, Au ; III = Al, Ga, In et X = S, Se, Te) sont reconnus comme des candidats prometteurs en raison de ses caractéristiques exceptionnelles, notamment l'accordabilité des écarts à large bande [53] long temps d'émission [54] et la facilité de traitement, ce qui le rend attrayant pour les applications optoélectroniques [55] et de récolte de lumière [56]. Pour les QD I-III-VI_2, la présence de défauts ponctuels interstitiels qui négocient le processus de recombinaison de charge (paire Donneur-Accepteur) donne lieu à ces propriétés optiques [57]. En règle générale, les cations de groupe I ont une grande mobilité pour former des postes vacants, ce qui explique la plupart des défauts [58]. La plupart de ces états de défaut sont domicile dans la bande interdite et responsables de la recombinaison de charge par le processus de recombinaison des paires donneur-accepteur

(DAP). Dans $AgInS_2$, l'antisite Indium (V_{Ag}^-) et le vacance argent (In_{Ag}^{2+}) dans $AgInS_2$ agissent comme les principaux centres DAP [57]. En photovoltaïque, l'existence d'états de sous-bande interdite a été préjudiciable car ils réduisent l'efficacité de conversion de puissance et la tension en circuit ouvert [59]. Les efforts actuels sont concentrés pour développer des semi-conducteurs I-III-VI_2 sans défaut. La stratégie de dopage Zn dans I-III-VI_2 QDs a été rapportée pour augmenter le PLQY et améliorer l'efficacité des cellules solaires [56]. En effet, les QDs Cu-In-Se synthétisés à partir des réactifs disponibles commerciaux ont souvent entraîné un écart par rapport au $CuInSe_2$ stœchiométrique, c'est-à-dire $CuIn_{1.5}Se_3$, $CuIn_5Se_8$ et $CuIn_{2.4}Se_4$ [60]. Azad et al. [61] a produit un $CuInSe_2$ stœchiométrique de haute qualité avec une quasi-monodispersion (environ 4 nm) en faisant réagir TOP, CuCl et $InCl_3$. Habituellement, les QD ternaires souffrent d'une forte densité de pièges / défauts de surface, qui servent de centres de recombinaison de charge. Cela peut entraîner une détérioration des performances des systèmes de récupération de l'énergie solaire. Par conséquent, l'adoption d'une stratégie de passivation de surface efficace grâce à l'ingénierie structurelle pourrait éliminer les pièges / défauts de surface pour réaliser des dispositifs à haute performance.

QDs d'ingénierie de structure

L'ingénierie structurelle adapte les états de surface pour améliorer la stabilité chimique, thermique et photochimique des QDs et les préserver de l'oxydation. La section suivante traitera des différentes architectures de cœur/coque, y compris les QDs de noyau/coque, les QDs de noyau/coque allié et les QDs de noyau/multi-coque.

Les propriétés optiques et électroniques des QDs noyau/coque montrent des caractéristiques distinctes par rapport aux QDs core-only. Typiquement, dans les QDs de noyau/shell, la coque agit comme couche protectrice et a un impact sur la distribution de charge. En fonction de l'alignement relatif de la bande des bords CB et VB des semi-conducteurs de noyau et de coque, les structures QDs cœur/coque sont classées en quatre types principaux : (i) Type I, (ii) Type inversé I, (iii) Type II, et Quasi-Type II qui permet une dynamique de charge et une stabilité différentes (Figure 3a-d).

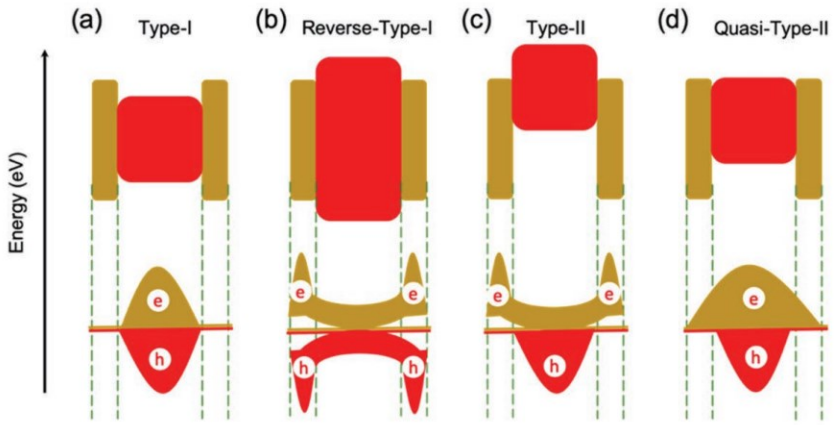

Figure 3 Différents types de QDs noyau/coque en fonction de l'alignement des bandes a) Type I, b) Type I inversé, c) Type II et d) Quasi-Type II [20].

Dans le type I, le bord CB et VB du noyau est situé à l'intérieur de la coque, comme CdSe/ZnS [78]. Lian et ses collègues [79] ont démontré que l'augmentation de l'épaisseur de la coque pour les QDs de type I CdSe/ZnS du cœur/coque diminue le taux de séparation et de recombinaison de la charge (Figure 4a). Les excitons sont confinés à l'intérieur du noyau et la passivation avec une bande interdite plus grande protège le noyau de l'environnement. En revanche, les QDs inverses de type I, tels que CdS/CdSe et ZnSe/CdSe, ont les deux bords de bande de la coque situés dans la bande interdite du noyau (Figure 4b-c). Jusqu'à présent, les QD CdSe/CdS sont l'un des systèmes de QDs de base/shell les plus étudiés et les mieux développés. Dans les QD de type II, le CB/VB du semi-conducteur de la coque est décalé avec celui du noyau. Un support est confiné à l'intérieur du noyau tandis que l'autre est principalement dans la région de la coque. En particulier, le décalage d'énergie de la bande dépend de la bande interdite efficace des QDs, qui peuvent être contrôlés en modifiant la taille du noyau et l'épaisseur de la coque. Dans le quasi-type-II, le trou ou l'électron est confiné dans le noyau, tandis que l'autre délocalisé sur la structure entière du noyau / de la coque, par exemple. CdTe/CdSe QDs. Dans les QDs noyau/coque, la limite nette induit des déformations interfaciales [93]. Typiquement, le décalage cristallographique entre les constituants a comme conséquence la contrainte aux interfaces, et par conséquent, le réglage fin de la valeur d'énergie de bande-bord et son alignement avec des composants voisins est souvent nécessaire.

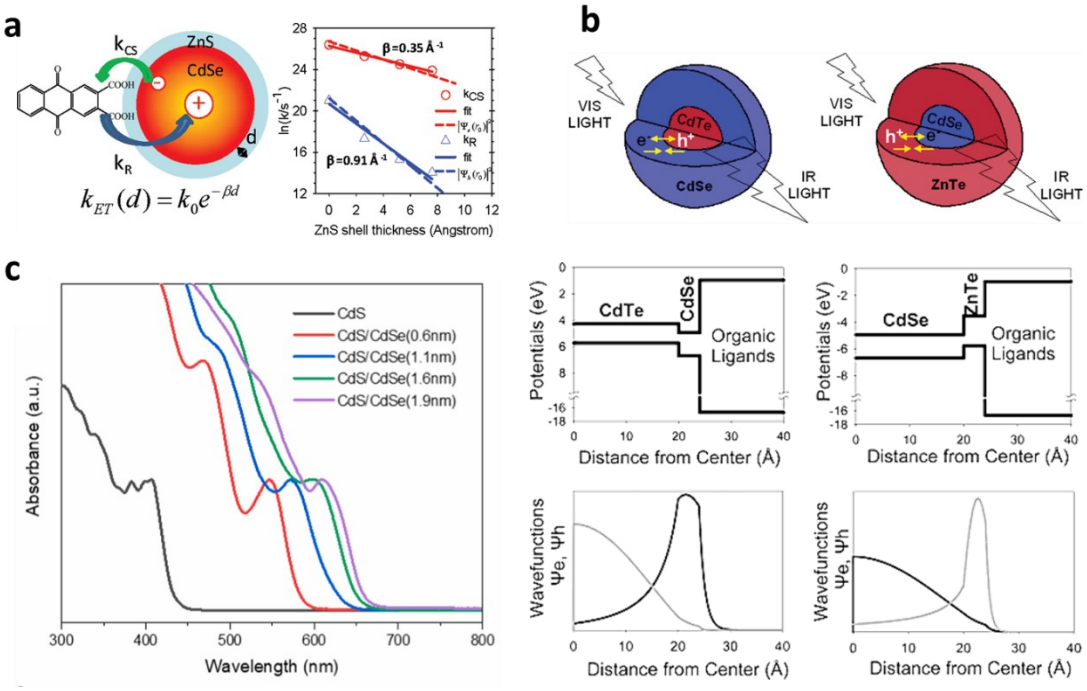

Figure 4 (a) Processus de séparation et de recombinaison de charge photoinduites dans les QDs de noyau/coque CdSe/ZnSe et le diagramme logarithmique de la séparation et de la recombinaison de charge en fonction de l'épaisseur de la coque [79]. (b) les hétérostructures CdTe/CdSe et CdSe/ZnSe de type II et leurs fonctions d'onde radiales d'électrons et de trous correspondantes [84]. c) et spectres d'absorption des QD cdS/cdSe core/shell d'épaisseur de coque différente.

Cela peut être obtenu en construisant un noyau / coque avec une limite souple via une ingénierie de composition en alliage au cœur ou à la coque. Une composition dépendante des énergies de bande interdite offre une accordabilité supplémentaire. Un CQD $Pb_ySe_{1-y}/PbSe_xS_{1-x}$ est synthétisé en une seule réaction en une seule étape en utilisant la différence de réactivité entre TOPSe et TOPS [94]. La synthèse de QDs avec plusieurs coques a été motivée par le défi de répondre simultanément aux exigences des propriétés électroniques (bande interdite, alignement de bande) et structurelles (non-concordance de réseau) dans les systèmes binaires noyau / coque [21, 81]. En particulier, le décalage du réseau entre les matériaux du noyau et de la coque limite considérablement la capacité de développer une coque épaisse sans compromettre les propriétés PL. Pour résoudre ce problème, une approche de coque intermédiaire réduisant la contrainte a été initialement introduite dans le système CdSe / ZnSe / ZnS core / shell / shell. La couche intermédiaire ZnSe agit comme un adaptateur de réseau, réduisant efficacement les déformations interfaciales entre CdSe et ZnS [98].

QDs conçus par Dopant

Les QDs dopés aux ions en métal de transition possèdent des propriétés optiques et photophysiques distinctes qui sont avantageuses par rapport aux QD non annulés, y compris le plus grand décalage de Stokes pour éviter l'auto-absorption / transfert d'énergie, des durées de vie plus longues à l'état excité, une fenêtre spectrale plus large et une stabilité chimique et thermique améliorée [100]. Le dopant crée des états électroniques dans la région midgap de la bande interdite du QD qui modifie la séparation de charge et la dynamique de recombinaison [100]. En outre, il est également possible d'ajuster les propriétés optiques et électroniques des nanocristaux semi-conducteurs en contrôlant le type et la concentration des dopants [101]. Jusqu'à présent, les ions de métaux de transition tels que Mn, Cu ou Ag ont principalement été introduits sous forme de dopants dans les QD de type II-VI (CdS, CdSe, ZnS et ZnSe) ou les QD ternaires (CuInS, AgInS, ZnCdS et ZnInS) [102, 103]. Les méthodes synthétiques traditionnelles pour préparer des CQD dopés impliquent le système de réaction avec des ions hôtes compétitifs et des ions dopants, ce qui est difficile à contrôler et à optimiser. Il en résulte souvent une grande partie des QDs non annulés, comme le révèlent leurs spectres d'émission. Dans ce contexte, Naryan et al. [104] a adopté une nouvelle stratégie de découplage du processus de dopage de la nucléation et / ou de la croissance via la nucléation-dopage et la croissance-dopage. En principe, cela permet de contrôler la position radiale des ions dopants dans les nanocristaux de l'hôte. La nucléation-dopage placerait les dopants loin des états potentiels de piège de surface, et ainsi, améliorerait les propriétés optiques. Dans les QDs Mn : ZnSe, l'excès de Se (Mn : Se - 1 : 25) aide à la formation de nanoclusters MnSe stables plus petits tandis que le faible rapport de précurseurs produit des nanocristaux MnSe de grande taille en raison de la croissance continue. La section suivante fournira une compréhension des différentes stratégies de dopage et de leur effet sur les propriétés optiques et électroniques des QDs.

QDs comme absorbeurs de lumière pour le fractionnement de l'eau PEC

Principe de fonctionnement

Dans un dispositif PEC typique, l'un des photoélectrodes est utilisé comme électrode de travail pour récolter l'énergie lumineuse de l'irradiation solaire, soit agir comme photoanode où les électrons sont des porteurs de charge mobiles ou comme photocathode où les trous sont les porteurs de charge mobiles (Figure 5a) [126]. La contre-électrode est l'endroit où l'autre demi-réaction a lieu. Une paire tandem photoanode-photocathode est une configuration plus

compliquée en cellules PEC, impliquant des réactions d'oxydation et de réduction. Ces électrodes sont trempées dans un électrolyte et reliées à un contact électrique externe. À la jonction électrolyte/électrode, la différence de potentiel chimique conduit au processus de transfert de charge, créant un flux de courant électrique jusqu'à ce que l'équilibre soit établi [127]. Le niveau de Fermi de l'électrode semi-conductrice et de l'électrolyte est aligné, ce qui provoque une flexion de la bande dans le semi-conducteur [128]. Lors de l'éclairage lumineux, plusieurs étapes cruciales se produisent dans les systèmes PEC qui sont les suivants (Photoanode à titre d'exemple) : (I) Génération de paires électron-trou après absorption de photons avec une énergie supérieure à la bande interdite (Par exemple) de semi-conducteur, (II) Séparation des paires électron-trou par champ électrique intégré, (III) Les électrons photoexcités sont tirés vers le circuit extérieur vers la contre-électrode et les trous participent à la réaction d'oxydation, (IV) Recombinaison de charge [129], et (V) réaction redox (Figure 5b) [128]. Pour réaliser une production efficace de CEE H_2, la photoélectrode qui est au cœur de la cellule PEC doit répondre à plusieurs exigences :

a) la bande interdite du semi-conducteur devrait convenir pour élargir l'absorption de la lumière avec un chevauchement maximal avec le spectre solaire.

b) La séparation des paires électron-trou photogénérées devrait être efficace.

c) Le transfert/transport de charge devrait être suffisamment rapide pour empêcher la recombinaison de charge.

d) Le fractionnement de l'eau PEC nécessite un apport d'énergie élevé (réaction en montée). Le potentiel CB du semi-conducteur devrait être plus négatif que 0.0 V contre NHE ($H_2O\ (l) \rightarrow H_2(g)\frac{1}{2}O_2$ $^+$/H_2), et le VB devrait être plus positif que 1.23 V contre NHE (O_2/H_2O). Compte tenu des pertes d'énergie, la bande interdite de semi-conducteur devrait être supérieure à 1,7 eV à température ambiante [130].

e) Les photoélectrodes doivent être chimiquement stables et résistantes à la corrosion dans des solutions aqueuses dans des conditions sombres et claires.

f) Les matériaux semi-conducteurs doivent être peu coûteux et faciles à préparer.

Depuis la découverte révolutionnaire de la division de l'eau PEC par Fujishima et Honda en 1972 [131], un effort important a été fait pour réaliser des photoélectrodes haute performance qui présentent une efficacité solaire-hydrogène élevée, et une stabilité opérationnelle à long terme [132]. Cependant, jusqu'à présent, aucune photoélectrode semi-conductrice ne peut satisfaire simultanément à toutes les exigences. Diverses recherches se sont concentrées sur les hétérojonctions avec un matériau absorbant la lumière (colorants organiques [133], complexes métalliques[134]) et semi-conducteurs en vrac (TiO_2, C_3N_4) [135]. Au cours des

dernières décennies, les dispositifs PEC basés sur QDs ont fait des progrès considérables alors que l'efficacité globale des STH est encore bien inférieure à celle de la commercialisation (STH >10% avec une stabilité à long terme >1000 h) [136], en raison de la génération de charge insuffisante à partir de la capacité de récolte de la lumière, de la recombinaison de charge non radiative indésirable et du taux d'injection de charge lente des QD aux accepteurs de charge [137]. Pour résoudre ces problèmes, le développement de matériaux et de structures utilisés dans les dispositifs PEC basés sur QDs est crucial, y compris la conception et la synthèse de QDs avec une structure de bande appropriée et une plage d'absorption de la lumière, l'amélioration de la charge des QDs sur les photoélectrodes, l'ingénierie de surface des électrodes photo pour améliorer le transport de charge et établir la stabilité à long terme.

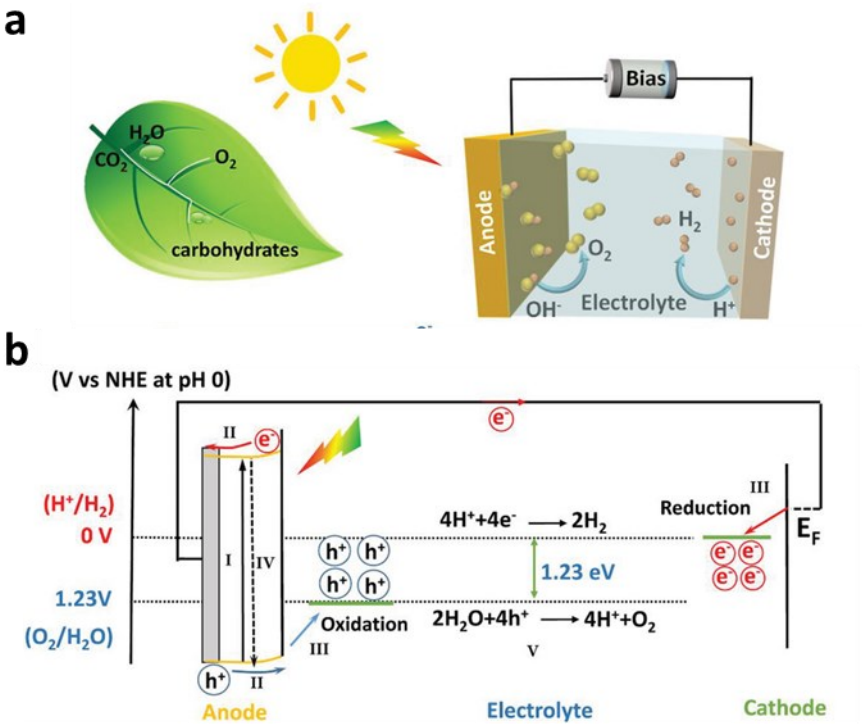

Figure 5 Illustration schématique de (a) Système typique de fractionnement de l'eau PEC. b) Dynamique du support de charge dans le système PEC à base de photoanode [138].

Défis à relever

Efficacité de l'absorption de la lumière

La génération de porteuses de charge est la première étape cruciale de la réaction PEC, où l'extension du bord d'absorption de la lumière est cruciale pour récolter un maximum de photons

pour améliorer l'efficacité STH [139]. La plupart des études étaient axées sur les QDs à base de chalcogénure actif à lumière visible en raison de leur procédure de synthèse simple et de structures de bande favorables [140]. En termes de distribution de l'énergie solaire lumineuse à la surface de la Terre, la gamme de lumière visible et NIR représente 50% alors que la lumière UV ne représente qu'environ <5% de l'ensemble du spectre solaire [141]. Par conséquent, les QDs à bande interdite étroite peuvent convenir à une exploitation optimale du spectre solaire, y compris les QDs à base de chalcogénure Pb avec des bandes interdites (1.1-1.8 eV) [142]. Par exemple, les QDs PbS (actifs dans les UV, visibles et NIR) déposés TiO_2 donnent une efficacité STH de 1,15% dans PEC avec des agents sacrificiels [143]. Néanmoins, la plage d'absorption de la lumière a été étendue au prix de la réduction de la force motrice pour injecter l'électron en raison des décalages de bande plus petits entre les QDs TiO_2 et PbS. Pour compenser le taux d'injection de charge élevé et l'absorption de la lumière, la co-sensibilisation QDs a été développée pour améliorer la collecte de photons. Un dépôt séquentiel de CdSe QDs sur des nanofils CdS QDs-ZnO augmente la densité de photocourants qui est attribuée à l'alignement de bande par étapes (CdSe/CdS/ZnO) et à une absorbance lumineuse plus élevée [144]. L'apport concurrentiel par chaque co-sensibilisant était toujours un problème à résoudre en améliorant la conception des QDs. Une autre stratégie sur le pardessus d'une coquille sur QDs a amélioré la capacité de récolte de la lumière. Jin et al. [145] a mis au point des QDs de noyau/coque PbS/CdS à base de SILAR qui montrent une large absorption de NIR (400 - 1030 nm) et ont contribué à améliorer l'absorption de la lumière, augmentant la densité de photocourant à 11,2 mA/cm^2. Bien que la coque ait amélioré les performances, les inconvénients de la méthode basée sur SILAR, tels qu'une consommation de temps élevée et une mauvaise couverture des QDs, ont stimulé le développement de QDs colloïdaux à coquille épaisse. Dans les QD à noyau colloïdal/coquille épaisse, la plage d'absorption des QDs est régie par le type et l'épaisseur de la coque. Par exemple, le remplacement de la coque ZnS par une coque CdS a étendu l'absorption de 400 nm à 600 nm [146]. Cependant, en raison de la large bande interdite de coque (CdS - 2,42 eV et ZnSe 3,25 eV), la coquille la plus épaisse a une absorption de lumière limitée, généralement inférieure à 600 nm. Généralement, l'alliage des QDs peut augmenter l'absorption. Peu d'exemples de QDs alliés incluent le TiO_2/CdS_xSe_{1-x} [147], le $ZnO/Zn_xCd_{1-x}Se$ [18] et le $ZnO/Zn_xCd_{1-x}Te$ [148]. Zhao et al. [149] les QDs synthétisés $CdSe/CdSe_{1-x}S_x$/CdSe core/alloyed shell montrent une meilleure absorption jusqu'à 650 nm par rapport aux QDs non alliés. Ces observations indiquent que l'alliage du noyau ou de la coque pourrait offrir de nouvelles possibilités d'étendre les capacités de récolte de la lumière pour utiliser une gamme d'absorption plus large du spectre solaire.

Efficacité du transport de charge

La séparation et le transport de charge sont des aspects cruciaux en dehors de l'efficacité d'absorption de la lumière dans les systèmes PEC. Les oxydes métalliques avec de plus grandes bandes intercalées ont été largement étudiés en tant que matériaux de transport d'électrons et matériaux hôtes pour les systèmes PEC en raison de leur grande mobilité des électrons, de leur stabilité électrochimique fonctionnelle, de leur propriété respectueuse de l'environnement, de leur viabilité économique et de leur correspondance des bords de bande avec le niveau de potentiel d'oxydoréduction de l'eau [150]. La conception et le contrôle rationnels de l'architecture des matériaux hôtes pourraient fournir des canaux de conduite appropriés pour le transport de charge. Dans ce contexte, différents films mésoporeux étudiés en tant que matériaux acceptant des électrons, souffrent généralement d'un grave problème de recombinaison de charge [151]. Une stratégie efficace pour résoudre ce problème consiste à soutenir le semi-conducteur hôte avec des matériaux hautement conducteurs qui peuvent fournir une voie directe pour un transfert d'électrons photoexcité plus rapide vers une interface solide/liquide et atteindre une densité photocourant élevée. Les exemples incluent le TiO_2 combiné à des nanoribbons de graphène 1D [152], des nanotubes de carbone à parois multiples (MWCNTs) [153], Au-MWCNTs [154] et des cadres métal-organiques (MOF) [155]. En outre, le réglage de la morphologie (nanotubes, nano-tiges et nanofils [156]) a également facilité le transfert de charge sans les défis de limite de grain.

Stabilité des matériaux et dynamique de charge

Les QDs colloïdaux souffrent souvent de sensibilité de surface aux environnements externes tels que la lumière, les ligands de surface, l'oxygène, l'humidité et la température) en raison du rapport surface / volume élevé [28]. Il peut induire des pièges de charge / défauts qui se traduit par une forte densité de centres de recombinaison et par conséquent, une diminution de la stabilité photo / chimique ainsi que des performances réduites du dispositif PEC. Dans ce contexte, le recouvrement du noyau avec une coque inorganique appropriée a été développé pour atténuer la dégradation des QDs et régler la dynamique de charge. Kim et al. [102] a utilisé la méthode basée sur SILAR pour déposer une coque Mn-CdS sur des QDs PbS, ce qui a amélioré l'absorption de la lumière de 400 à 800 nm. Cependant, leur photocourant élevé (22,1 mA/cm^2) diminue rapidement (55% de la valeur initiale après 5 min), probablement en raison des états de piège de surface interfaciale qui se produisent avec le dépôt de SILAR [143]. Pour résoudre ce problème, des QDs colloïdaux de noyau / coquille sont pré-synthétisés qui passent les liaisons pendantes à la surface des QDs, améliorant ainsi la stabilité chimique, thermique et

photochimique. Un photoanode TiO_2 utilisant des CDSe/CdS QDs à coque épaisse a maintenu 57,5% de sa densité de photocourants après 2 h d'éclairage continu, ce qui est mieux que les points quantiques CdS nus (42,1%). L'épaisseur de la coque influence la dynamique de charge dans les QDs cœur/coque. Par exemple, l'augmentation de l'épaisseur de la coque pour les CdSe/CdS QDs réduit le taux de transfert de trou 4-5 fois par rapport aux CdSe QDs. La couche de coque en alliage à gradient interfacial s'est avérée présenter un taux de transfert électron-trou plus élevé qui modifie le potentiel de confinement pour atteindre une densité photocourante record de 17,5 mA/cm^2 [157]. Ces efforts ouvrent de nouvelles voies pour atteindre simultanément une stabilité optimale et un transfert de charge efficace.

Développement d'un dispositif PEC à base de QDs sans métaux lourds

La plupart des QDs haute performance contiennent des métaux lourds tels que Cd, Hg et Pb ou utilisant ces éléments lors de la synthèse de QDs, ce qui limite le développement commercial de photoélectrodes à base de QDs. En plus de la stabilité et de l'efficacité, le développement de photoélectrodes à base de QDs sans métaux lourds joue également un rôle crucial pour les applications commerciales.

Les photoélectrodes écologiques à base de points de carbone ont le potentiel d'une large gamme d'absorption de la lumière et d'autres avantages tels que l'abondance de la terre, la stabilité chimique, la rentabilité et une large absorbance optique [158]. Bien que la densité de courant soit très faible (<4 mA/cm^2) en raison d'une recombinaison de charge relativement sévère [159]. Un photoanode SnSe QDs-TiO_2 actif de NIR synthétisé par l'approche d'échange de cations assisté par modèle présente une densité de photocourant de 8,2 mA/cm^2 [160]. Cependant, Sn^{2+} s'oxyde facilement à l'état Sn^{4+} qui se forme comme une impureté pendant le processus de fabrication, affectant la production de H_2. De plus, les QDs à base de Sn impliquent l'utilisation de Cd pour la synthèse. Comme alternative, les semi-conducteurs ternaires I-III-VI_2 ont été largement étudiés en raison de la synthèse à faible coût, des propriétés optoélectroniques accordables de composition et de l'alignement approprié de la bande pour la réduction de l'eau. La plupart des rapports montrent une très faible densité de photocourants, probablement due à des pièges de charge induits par des défauts. Les QDs NIR non colloïdaux produits par épitaxie de faisceau moléculaire ont démontré des densités de courant élevées (18 mA/cm^2), mais cette méthode implique des techniques de dépôt complexes et coûteuses [161]. Tong et al. [162] les QDs colloïdaux synthétisés $CuInS_2$/ZnS noyau/coquille mince, résultant QDs-PEC dispositif montrent une densité photocurrente élevée de 5,3 mA/cm^2. Une coquille épaisse s'est avérée efficace pour supprimer la recombinaison Auger pour améliorer le

rendement quantique PL et améliorer la durée de vie exciton des QDs ternaires I-III-VI_2. Li et al. [163] synthétisé $CuInSe_xS_{1-x}$ alliage couche interfaciale graduée en $CuInSe_2/CuInS_2$ QDs et obtenir une amélioration de 70% de la densité de photocourant. À l'avenir, l'ingénierie des QDs sans métaux lourds devrait se concentrer davantage sur l'ingénierie de la surface et de l'interface des QDs I-III-VI_2.

CQD pour dispositifs optiques anti-contrefaçon

Les progrès de la science et de la technologie modernes ont rendu la vie quotidienne pratique pour les gens, mais apportent également la contrefaçon comme un travail sans effort pour les fraudeurs [164]. Les produits contrefaits à forte prévalence perturbent la croissance économique normale, causent d'énormes pertes économiques et ont un effet négatif sur la vie humaine. La contrefaçon de marque mondiale (GBC) fait état d'une perte économique mondiale de 3 billions de dollars américains causée par la contrefaçon en 2022 et une augmentation exponentielle est attendue [165]. Par conséquent, la conception et le développement de la technologie anti-contrefaçon de haute sécurité (ACF) est cruciale pour améliorer la protection des documents, prévenir la contrefaçon et la réplication. Bien que diverses techniques et matériaux anti-contrefaçon, y compris les hologrammes laser, l'identification par radiofréquence, la technologie du filigrane, la technologie des pistes nucléaires, etc., aient été développées, l'impression luminescente a été largement utilisée en raison de sa facilité d'utilisation, de sa production désignable et à haut débit. Les matériaux anti-contrefaçon luminescents utilisant des points quantiques semi-conducteurs, des cristaux photoniques et des nanomatériaux à conversion à la hausse ont attiré beaucoup d'attention parmi les chercheurs pour ouvrir la voie à des modèles anti-contrefaçon plus avancés**.**

Principes de travail

L'antidénombre à base de luminescence consiste à incorporer des matériaux luminescents qui émettent de la lumière lorsqu'ils sont exposés à des stimuli externes [166]. Les matériaux luminescents sont conçus pour répondre de manière unique dans diverses conditions qui rendent les contrefacteurs difficiles à reproduire les articles authentiques [167]. Les QDs semi-conducteurs [168], les colorants organiques [168], les points de carbone Yb/Er [169], la pérovskite [170] et les nanoparticules dopées Ln^{3+} [167] sont les excellents matériaux luminescents qui peuvent être excités par des stimuli externes tels que la lumière, la chaleur, la force mécanique et les réactifs chimiques. Par exemple, le $CsPbBr_3$ produit une fluorescence verte sous la lumière UV tandis que les NPs dopés Ln^{3+} peuvent être réglés sur différentes couleurs en modifiant la longueur d'onde d'excitation [171, 172]. Généralement, sur la base du

nombre de stimuli externes, l'anticounterfeiting de luminescence est classé en trois niveaux : (i) niveau simple, (ii) double niveau, et (iii) anticounterfeiting à plusieurs niveaux. L'anti-contrefaçon à niveau unique est le mode anticounterfeiting à luminescence le plus simple qui est largement appliqué dans diverses devises et certificats. Selon divers modes de luminescence, l'anti-contrefaçon à un seul niveau est divisée en PL à chimiluminescence, PL de conversion vers le haut (UC) et anti-contrefaçon PL de conversion vers le bas (DC) [173]. L'anticounterfeiting DC PL est réalisé par absorption de photons de haute énergie et libère des photons de faible énergie [174]. Actuellement, les différents matériaux utilisés dans l'anti-contrefaçon DC PL à un seul niveau, y compris les points de carbone, les luminogènes organiques, les nanofibrilles de cellulose / CdTe QDs, les points de carbone dopés à l'azote, le cyanurate de mélamine greffé Tb^{3+}/Eu^{3+} et $SrAl_2O_4 : Eu^{2+}$. Les matériaux composites à base de QDs pourraient offrir des caractéristiques prometteuses pour des modèles anticounterfeiting plus précis, complexes et de haute dimension, qui ont été d'un grand intérêt par rapport aux matériaux anticounterfeiting monochromes simples de bas niveau.

Défis à relever

À l'époque d'aujourd'hui, les principales limites des matériaux anticounterfeiting luminescents sont leur susceptibilité aux dommages lorsqu'ils sont exposés à des facteurs environnementaux tels que le pH, l'humidité et la température. La dégradation des matériaux luminescents dans diverses conditions environnementales limite leur application pratique dans divers environnements. La sensibilité à ces facteurs entraîne la perte d'informations sensibles cryptées. Les chercheurs s'efforcent continuellement de surmonter ces limites en fabriquant des matériaux stables pour offrir une meilleure protection contre les facteurs environnementales. Xu et al. [170] a démontré une stabilité de stockage élevée (60 jours) et une stabilité thermique (150 °C) pour les étiquettes de sécurité anti-contrefaçon à base de nanocristaux $CsPbBr_6/SiO_2$ protégées par Cs_4PbBr_6/SiO_2. Ding et al. [175] a conçu des nanostructures noyau-coque De $NaGdF_4$:Yb/Ho/Ce@$NaYF_4$:X (X = Eu, Tb, Sm, Dy) en tant qu'émetteurs bimodes efficaces et multicolores accordables pour l'anti-contrefaçon. Néanmoins, les matériaux upconversion à base d'éléments lanthanides (Ce, La, Gd, Eu, Tb) sont coûteux et leur synthèse compliquée limite leurs applications pratiques. Les QDs à base de chalcogène métallique présentent des performances d'émission prometteuses et offrent une accordabilité composition / taille, qui fournit une longueur d'onde d'émission plus large pour couvrir la région de lumière visible. Chen et leurs collègues [176] ont signalé l'hybride CdTe/ZnS-2-polyamidoamine utilisant des méthodes d'impression microfluidique, et la réponse du motif imprimé dans les couleurs vertes

et rouges sous la lumière UV. Liu et al. [177] a mis au point des QDs colloïdaux II-VI à base de Rouge-vert-bleu (RVB) émettant des encres de sécurité à fluorescence. Les étiquettes de sécurité fabriquées sont invisibles à l'œil nu, mais peuvent être visualisées sous la lumière UV, et en outre, la stratégie d'authentification basée sur l'IA la rend très prometteuse pour les industries sensibles telles que celle nucléaire. Cependant, pour la commercialisation, ces étiquettes de sécurité contiennent des éléments toxiques comme le Cd et le Pb. Par conséquent, le développement de QDs alternatifs sans métaux lourds pour les applications anti-comptage est important pour assurer la sécurité et la durabilité environnementale.

Objectifs de la recherche

Sur la base de mon examen de la littérature, les défis importants ont été identifiés pour concevoir et développer des QDs colloïdaux /coquilles colloïdaux sans métaux lourds efficaces, y compris la réduction de la recombinaison de charge de surface, la modulation des caractéristiques d'émission PL et la dynamique des porteurs de charge comme souhaité pour les deux applications clés, à c'est-à-dire la production PEC H_2 et les dispositifs optiques anti-contrefaçon. L'ingénierie de surface des QDs en trouvant un matériau de coque approprié qui assure à la fois la stabilité et une meilleure génération / séparation de charge est nécessaire pour la production de PEC H_2 basée sur QDs haute performance. Dans les dispositifs optiques anti-contrefaçon, la modulation des caractéristiques PL en utilisant des dopants doubles avec la passivation de la coque pourrait améliorer les caractéristiques de sécurité et fournir une ultra-stabilité contre la dégradation de l'environnement, qui sont essentielles pour une application pratique. Par conséquent, les objectifs de ma thèse sont les suivants :

1. Production photoélectrochimique de H_2

Le premier projet est axé sur la conception et la synthèse de QDs $ZnInSe_2$ dopés $ZnInSe_2$ dopés $ZnInSe_2$ à coque allié $ZnInSe_2$ respectueux de l'environnement pour la production de PEC H_2 à énergie solaire. L'objectif est de prévenir les pièges/défauts de surface et de régler la dynamique du support de charge des QDs de noyau de $CZISe_2$ par une approche de passivation in situ de la coque. Cette approche peut atténuer efficacement la recombinaison de charge indésirable et fournir un alignement de bande approprié pour le transfert de charge. Les photosensibilisants $CZISe_2$/ZSeS QDs synthétisés sur des couches minces semi-conductrices TiO_2 mésoporous à large bande interdite ont été utilisés comme photoanode pour la production

de PEC H_2. En outre, les MWCNTs sont incorporés pour améliorer les propriétés de transport de charge pour une production améliorée et stable de PEC H_2.

2. Application optique anti-contrefaçon

Le deuxième projet consiste à moduler en synergie les propriétés optiques des QDs de noyau / coque $ZnInSe_2$/ZnSe respectueux de l'environnement en incorporant le dopage cu et l'alliage mn dans leur noyau et leur coque pour étudier leur utilisation dans la lutte contre la contrefaçon et le cryptage de l'information. Les QDs ont été introduits sur le polymère PMMA pour former des encres cachées intelligentes pour les modèles d'écriture et d'impression. Nous avons étudié la durabilité des motifs imprimés en les exposant à des températures variables et à des tests de trempage de l'eau. Un mécanisme a été proposé pour comprendre comment les interactions dopant modulent les caractéristiques d'émission des encres de sécurité anti-contrefaçon.

Méthodologie

La fabrication de Photoanode à base de QDs pour la production de PEC H_2 sont les suivantes :

a. $CZISe_2$ QDs et $CZISe_2$/ZSeS noyau/coquille QDs ont été synthétisés utilisant la technique d'injection à chaud.
b. Les couches minces de TiO_2 ont été utilisées comme semi-conducteur hôte pour fabriquer le photoanode et préparées en utilisant l'approche de la lame du médecin. La couche de transport d'électrons (MWCNTs) a été intégrée au TiO_2 en utilisant la même méthode.
c. Les QDs synthétisés ont été déposés sur des couches minces par la technique de dépôt électrophorétique.
d. Un semi-conducteur inorganique ZnS et du SiO_2 ont été déposés en tant que couches de coque finales pour protéger le photoanode à base de QDs de la dégradation.

La fabrication de dispositifs optiques anti-contrefaçon basés sur QDs sont les suivantes :

a. $ZISe_2$, Cu:$ZISe_2$, Cu:$ZISe_2$/ZSe, Cu:$ZISe_2$/Mn:ZSe, et $ZISe_2$/Mn:ZSe ont été synthétisés par la technique d'injection à chaud.
b. Les QD purifiés ont été intégrés au polyméthacrylate de diméthyle pour former une solution QDs/PMMA.
c. Des étiquettes de sécurité invisibles ont été créées en dessinant des motifs à l'aide d'encre luminescente sur différents types de matériaux d'emballage.

Caractérisation

1. La propriété d'absorption et d'émission de lumière des QDs a été étudiée à l'aide de la spectroscopie d'absorption UV-visible et de la spectroscopie de photoluminescence.
2. La morphologie et les caractéristiques structurelles des QDs ont été examinées par XRD et TEM.
3. Les états chimiques des QD du noyau et du noyau/coque ont été étudiés par XPS.
4. La morphologie de surface, la composition du photoanode à base de QDs fabriqués ont été étudiées par SEM, EDS.
5. L'efficacité de l'injection de charge et les taux de transfert de charge dans le photoanode basé sur QDs ont été mesurés par analyse TRPL.
6. La dynamique de porteur de charge à différentes interfaces (QDs/électrolyte, QDs/TiO_2/électrolyte) ont été étudiées par EIS.

Dans le chapitre trois, une coquille ZnSeS surfondie Cu:$ZnInSe_2$ QDs ($CZISe_2$/ZSeS core/shell QDs) a été conçue et synthétisée par une approche de passivation de croissance in situ. Les $CZISe_2$/ZSeS core/shell QDs ont été sensibilisés sur le photoanode TiO_2 dans le dispositif PEC pour la production de H_2. L'objectif de ce projet est d'atténuer les pièges de surface et les défauts des QDs $CZISe_2$ en utilisant une coque ZnSeS, réduisant ainsi la recombinaison des porteurs non radiatifs pendant le fonctionnement de l'appareil. L'effet de l'ingénierie de la coque a été étudié sur la dynamique du support de charge et la performance du PEC. L'appareil PEC basé sur des QDs $CZISe_2$/ZSeS présente une densité de photocourants sans précédent de 11,80 mA/cm^2, soit 7% de plus que les QD $CZISe_2$ nus. De plus, la stabilité opérationnelle à long terme a été améliorée de 10% par rapport aux QD $CZISe_2$ de référence de plus de 3600 s. La dynamique des porteurs et la structure de la bande électronique ont été étudiées pour comprendre l'amélioration de la densité des photocourants. La coque ZnSeS agit comme une couche de passivation efficace qui réduit la recombinaison du support, ce qui entraîne un taux d'injection de charge plus élevé aux interfaces QDs/TiO_2 et QDs/électrolyte. D'ailleurs, une densité de photocourant d'enregistrement de 13,15 mA/cm^2 à 0,8 V contre RHE a été réalisée en incorporant des MWCNTs dans le photoanode QDs/TiO_2. Le résultat de ce projet est présenté à la Figure 6. De plus, les 80% de rétention photocurrente initiale démontrent l'excellente stabilité à long terme de ce dispositif PEC.

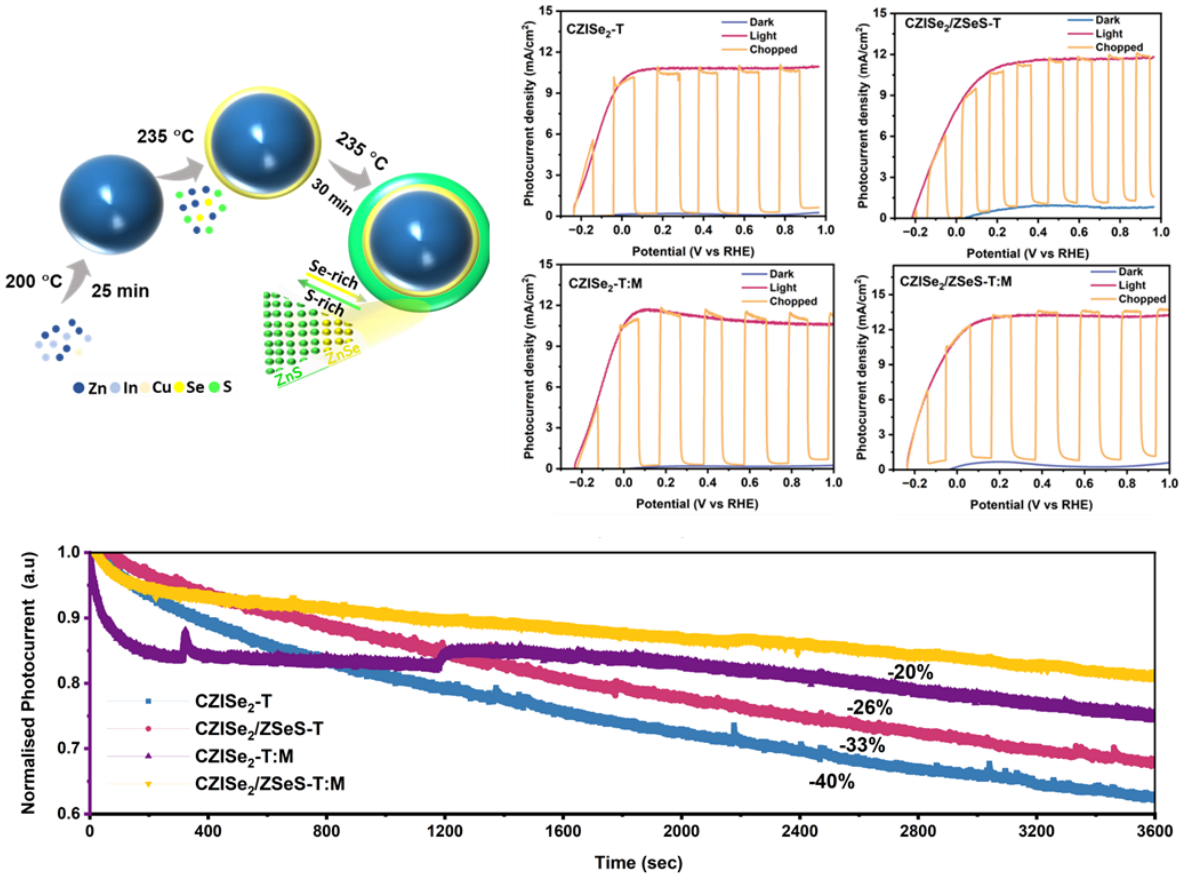

Figure 6 Illustration schématique de la synthèse de $CZISe_2$ et $CZISe_2$/ZSeS QDs, Densité photocourant–dépendance potentielle de FTO|TiO_2|$CZISe_2$ QDs|ZnS, FTO|TiO_2|CZISe/ZSeS QDs|ZnS, FTO|MWCNTs|TiO_2|$CZISe_2$, et FTO|MWCNTs|TiO_2|$CZISe_2$/ZSeS dans l'obscurité, sous éclairage solaire haché et continu 1 (AM 1,5 G, 100 mW/cm^2), et J–t tracés de photoanodes représentatifs sous un éclairage à un soleil à -0,6 V par rapport à Ag/AgCl.

Dans le chapitre quatre, une approche synergique a été adoptée pour moduler les propriétés optiques de $ZnInSe_2$/ZnSe noyau / coque QDs par le dopage Cu à l'intérieur du noyau et Mn alliage dans la coque. Les QDs Cu:$ZnInSe_2$/Mn:ZnSe conçus ont été intégrés au polymère PMMA pour être utilisés comme encres de sécurité luminescentes pour les applications anti-contrefaçon. Sur la base d'études liées au PL, les résultats indiquent que le dopage au Cu dans le $ZnInSe_2$ capture efficacement les trous, tandis que l'alliage mn dans la coque ZnSe fournit des états d'espace moyen pour la relaxation des électrons. Cette stratégie de double dopage a considérablement prolongé la durée de vie du PL (201 ns) et a amélioré l'intensité d'émission de PL par rapport aux QDs non défaits et proprement dopés. Malgré la présence de deux dopants optiquement actifs (Cu et Mn), l'émission de dopant cu est prédominante dans le

Cu:ZnInSe$_2$/Mn:ZnSe en raison de la bande interdite étroite du matériau hôte comme confirmé par les spectres PL. Les QDs de noyau/shell modulés de Cu et de Mn dopants pourraient produire une énorme capacité de codage et réaliser le cryptage complexe de l'information. Les caractéristiques anti-contrefaçon des motifs imprimés sont restées intactes même après un trempage direct de l'eau pendant une période prolongée de 10 semaines. De plus, ils présentaient une stabilité thermique supérieure, conservant 70% de l'intensité pl à 170 °C. Le résultat de ce projet est illustré à la Figure 7. Ces résultats indiquent que la manipulation synergique des dopants de Cu et de Mn dans des QDs de noyau/coquille respectueux de l'environnement montre un potentiel prometteur pour réaliser des encres luminescentes très stables pour des applications anti-contrefaçon.

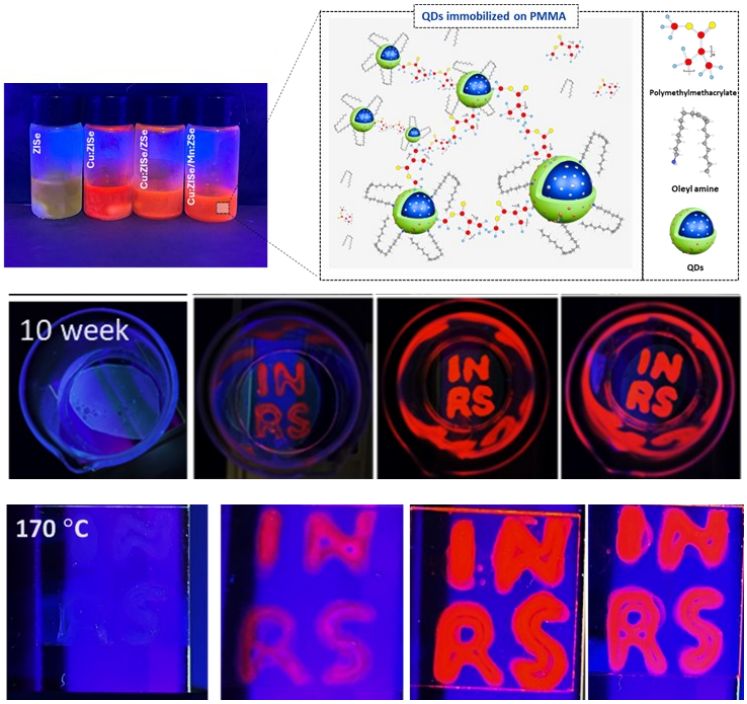

Figure 7 Photographie de flacons contenant des encres luminescentes préparées sous exposition à la lumière UV. Test de stabilité - Photographies des feuilles de plastique imprimées INRS placées à l'intérieur de l'eau après dix semaines. Photographies numériques de lettres INRS imprimées sur verre à l'aide d'encres luminescentes maintenues à 170 °C sous lumière UV.